Conditional gene targeting of *Hif1a* reveals an unexpected protective role of myeloid cells in liver cancer cachexia

Von der Fakultät für Mathematik, Informatik und Naturwissenschaften der RWTH
Aachen University zur Erlangung des akademischen Grades einer Doktorin der
Naturwissenschaften genehmigte Dissertation

vorgelegt von

Merve Erdem, M.Sc.
aus
Safranbolu, Türkei

Berichter: Univ.-Prof. Dr. Thorsten Cramer
Univ.-Prof. Dr. Joost van Dongen
Univ.-Prof. Dr. Till Marquardt

Tag der mündlichen Prüfung: 22.07.2019

Diese Dissertation ist auf den Internetseiten der Universitätsbibliothek verfügbar.

Acknowledgements

First of all, I would like to express my greatest gratitude to my supervisor, mentor Univ.-Prof. Dr. med. Thorsten Cramer for giving me the opportunity to perform this study in his lab first in Berlin and later in Aachen. I am thankful for his guidance, constant advice and patience during my PhD time, and also for very valuable discussions and for his boundless optimism, he has always been there and supportive whenever I needed.

I am incredibly grateful to my examiners Univ.-Prof. Dr. rer. nat. Joost van Dongen and Univ.-Prof. Dr. Till Marquardt for their time and interest to read and evaluate my thesis. I would like to thank the external member of my doctoral committee Univ.-Prof. Dr. Ralph Panstruga and the head of my doctoral committee Univ.-Prof. Alan Slusarenko, Ph. D. DIC for their time and interest.

I also thank to Univ.-Prof. Dr. med. Ulf Peter Neumann, the director of the Department of General, Visceral, and Transplantation Surgery, giving me opportunity to work for my thesis in this department.

I would like to thank former and current members of Cramer lab for helpful discussions and input during my study and for friendly support. My great thanks go for our ‘Office team’, this work would have not been possible without contribution of Dr. Jessica Wappler, Laura Robrahn, and Dr. Sandra Jumpertz. They make such a nice working atmosphere as being not just great colleagues but also friends with their continuous support and advice.

I would also like to express my great appreciations to Dr. Athanassios Fragoulis who always helps and supports my work.

Many thanks go to our collaborators Gregory van der Kraft, David van Dijk, and Georg Lurje for their contribution and help with patient study, Univ.-Prof. Dr. Dr. Twan Lammers and his group for imaging techniques and Dr. Marco Koch for his contribution with brain analysis. I also thank Johanna Wulfmeier for tumor quantification analysis.

I am also grateful for the support from my graduate school Berlin School of Integrative Oncology which made my way to Germany at first place.

I have to also acknowledge my great friend and colleague Dr. Olya Vvedenskaya and my friends Basak Sentürk, Eray Sahin, Gökhan Tunc Karaer, Dr. Milas Ugur, Pinar Atalay Dündar, and Tugba Karaca for their support.

Last but not least, I would like to thank my parents, my brother and sister for always believing in me and supporting me in so many ways throughout writing this thesis and my life in general.

Table of contents

Acknowledgements I

Table of contents III

Abbreviations VIII

Summary 1

Zusammenfassung 2

1 Introduction 4

- 1.1 Liver cancer 4
  - 1.1.1 Liver and hepatocytes 4
  - 1.1.2 Hepatocellular carcinoma (HCC) 4
    - 1.1.2.1 Epidemiology and risk factors 5
    - 1.1.2.2 Molecular pathogenesis of HCC 6
    - 1.1.2.3 Diagnosis, treatment and prognosis of HCC 7
- 1.2 Cachexia as a wasting disease 8
  - 1.2.1 Definition of cachexia 8
  - 1.2.2 Cancer cachexia 9
  - 1.2.3 Pathophysiology of CAC 10
    - 1.2.3.1 Metabolic alterations 10
    - 1.2.3.2 Tumor-induced factors 11
    - 1.2.3.3 Host-tumor interactions 12
    - 1.2.3.4 Host response 13
    - 1.2.3.5 Muscle wasting mechanisms 13
    - 1.2.3.6 Adipose tissue wasting 14
    - 1.2.3.7 Brain 16
    - 1.2.3.8 Liver 17
    - 1.2.3.9 Heart 17
  - 1.2.4 Treatment approaches in cancer cachexia 18
- 1.3 Adipose tissue and macrophages 19
- 1.4 Hypoxia-inducible factor 1 (HIF-1) 20

1.5 Aim of the study ... 22

2 Materials ... 24

2.1 Animals ... 24
2.2 Cells ... 24
2.3 Antibodies ... 25
2.3.1 Primary antibodies ... 25
2.3.2 Secondary antibodies ... 25
2.4 Buffers and solutions ... 26
2.5 Chemicals and reagents ... 28
2.6 Consumables ... 34
2.7 Kits ... 35
2.8 Primers ... 36
2.8.1 Genotyping primers ... 36
2.8.2 Quantitative polymerase chain reaction primers ... 36
2.8.3 Design of primers ... 37
2.9 Substrates and inhibitors ... 38
2.10 Instruments ... 39
2.11 Computer programs ... 40

3 Methods ... 42

3.1 Animals ... 42
3.1.1 ASV-B mice as a HCC animal model ... 42
3.1.2 Hepatocyte- and myeloid cell-specific *Hif1a* knockout in ASV-B mice ... 43
3.1.3 Tissue collection ... 45
3.2 Monitoring and imaging of animals ... 46
3.2.1 Body weight, food intake and body composition measurements ... 46
3.2.3 Computed tomography imaging of mice ... 46
3.3 Hematological and biochemical methods ... 47
3.3.1 Blood count ... 47
3.3.2 UPS and apoptotic activities ... 47
3.3.2.1 GC tissue extraction ... 47

3.3.2.2 Bradford assay for quantification of protein concentration 48
3.3.2.3 UPS activity assay 48
3.3.2.4 Apoptotic activity assay 48
3.3.3 Luminex® assay for cytokine measurement from blood serum 49
3.3.4 *Ex vivo* lipolysis assay 51
3.3.5 Catecholamine measurement 51
3.3.6 Protein analysis 52
3.3.6.1 Protein extraction from tissue 52
3.3.6.2 Lowry assay for quantification of protein concentration 52
3.3.6.3 SDS-polyacrylamide gel electrophoresis 52
3.3.6.4 Western blot 53
3.4 Molecular analysis 54
3.4.1 Genotyping of animals 54
3.4.1.1 DNA isolation and polymerase chain reaction 54
3.4.1.2 Agarose gel electrophoresis 55
3.4.2 Gene expression analysis 56
3.4.2.1 RNA isolation 56
3.4.2.2 complementary DNA (cDNA) synthesis 57
3.4.2.3 Quantitative real-time polymerase chain reaction (qPCR) 57
3.5 Histological analysis 58
3.5.1 Liver tumor area analysis 58
3.5.2 Adipocyte cell size analysis 60
3.5.2.1 Hematoxylin and eosin (H&E) staining of eWAT 60
3.5.2.2 Calculation of cell size of adipocytes 60
3.5.3 Multiplex immunofluorescence staining 61
3.5.4 Neuron-macrophage distance calculation 63
3.6 Cell Culture 64
3.6.1 L929-conditioned medium production 64
3.6.2 Isolation and stimulation of BMDM cells 64
3.7 Body composition analysis of HCC patients 65
3.8 Statistical Analysis 66

4. Results 68

4.1 ASV-B mice show cachexia during cancer development 68
4.1.1 Body weight and food intake was not affected in ASV-B mice 68
4.1.2 Muscle and fat loss occurs in ASV-B mice 70
4.1.3 Complete blood count suggests anemia in ASV-B mice 72
4.2 Conditional knockouts of *Hif1a* in ASV-B mice reveals diverse outcomes regarding cachexia 73
4.2.1 ASV-B mice with hepatocyte-specific *Hif1a* knockout 73
4.2.2 ASV-B mice with myeloid-specific *Hif1a* knockout 77
4.3 Effect of the myeloid cell-specific *Hif1a* knockout on cachexia in ASV-B mice 80
4.3.1 ASV-B Hif1a^{MC} mice show less total fat amount 81
4.3.2 ASV-B WT mice have elevated levels of inflammatory cytokines 84
4.4 Increased lipolysis and browning occurs in ASV-B mice 85
4.5 Adipose tissue macrophages (ATMs) in ASV-B mice 90
4.5.1 Myeloid *Hif1a* loss decreases macrophage number in ASV-B mice eWAT 90
4.5.2 Macrophage phenotype in adipose tissue was not affected by *Hif1a* 92
4.5.3 Innervation and macrophage-neuron proximity in eWAT 93
4.5.4 Hypothalamic pro-opiomelanocortin (POMC) neuron activation in ASV-B mice 97
4.6 Quantification of body composition in human HCC patients 98

5. Discussion 101

5.1 ASV-B mice develop cachexia 101
5.2 Myeloid cell-specific *Hif1a* deficiency aggravates loss of adipose tissue in ASV-B mice 102
5.3 Lipolysis and browning of adipose tissue in HCC-induced cachexia 104
5.4 Macrophage accumulation in adipose tissue is affected by *Hif1a* 106
5.5 Hypothalamic activation and WAT innervation does not underlie the enhanced fat loss in ASV-B Hif1a^{MC} 108

5.6 A subgroup of patients shows low muscle and/or fat amount in HCC cohort 109
6. Conclusion 111
7. References 113
Declaration 126
Erklärung 126
Publications 127

Abbreviations

°C	degree celsius
AAMs	Alternatively activated macrophages
ACTRIIA/B	Activin A receptor type IIA or B
AgRP	agouti-related peptide
ANGPT2	Angiopoietin 2
ANOVA	Analysis of variance
APPR	Acute-phase protein response
APS	ammonium persulfate
ARC	Arcuate nucleus
Arg1	Arginase 1
ATGL	Adipose triglyceride lipase
ATM	Adipose tissue macrophages
ATP	Adenosine triphosphate
B2m	Beta-2 microglobulin
BCLC	Barcelona clinic liver cancer
BMDM	Bone marrow derived macrophage
BMI	Body mass index
bp	Base pairs
BSA	Bovine serum albumin
CAC	Cancer-associated cachexia
cAMP	Cyclic adenosine monophosphate
CAMs	Classically activated macrophages
CCR2	C-C chemokine receptor type 2
Cd274	Cluster of differentiation 274 gene
cDNA	Complementary DNA
cGMP	Cyclic GMP
Cidea	Cell death-inducing DNA fragmentation factor alpha-like effector A
Clec10a	C-type lectin domain family 10 member A gene
cm	Centimeter
cm^2	Square centimeter
CNS	Central nervous system
CRP	C-reactive protein
CTNNB1	Catenin beta 1
DEN	Di-ethyl-nitrosamine
DEPC	Diethyl dicarbonate
DMSO	Dimethyl sulfoxide
DTT	Dithiothreitol
DMSO	Dimethyl sulfoxide
DNA	Deoxyribonucleic acid
dNTP	Deoxynucleotide
dT	Deoxy-thymidine
EDL	Extensor digitorum longus
EDTA	Ethylene diamine tetraacetic acid

eWAT	Epididymal white adipose tissue
F4/80	EGF-like module-containing mucin-like hormone receptor-like 1
FBS	Fetal bovine serum
FGF	Fibroblast growth factor
FIH	Factor inhibiting HIF-1
g	gram
g	gravity
GI	Gastrointestinal
GC	Gastrocnemius
GC-A	Guanylyl receptor-A
H&E	Hematoxylin and eosin
HBV	Hepatitis B virus
HCC	Hepatocellular carcinoma
HCT	Hematocrit
HCV	Hepatitis C virus
HGB	Hemoglobin
HIF	Hypoxia inducible factors
Hif1a	Hypoxia inducible factor 1 alpha gene
HIF-1α	Hypoxia inducible factor 1-alpha
HPLC	High-performance liquid chromatography
HSL	Hormone sensitive lipase
HCl	Hydrogen chloride
IFN-γ / Ifn-γ	Interferon gamma
IGF-1	Insulin-like growth factor-1
IL-10 / Il-10	Interleukin 10
Il-17a	Interleukin 17a
IL-1β / Il-1β	Interleukin 1 beta
Il-4	Interleukin 4
IL-6 / Il-6	Interleukin 6
IR	Insulin receptor
IRS-1	Insulin receptor substrates
iNOS	Inducible nitric oxide synthase
JAK	Janus kinase
L3	The third lumbar vertebra
LANUV NRW	Landesamt für Natur, Umwelt und Verbraucherschutz Nordrhein-Westfalen
Lipe	Lipase E, hormone sensitive type gene
LMF	Lipid mobilizing factor
LPS	Lipopolysaccharide
M	molar
m^2	square meter
MAPK	mitogen-activated protein kinase
MCH	Mean corpuscular hemoglobin
MCP-1/CCL2	Monocyte chemoattractant protein-1
MCV	Mean corpuscular volume
mg	milligram

min	minute/s
ml	milliliter
mM	millimolar
mm	millimeter
Mrc1	Mannose receptor C-type 1
mRNA	Messenger ribonucleic acid
mTOR	Mammalian target of rapamycin
NF-kB	Nuclear factor-kB
nm	Nanometer
nmol	Nanomole
NMR	Nuclear magnetic resonance
Nos2	Nitric oxide synthase 2 gene
NPY	Neuropeptide Y
p300/CBP	CREB-binding protein
PCR	Polymerase chain reaction
PDE3	Phosphodiesterase 3
PDGFR	Platelet-derived growth factor receptor
PE	Phycoerythrin
Pgc1a	Peroxisome proliferator-activated receptor gamma coactivator 1-alpha
PGPH	Peptidylglutamyl-peptide hydrolysing
PHD	Prolyl hydroxylase domain enzymes
PBS	Phosphate buffered saline w/o Ca^{2+} and Mg^{2+}
PI3K	Phosphatidylinositol 3-kinase
PIF	Proteolysis-inducing factor
PKA	Protein kinase A
PKG	Protein kinase G
PLIN	Perilipin
POMC	Pro-opiomelanocortin
Pparg	Peroxisome proliferator activated receptor gamma
Prdm16	PR domain containing 16
PTHrP	Parathyroid hormone-related protein
qPCR	Quantitative real-time polymerase chain reaction
REE	Resting energy expenditure
RIP140	Receptor-interacting protein 140
RIPA	Radioimmunoprecipitation assay
RNA	Ribonucleic acid
RPMI	Roswell Park Memorial Institute medium
RT	Room temperature
s	Seconds
S.E.M.	Standard error of the mean
SAT	Subcutaneous adipose tissue
SDS	Sodium dodecyl sulfate
SDS-PAGE	Sodium dodecyl sulphate-polyacrylamide gel electrophoresis
STAT3	Signal transducer and activator of transcription 3
SV40	Simian virus 40

TA	Tibialis anterior
TAE	Tris acetate EDTA
TBS-T	Tris-buffered saline-Tween 20
TG	Triglycerides
TH	Tyrosine hydroxylase
TLR4	Toll-like receptor 4
TNF-α	Tumor necrosis factor alpha
Tnfa	Tumor necrosis factor alpha gene
TNFR	Tumor necrosis factor-a receptor
TP53	Tumor protein p53 gene
Ucp1	Uncoupling protein 1 gene
UPS	Ubiquitin proteasome system
UV	Ultraviolet
VAT	Visceral adipose tissue
VEGF	Vascular endothelial growth factor
VEGFR2	Vascular endothelial growth factor receptor 2
VHL	Von Hippel–Lindau
w	Weeks
WAT	White adipose tissue
WB	Western blot
WT	Wild-type
Xg	x gravity
α2-AR	α2-adrenoceptor
β1,2,3	β-adrenoceptors 1, 2 and 3
µCT	µicro computed tomography
µl	microliter
µM	micromolar

Summary

Cachexia is a wasting syndrome affecting 30-80% of cancer patients and represents a central obstacle in medical oncology as it is associated with poor therapy response and reduced overall survival. Cachexia is a hallmark in the context of solid tumors and especially prevalent in gastrointestinal cancers. While murine models for cancer cachexia in the context of pancreas and colon cancer are well established, no common mouse model exists for liver cancer (hepatocellular carcinoma (HCC))-associated cachexia. Here, the ASV-B mouse, a transgenic murine HCC model, is introduced as a means to study cancer cachexia. During HCC development, ASV-B mice showed robust cachexia as evidenced by the loss of fat and lean mass. In addition, these mice showed elevated inflammatory markers in blood, increased fat mobilization and browning of adipose tissue, all hallmarks of cancer cachexia.

Next, the molecular mechanisms underlying HCC cachexia were characterized. The transcription factor hypoxia inducible factor 1-alpha (HIF-1α) is centrally involved in the control of pro-tumorigenic as well as pro-inflammatory pathways. Given the well-established importance of inflammation in cachexia, the functional significance of HIF-1α was investigated in ASV-B mice lacking *Hif1a* gene expression specifically in tumor or myeloid cells by the Cre-loxP system. Cachexia development was not affected by deleting *Hif1a* in tumor cells. Rather unexpected, myeloid cell-specific *Hif1a* loss aggravated cachexia as evidenced by enhanced body fat loss, despite reduced expression of pro-inflammatory cytokines in the serum of HCC-bearing mice. Furthermore, myeloid cell-specific *Hif1a* deficiency was associated with decreased macrophage infiltration and macrophage proliferation in adipose tissue compared to wild-type mice, suggesting a role for local macrophages in the regulation of cancer-induced fat loss. Taken together, myeloid cell-mediated inflammation displays a rather unexpected beneficial function against cancer-induced tissue wasting in a murine HCC model, adding a further layer of complexity to the pathogenesis of cachexia.

Computed tomography-based analyses of HCC patients revealed that 34% of subjects displayed reduced visceral fat mass as part of the cancer cachexia phenotype, nicely complementing the murine phenotype identified in this study.

Zusammenfassung

Das Wasting-Syndrom Kachexie betrifft 30-80% der Krebspatienten und stellt ein zentrales Hindernis in der medizinischen Onkologie dar, da es mit einem schlechten Therapieansprechen und einer verminderten Gesamtüberlebensrate einhergeht. Kachexie kennzeichnet den Krankheitsverlauf von Patienten mit soliden Tumoren und ist besonders bei gastrointestinalem Krebs verbreitet. Während Mausmodelle für die Krebskachexie im Kontext von Pankreas- und Kolonkarzinom gut etabliert sind, existiert kein allgemeines Mausmodell für Leberkrebs (hepatozelluläres Karzinom (HCC))-assoziierte Kachexie. Hier wird die ASV-B-Maus, ein transgenes, murines HCC-Modell, vorgestellt, an dem die Krebskachexie untersucht wurde. Während der HCC-Entwicklung zeigten ASV-B-Mäuse eine robuste Kachexie, wie durch den Verlust von Fett und Magermasse nachgewiesen wurde. Darüber hinaus zeigten diese Mäuse erhöhte Entzündungsmarker im Blut, erhöhte Fettmobilisierung und Bräunung des Fettgewebes, typische Kennzeichen von Krebskachexie.

Als nächstes wurden die molekularen Mechanismen charakterisiert, die der HCC-Kachexie zugrunde liegen. Der Transkriptionsfaktor Hypoxie-induzierbarer Faktor 1-alpha (HIF-1α) ist zentral an der Kontrolle pro-tumorigener und pro-inflammatorischer Signalwege beteiligt. Angesichts der allgemein bekannten Bedeutung von Entzündungen im Kontext von Kachexie wurde der funktionelle Einfluss von Hif-1α bei ASV-B-Mäusen untersucht, denen mittels Cre-loxP-System die *Hif1a*-Genexpression spezifisch in Tumor- oder Myeloidzellen fehlte. Die Entwicklung der Kachexie wurde durch Deletion von Hif-1α in Tumorzellen nicht beeinflusst. Eher unerwartet erhöhte der Myeloidzell-spezifische *Hif1a*-Verlust die Kachexie, was sich in einem erhöhten Körperfettverlust widerspiegelte, obwohl die Expression pro-inflammatorischer Zytokine im Serum HCC-tragender Mäuse reduziert war. Darüber hinaus war im Vergleich zu Wildtypmäusen ein Myeloidzell-spezifisches *Hif1a*-Defizit mit einer verminderten Makrophageninfiltration und Makrophagenproliferation im Fettgewebe assoziiert, was einen Einfluss lokaler Makrophagen auf die Regulierung des durch Krebs hervorgerufenem Fettverlusts nahelegt. Zusammengefasst zeigt die Myeloidzell-vermittelte Entzündung einen eher unerwarteten, vorteilhaften Effekt auf den krebsinduzierten Gewebeabbau in einem murinen HCC-Modell, was eine weitere Komplexitätsschicht zur Pathogenese der Kachexie hinzufügt.

Computertomographie-basierte Analysen von HCC-Patienten zeigten eine reduzierte viszerale Fettmasse bei 34% der Probanden als Teil des Krebskachexie-Phänotyps, was den in dieser Studie identifizierten murinen Phänotyp gut ergänzte.

1 Introduction

1.1 Liver cancer

1.1.1 Liver and hepatocytes

The liver is an organ with endocrine and exocrine properties found in vertebrates. It is the largest gland in the human body and provides functions to maintain homeostasis. The liver can secrete many different hormones (e.g. insulin-like growth factor, angiotensinogen, and thrombopoietin) as a part of endocrine function and performs exocrine functions via the secretion of bile. The liver is essential for glucose homeostasis via glucose (gluconeogenesis, glycogenolysis) and glycogen production, as well as drug detoxification, regulation of cholesterol synthesis and transport, urea metabolism, and secretion of many plasma proteins (albumin and other carrier proteins, coagulation factors, fibronectin, C-reactive protein, and many others). Considering that the liver performs vital functions for the organism, liver-related diseases like hepatic fibrosis, cirrhosis, hepatitis, and liver cancer result in high morbidity and mortality [1, 2].

The liver comprises parenchymal cells and different types of non-parenchymal cells. The parenchymal part consists of hepatocytes which are highly specialized epithelial cells comprising approximately 80% of the whole liver cell population, whereas non-parenchymal cells include cholangiocytes (3%), endothelial cells, macrophages (2%), dendritic cells, lymphocytes, hepatic stellate cells (1.4%), and liver sinusoidal endothelial cells (2.5%). In the liver, hepatocytes represent the main functional cells and are located in the lobule divisions together with sinusoids, bile ducts, portal vein, and hepatic artery branches to orchestrate all liver functions [2].

1.1.2 Hepatocellular carcinoma (HCC)

Hepatocellular carcinoma (HCC) is a primary liver cancer with an aggressive behavior. The exact cellular origin of this cancer type has remained elusive until recently, and today studies reveal that HCC originates mainly from hepatocytes and additionally could also be derived from benign lesions of hepatic progenitor cells [3, 4].

1.1.2.1 Epidemiology and risk factors

Liver cancer is the fifth most prevalent cancer type in men (7.5% of all cancer cases) and ninth in women (3.4% of all cancer cases) according to the GLOBOCAN cancer statistics reports. Mortality to incidence rate is high as liver cancer is the second most common cause of cancer related death [5]. HCC comprises more than 90% of primary liver cancer cases. HCC incidence is different in various regions suggesting heterogeneity in the prevalence of underlying risk factors and ethnicity. Incidence of HCC is high in eastern Asia and Africa (80% of all HCC cases) where hepatitis B virus (HBV) infection and aflatoxin B1 in the diet are the main underlying factors [6]. On the other hand, other risk factors of HCC like hepatitis C virus (HCV) and alcohol consumption are common in North America, Europe, and Japan [7].

HCC is a cancer type with established risk factors (Fig.1.1). In most cases, chronic infections of HBV or HCV, alcohol-related liver disease, and nonalcoholic fatty liver disease are the dominant risk factors [8, 9]. As can be seen in Figure 1.1, viral infection or alcohol-induced hepatocarcinogenesis is associated with increased inflammation in the liver, cycles of hepatocyte necrosis and regeneration, as well as increased oxidative stress [10, 11]. Oxidative stress results in the formation of fibrosis and cirrhosis in the liver that can most likely progress to HCC. In the clinic, it has been observed that most of the HCC patients had a cirrhosis history. However, it should be noted that livers without cirrhosis can also develop this disease. Epidemiology data show that the prevalence of non-cirrhotic HCC development can vary (2-54%) among the different geographical areas and aetiological factors [12].

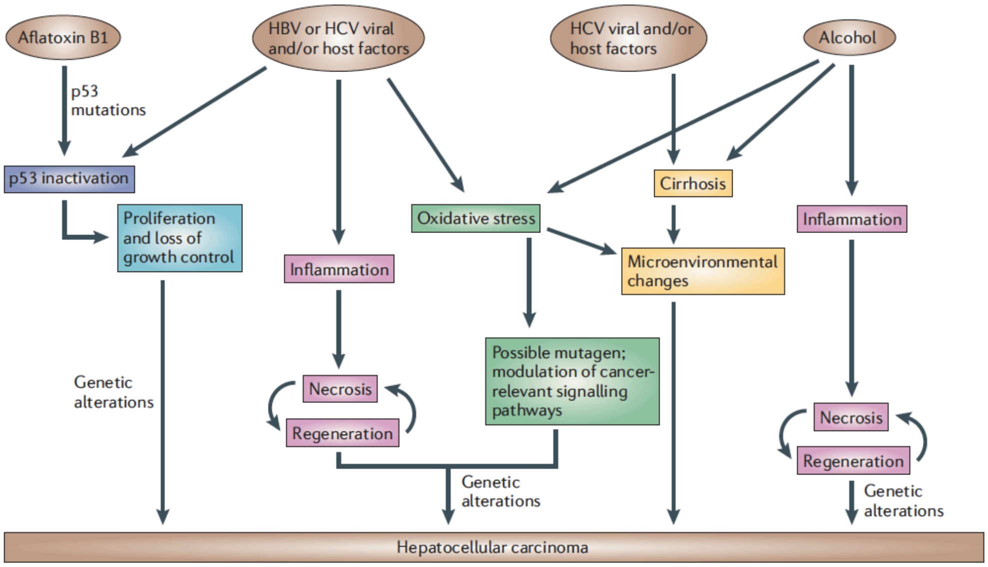

Figure 1.1: Mechanisms of HCC formation. Potential hepatocarcinogenesis mechanisms with the different risk factors are shown. Same colors imply the commonalities (figure is modified from Farazi *et al.* [13]).

1.1.2.2 Molecular pathogenesis of HCC

Similar to the development stages of other cancer types, HCC is also a multistep process (Fig. 1.2). In the molecular pathogenesis of the disease, various genetic events have been characterized. The most common mutations occur in the tumor suppressor p53 coding *TP53* gene (25-40%, depending on tumor stage) and the β-catenin coding *CTNNB1* gene (25%). Other genomic alterations like chromosomal gains in 1q, 6p, 8q, 11q, and 17q or deletions in 1p, 4q, 8p, 11q, 13q, 16q, and 17p cause critical changes in the regulation of oncogenes and tumor suppressors [14]. As a result of these alterations, overexpression of members of ErbB receptor family and Hepatocyte Growth Factor activate downstream pathways of mitosis. In relation to proliferation cascades, Ras signaling is activated in more than 50% of HCCs and the mammalian target of rapamycin (mTOR) pathway was determined to be affected in 40-50% as a result of the mutations in phosphoinositide-3-kinase [13, 15]. Wnt signaling was found to be activated in 30% of HCC following mutations in β-catenin, overexpression of Wnt receptors, or E-cadherin inactivation. In addition to the proliferation pathways, increased angiogenesis activity through *VEGF*, *ANGPT2* genes, and fibroblast growth factor (FGF) signaling were detected [13, 14].

Genomic instability is another common cause of genetic alterations in HCC. Telomere erosion can be induced following viral infection, and then, telomerase reactivation together with loss of p53 activation cause DNA damage-response disruption and chromosome instability [16].

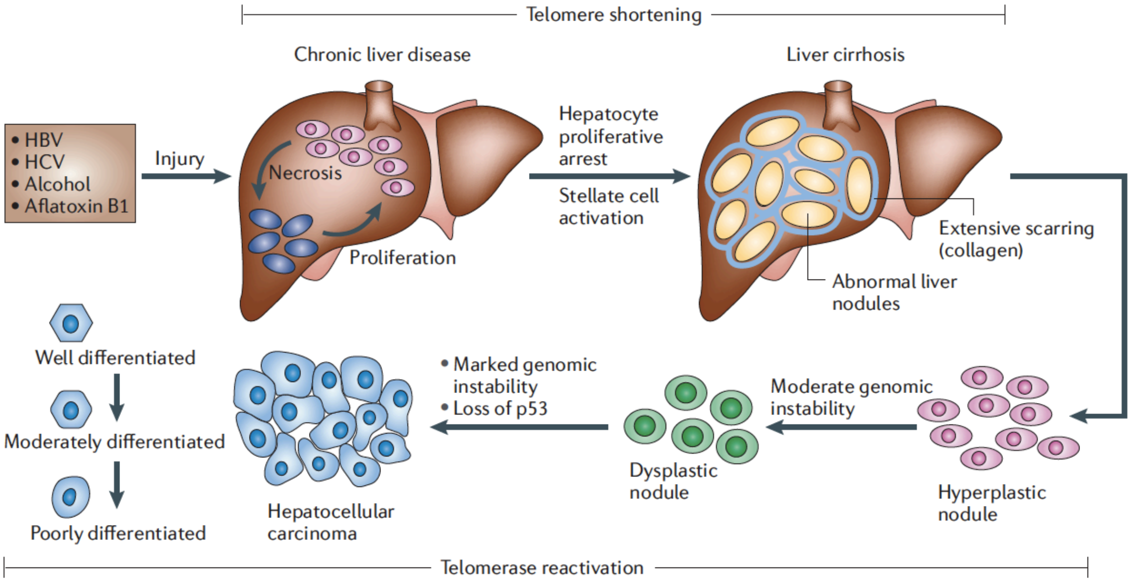

Figure 1.2: Progression of HCC through liver cirrhosis in human. Liver injury can be induced by several factors (HBV/HCV infection or alcohol/aflatoxin B1 consumption). Necrosis and then hepatocyte proliferation occur in the liver. Repeated cycle of necrosis-inflammation-regeneration causes chronic liver disease. Liver cirrhosis develops as nodule formation and increased collagen deposition. Nodules in the liver become hyperplastic and dysplastic with increased genomic stability. Next, HCC is observed and can be classified into well differentiated, moderately differentiated and poorly differentiated tumors (figure is taken from Farazi *et al.* [13]).

1.1.2.3 Diagnosis, treatment and prognosis of HCC

For most of the patients, diagnosis is achieved via ultrasonography. Smaller nodules (diameter <1 cm) are recommended for follow-up while non-invasive imaging techniques including contrast-enhanced computed tomography or magnetic resonance imaging is necessary for bigger nodules (diameter >1 cm) [17]. These non-invasive imaging-based diagnosis is only established for patients with cirrhosis. In case of a non-cirrhotic liver or a liver with atypical nodules, pathological analyses should be performed with biopsy samples collected from patients [18].

Treatment of HCC can be carried out with curative or palliative intent. HCC patients diagnosed with early-stage cancer according to Barcelona Clinic Liver Cancer (BCLC) strategy are treated by surgical resection, liver transplantation, or ablation. These treatments can be classified as curative due to their high rate of complete responses [17]. However, early detection is usually difficult in liver cancer, and patients are commonly diagnosed at late stages of the disease. In this case, curative approaches are no longer considered as a treatment option, since complete tumor resection is difficult and post-operative liver failure becomes a risk factor. Transarterial chemoembolization (delivery of chemotherapy agents to tumor via the hepatic artery) and sorafenib (a multikinase inhibitor having activity against c-Raf, B-Raf, VEGFR2, PDGFR, and c-Kit) treatment are palliative approaches with improved survival rates [19, 20]. Arterial embolization without chemotherapy, systemic chemotherapy, external radiotherapy, and radioembolisation failed to prove significant survival benefits for HCC patients [19, 21].

Prognosis of HCC is affected by tumor-related variables (size, number of nodules vascular invasion and extrahepatic spread) and liver function. Including these variables in the BCLC staging system, possible patient outcome and treatment decisions can be concluded despite the presence of high patient heterogeneity. Overall survival of HCC patients has improved in the last decades via curative treatment for early-stage diagnosed patients, as they show 5-year survival of 40-70%. However, late-stage patients still have a very poor prognosis (survival between 3-20 months) and can only be subjected to palliative therapies [17, 22, 23].

1.2 Cachexia as a wasting disease

1.2.1 Definition of cachexia

The term ‘cachexia’ comes from Greek words ‘kakós’ and ‘hexis’ literally meaning bad condition [24]. Historically, the first report about cachexia had been written by

Hippocrates, and he described the disease as ‘the flesh is consumed and becomes water, … the abdomen fills with water, the feet and legs swell, the shoulders, clavicles, chest and thighs melt away … This illness is fatal’ [25]. Current definition of cachexia was described by a formal international consensus of cachexia experts in 2011 and explained as ‘cachexia is a multifactorial syndrome characterized by an ongoing loss of skeletal muscle mass (with or without loss of fat mass) that cannot be fully reversed by conventional nutritional support and leads to progressive functional impairment’ [26]. Cachexia can emerge as a secondary disease under many different chronic diseases such as congestive heart failure, obstructive pulmonary disease, chronic kidney disease, diabetes, and cancer [27].

1.2.2 Cancer cachexia

Clinically, cachexia is diagnosed when patients with a chronic disease involuntarily lose more than 5% of body weight over the past 6 months or less. Besides, multiple other factors can be involved in cachexia including increased inflammation, loss of appetite (anorexia), fatigue due to decreased muscle strength, anemia, insulin resistance as well as an impaired protein anabolism-catabolism balance [28].

Regarding cancer, cachexia incidence among patients is noticeably high as, depending on tumor type, 30-80% of patients develop cachexia. Gastric and pancreatic cancer patients commonly show cachexia (80-90% of the patients), while the incidence is 50% for lung, prostate or colon cancer patients and approximately 40% in sarcoma and breast cancer [29, 30]. Cancer-associated cachexia (CAC) dramatically affects the quality of life of patients and decreases chemotherapy tolerance, resulting in poor prognosis. In addition, cachexia is associated with reduced survival in patients with weight loss >10% [31]. Overall, cachexia is estimated to be responsible for 20% of cancer-related deaths [32].

1.2.3 Pathophysiology of CAC

1.2.3.1 Metabolic alterations

Cachexia comprises a combination of multifactorial metabolic changes, and is characterized with an unusual energy and protein balance as a result of decreased food intake and disrupted metabolism [33]. Weight loss mainly originates from decrease in fat depots, in addition to the muscle loss. In muscle, increased protein catabolism has been observed during CAC. Intracellular proteolytic pathways such as ubiquitin-dependent proteolysis, lysosomal proteolysis, and the calcium/calpain pathway display increased activity [34-36]. In adipose tissue, lipolysis is the underlying mechanism of tissue loss [37]. In cachexia, a possible lipolysis-inducing actor is lipid mobilizing factor (LMF), which is secreted from tumors [38]. Another important factor in CAC is the elevated resting energy expenditure (REE) of affected patients. Cancer patients with solid tumors exhibited elevated REE as a result of disordered energy metabolism [39, 40]. Altogether, these metabolic changes are emerging due to the interactions between tumor and host response mechanisms (Fig.1.3) which are further explained below.

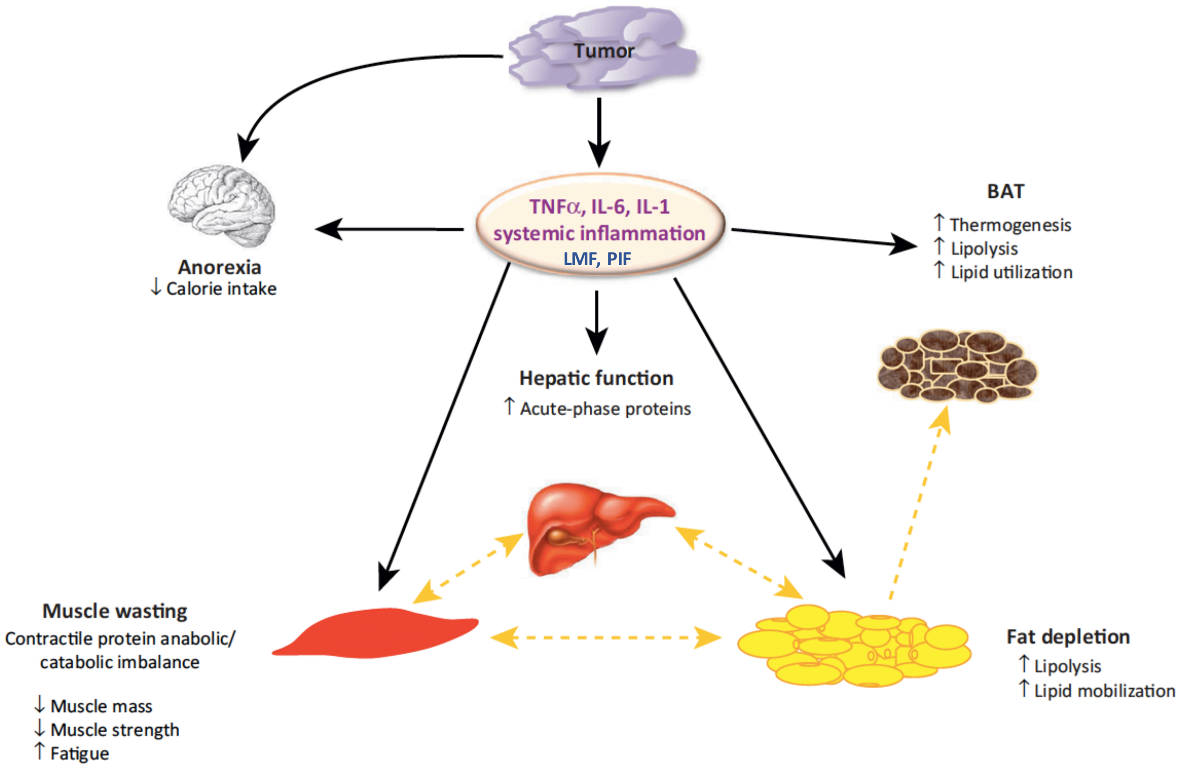

Figure 1.3: The interplay of tumor-derived factors (inflammatory cytokines and tumor cell-secreted proteins) with metabolic pathways in organs affected by cancer cachexia resulting catabolic energy imbalance. Inflammatory cytokines affect appetite control in the brain leading to anorexia. Muscle wasting results in fatigue and impaired physical activity, and adipose tissue depletes fat depots and energy reserves via increase lipolysis. Increased activity of brown adipose tissue (BAT) leads to thermogenesis via inefficient use of glucose and lipid. Acute-phase proteins are enhanced in liver as a response to inflammatory cytokines. There is also potential interplay between muscle, adipose tissue, liver, and BAT involving metabolites and signaling pathways (dashed lines) involving disruption of key metabolic pathways (figure is modified from Tsoli *et al.* [31]).

1.2.3.2 Tumor-induced factors

Anorexia and reduced calorie intake are important contributors for the development of cachexia, but these factors *per se* do not explain all catabolic alterations and weight loss of patients. In this regard, it has become clear that additional mediators and/or mechanisms induced by tumors or the host response can be involved in CAC. Tumor cells have been shown to secrete pro-cachectic factors named lipid mobilizing factor (LMF, also known as zinc-α2-glycoprotein) [41] and proteolysis-inducing factor (PIF) [42]. In adipose tissue, LMF can bind to adrenergic receptors and induce lipolysis via a cyclic adenosine monophosphate (cAMP)-dependent pathway [43]. PIF signaling through nuclear factor-κB (NF-κB) and signal transducer and activator of transcription 3 (STAT3) pathways has been shown in animal models where they induced proteolysis in muscle via the increased expression of the ubiquitin-proteasome pathway [42]. PIF has been detected in the urine of cancer patients, however mice expressing human homolog of PIF did not show cachexia and further studies failed to confirm the cachectic effect of human PIF [44]. Another tumor-derived factor is parathyroid hormone-related protein (PTHrP), which was associated with systemic inflammation and reduced survival in gastroesophageal carcinoma, and additionally, it was shown that this protein triggers cachexia in pancreatic cancer [45, 46].

1.2.3.3 Host-tumor interactions

Systemic inflammation is considered a hallmark of cancer. Inflammatory cytokines in cancer patients increase, since they can be secreted by tumor cells or by immune cells especially activated macrophages constituting a host response to the tumor [47]. In cachexia, it is not clear whether the host response or tumor itself is the main cause, nevertheless systemic inflammation is widely considered to be a driving force of cachexia process [48]. It is believed that CAC-associated metabolic alterations are triggered by immune responses and increased inflammatory cytokine production.

In animal studies, weight loss was positively correlated with the increased inflammatory cytokine levels in tumors [49, 50]. The identified pro-inflammatory cytokines in the context of cachexia include tumor necrosis factor-alpha (TNF-α), interleukin 1 beta (IL-1β), interleukin 6 (IL-6), and interferon gamma (IFN-γ) [49-51] . In some cancer patients, increased levels of TNF-α, IL-1β, and IL-6 in serum were correlated with the progression of tumors. Continuous application of these cytokines was able to induce cachexia in animal models [49, 52, 53]. Although it is not certain whether tumor or inflammatory cells are the main producers of these cytokines, production of pro-inflammatory cytokines is the reason of the acute phase protein response (APPR), a key marker of systemic inflammation, in cancer. The cytokine production is a natural response of the host against the tumor, but later on chronic inflammation during tumor progression causes wasting and cachexia [54].

1.2.3.4 Host response

Increased cytokine levels are able to trigger APPR in the liver of cancer patients. It has been shown in pancreatic cancer patients that especially IL-6-dependent mechanisms were responsible for APPR in hepatocytes [55]. Increased C-reactive protein (CRP) as one APPR marker is the most used criterion to detect systemic inflammation and it is included in clinical setting to estimate prognosis. For instance, tumor tissue concentrations of IL-1β and blood level of IL-6 were positively correlated with CRP serum concentrations in gastroesophageal and pancreatic cancer, respectively [56, 57] . Moreover, increased CRP levels are used as a prognostic marker for many different cancer types (pancreatic, lung, melanoma, gastrointestinal, ovarian, renal) [48].

1.2.3.5 Muscle wasting mechanisms

Muscle wasting is the first sign of cachexia as specified in the definition. In muscle tissue wasting, pro-inflammatory cytokines are thought to be the primary actors of the catabolic processes. In the healthy state, the anabolism/catabolism rate of muscle is balanced, preserving total muscle mass. In case of increased protein breakdown or decreased protein synthesis, a shift towards catabolism results in wasting and cachexia [58]. The adenosine triphosphate (ATP)-dependent ubiquitin proteasome system (UPS) was discovered as the main mechanism behind muscle wasting. The NF-κB transcription factor is activated by cytokines or PIF in muscle cells, and this activation increases the expression of E3 ubiquitin ligases (MAFBX and MURF1) which are responsible for myofibrillar protein degradation [59]. In addition to the proteasome pathway, caspase activity and apoptosis might also be induced through activation of the Janus kinase (JAK) and mitogen-activated protein kinase (MAPK) cascades following stimulation of muscle cells by cytokines and PIF [32, 60]. Another player in this context is myostatin (also known as growth differentiation factor 8). Myostatin binding to the Activin A receptor type IIA or B (ACTRIIA/B) receptor induces pathways including the SMAD complex as well as the JAK and MAPK pathway, increasing protein degradation and decreasing protein production [61]. Not only are catabolic pathways upregulated in muscle tissue wasting, but also anabolic pathways are downregulated. Under normal conditions, insulin-like growth factor-1 (IGF-1) stimulates protein synthesis and blocks UPS via activating phosphatidylinositol 3-kinase (PI3K)/AKT signaling. In cachexia, low levels of IGF-1 were detected as a contributor to muscle loss [62].

1.2.3.6 Adipose tissue wasting

In the international consensus definition of cachexia in the clinical setting, skeletal muscle loss is defined as a necessity, however, fat loss is not mandatory. Nevertheless, significant depletion of adipose tissue, possibly due to a negative energy balance, is often observed in cancer [63, 64]. Furthermore, animal and patient studies showed that adipose tissue loss might even start before the onset of muscle loss. In a patient study with different cancer types, accelerated fat loss occurred seven months before death, suggesting adipose tissue as an indicator of survival [65]. Adipose tissue loss results in altered tissue morphology. Cell size decreased and fibrosis occurred in a mouse model of cachexia [66], and adipocyte atrophy was detected in gastrointestinal cancer patients [67]. In another study with gastrointestinal cancer, patients displayed decreased cell volume while cell number remained unchanged [68]. Overall, these studies suggested that adipose tissue loss with reduced lipid storage appears as a hallmark of CAC.

Adipose tissue storage can be affected by many processes including lipolysis (lipid breakdown), lipogenesis (lipid storage), adipogenesis, and adipocyte death. Among these mechanisms, increased lipolysis is appreciated as the main underlying process of the adipose tissue loss in CAC [69-71]. Cancer patients with cachexia show high lipolytic rates, resulting in enhanced blood levels of glycerol and free fatty acids levels relative to total fat tissue amount [72]. Adipose tissue stores energy in the form of triglycerides (TG), and when energy is needed, TG is degraded to glycerol and free fatty acids via lipolysis followed by secretion of these into the blood stream. This degradation process is driven by enzymes such as hormone sensitive lipase (HSL) and adipose triglyceride lipase (ATGL). Increased HSL expression and activity were detected in cancer cachexia patients and patient-derived adipose cells [72, 73]. Moreover, ATGL or HSL knock-out mice exhibited resistance CAC-induced fat and muscle loss, and higher activity of ATGL and HSL enzymes in fat tissue was found in cancer patients compared to non-cachectic controls [74].

Lipolysis in CAC is induced by different serum factors including inflammatory cytokines, tumor derived factors (LMF, PTHrP) and catecholamines (adrenaline, noradrenaline, dopamine). LMF induces lipolysis in adipose cells through β3-adrenoreceptors which stimulates cAMP-mediated signal transduction and activates HSL [43]. In addition, catecholamines and natriuretic peptides can induce lipolysis in patients with cachexia [72]. Catecholamines, the major endogenous stimulators of lipolysis, are released from sympathetic nerves and bind to β-adrenergic receptors on the plasma membrane of adipocytes. Then, β-adrenergic receptor-coupled G-proteins stimulate adenylyl cyclases to generate cAMP and activate HSL through protein kinase A. Natriuretic peptides also promote lipolysis by a parallel pathway leading to the activation of protein kinase G in humans (Fig. 1.4) [75, 76].

The inflammatory cytokine TNF-α has been shown to induce lipolysis via MAPK p44/42 pathway and perilipin reduction. TNF-α also contributes to lipolysis via increasing insulin resistance of adipose cells [77]. Furthermore, TNF-α, IL-1β and IFN-γ were shown to induce lipolysis in cultured adipocytes [78], and they can inhibit expression of lipoprotein lipase, leading to decreased fatty acid storage in adipocytes [79]. Of note, insulin is an anti-lipolytic player in the regulation of lipolysis. It is the main anabolic factor for lipid storage of adipose tissue via inactivating cAMP and suppression of lipolysis (Fig. 1.4) [76].

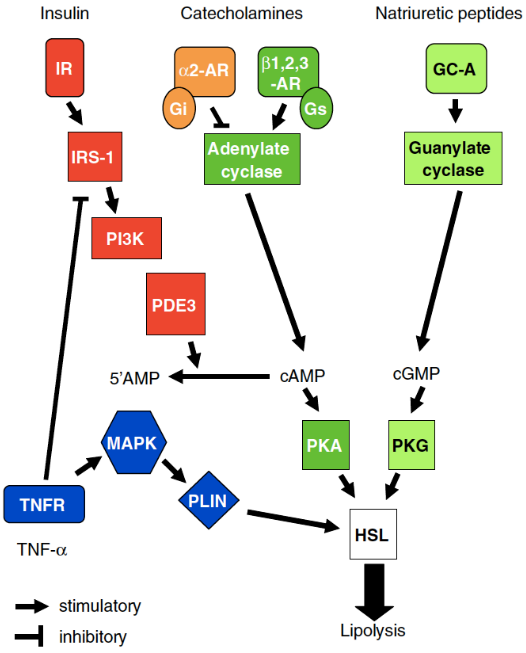

Figure 1.4: Schematic illustration of the major intracellular pathways affecting lipolysis. Insulin receptor (IR), insulin receptor substrates (IRS-1), phosphatidyl inositol-3 kinase (PI3K), phosphodiesterase 3 (PDE3), tumor necrosis factor-a receptor (TNFR), mitogen activated protein kinase (MAPK), perilipin (PLIN), α2-adrenoceptor (α2-AR), β-adrenoceptors 1, 2 and 3 (β1,2,3), cyclic AMP (cAMP), cyclic GMP (cGMP), protein kinase A (PKA), guanylyl receptor-A (GC-A), protein kinase G (PKG), hormone sensitive lipase (HSL) (figure is taken from Ryden *et al.* [76]).

In addition to lipolysis, browning can be stimulated in white adipose tissue (WAT) by IL-6 and PTHrP in cancer cachexia. Browning is a process in which white adipose cells acquire some of the molecular machinery that characterizes brown adipose cells. In this process, uncoupling protein expression is increased in white cells resulting in thermogenesis and energetic inefficiency [46, 80].

1.2.3.7 Brain

Skeletal muscle and adipose tissue are the main tissues affected in cancer cachexia, however, cachexia symptoms also target other organs, making cachexia a multi-organ syndrome. The brain is one of these organs and it is centrally involved in the control of food intake and appetite in cachexia. Inflammatory cytokines inhibit orexigenic (appetite-stimulating) pathways by mimicking the effect of leptin, and thereby suppressing the ghrelin and neuropeptide Y (NPY) signaling in the hypothalamus. Moreover, anorexigenic (appetite-suppressing) pathways are activated by inflammatory cytokines through increased activity of melanocortin and corticotropin-releasing factor, leading to decreased food intake [54].

1.2.3.8 Liver

As described in section 1.2.3.4, the most prominent change in the liver during cachexia is the induction of AAPR by inflammatory factors, especially IL-6. Besides, increased hepatic gluconeogenesis was detected in the liver of cancer patients possibly due to the flow of amino acids from skeletal muscle to the liver as a consequence of muscle wasting [81]. Hepatic steatosis has been observed in cancer cachexia patients [82]. Later, increased TG storage was also detected in liver as a result of adipose wasting in CAC. Receptor-interacting protein 140 (RIP140) might be important in the regulation of TG metabolism during cachexia, as increased RIP140 was observed in tumor mice, and liver-specific knockdown of RIP140 ameliorated hepatic steatosis [83].

1.2.3.9 Heart

Cardiac muscle changes have been reported in some tumor models of cachexia. In a rat tumor model, animals had a decrease in heart weight and showed functional changes comparable to congestive heart failure [84]. In the C26 colon cancer cachexia model, cardiac atrophy has been shown to depend on ActRIIB receptor signaling which might be activated by myostatin, activin, and growth/differentiation factor 11 [85]. Furthermore, in the C26 mouse model, several cardiac alterations such as marked fibrosis, disrupted myocardial ultrastructure and altered composition of contractile proteins have been observed [86].

1.2.4 Treatment approaches in cancer cachexia

For the treatment of cachexia, different approaches have been evaluated including the blocking of immune responses, improving food intake or inhibiting cachectic mediator signaling. It has been shown that a multimodal approach including nutrition support and exercise should be applied in the management of cachexia in the clinic [87]. To increase the food intake, some agents such as ghrelin agonists or melanocortin-4 receptor antagonists should be used since they are able to reverse tissue wasting, especially when reduced food intake is the primary cause [88-90]. In addition, oral application of eicosapentaenoic acid (present in fish oil) stabilized body weight in pancreatic cancer patients, and reduced the acute-phase response through the suppression of IL-6 [91, 92].

Different agents have been tested to inhibit inflammatory cytokines and associated pathways. Inhibition of TNF-α using the anti-TNF-α antibody infliximab did not give promising results in pancreatic and non-small cell lung cancer patients [93, 94], however, thalidomide application in esophageal cancer patients improved the amount of lean body mass [95]. Additionally, targeting IL-6 with an IL-6 receptor antibody was sufficient to stop weight loss but did not recover protein synthesis in an animal model of colon cancer cachexia [96]. Another IL-6 receptor antibody, tocilizumab, increased survival via recovering body weight and food intake in murine model of CAC [97]. An additional therapy option for muscle wasting is treatment with ActRIIB antagonists to block myostatin or activin binding. This approach restored muscle mass and prolonged survival in animal models [85].

Taken together, in the treatment of cachexia with a multi-factorial approach potentially gives the best results since one-sided targeting might not be enough to overcome the disease. However, multimodal therapy requires optimized and coordinated efforts in clinical oncology, early intervention, supportive care, nutritional support, and exercise together with multidisciplinary teamwork [87].

1.3 Adipose tissue and macrophages

Adipose tissue is the organ that mainly reserves energy and serves as a major source of metabolic fuel for whole body energy homeostasis. Adipocytes, which make up the bulk part of the tissue, store TG in periods of energy excess and use this storage when energy is needed. Additionally, adipose tissue has endocrine and paracrine functions as a secretory organ. Adipocytes secrete lipids (e.g. fatty acids and glycerol) and proteins (e.g adipo- and cytokines), which are important regulators of appetite, insulin sensitivity, inflammation, and angiogenesis [98, 99].

Adipocytes constitute the majority of the cell population in the adipose tissue whereas the non-adipocyte fraction contains preadipocytes, fibroblasts, endothelial cells, and cells of the immune cells, primarily macrophages, T cells, natural killer cells and mast cells. Macrophages are innate immune cells which can be polarized for different functional states by stimuli from the microenvironment. ‘Classically activated’ macrophages are stimulated by pro-inflammatory cytokines such as IFN-γ and TNF-α or lipopolysaccharide (LPS), and they produce pro-inflammatory cytokines. ‘Alternatively activated’ macrophages are polarized by IL-4 and IL-13, and show anti-inflammatory characteristics. In human adipose tissue, macrophage phenotypes were found equivalent in a normal state [100].

In obesity, it has been shown that macrophage infiltration into WAT increases, and macrophage number can reach up to 15-30% of adipocytes (where it counts 5-10% in healthy state) [99]. This increased abundance is a potential consequence of uncontrolled fatty acid flux originated from the basal lipolysis of the adipose tissue. In addition, during adipose tissue expansion, hypoxic areas emerge, leading to apoptosis of adipocytes and infiltration of macrophages for phagocytosis of cell debris [101, 102]. The adipose tissue macrophages (ATM) recruited to adipose tissue during high-fat feeding expressed IL-6, inducible nitric oxide synthase (iNOS), and C-C chemokine receptor type 2 (CCR2), indicating the classically activated phenotype and leading to a state of chronic inflammation [103]. Of note, chronic inflammation in adipose tissue reduced insulin sensitivity and induced insulin resistance [104]. In addition to these observations, Lumeng *et al.* reported that in adipose tissue of lean mice, macrophages express arginase-1 and IL-10, reminiscent of the alternatively activated phenotype. However, after high-fat diet the phenotype of ATM shifted to classical activation where macrophages increased the expression of TNF-α and iNOS [105].

Based on the knowledge that in obesity ATM number increases and macrophages show an inflammatory phenotype, one could speculate that weight loss has an opposite effect, i.e. reduced number of ATMs and lower inflammation. Confirming this assumption, patients after gastric bypass surgery and weight loss showed decreased ATM abundance and anti-inflammatory features [106]. However, a mouse model showing the role of macrophages in gradual weight loss emphasized that lipid fluxes are central regulators of ATM recruitment. Kosteli *et al.* revealed that weight loss led to increased macrophage recruitment in short term, but decreased ATM content in prolonged weight loss [107]. Overall, macrophages are able to impact on adipose tissue in varied ways and emerge as critical regulators of adipose tissue during health and disease.

1.4 Hypoxia-inducible factor 1 (HIF-1)

Oxygen is indispensable for the metabolism of eukaryotic cells. Reduced oxygen levels (hypoxia) occur physiologically during embryonic development and pathophysiologically during conditions such as arthritis, wound healing, atherosclerosis, chronic infections, and tumors. Hypoxia-inducible factors (HIFs) are the main mediators of the adaptive response of cells to hypoxia. HIFs are heterodimeric DNA binding transcription factors containing two basic helix-loop-helix domains: The oxygen sensing ‘α’ subunits (HIF-1α, HIF-2α, and HIF-3α) and a ‘β’ subunit (HIF1-β), which is constitutively expressed [108].

The activity of HIF-1 (heterodimer of HIF-1α and HIF1-β) is post-translationally regulated through hydroxylation of either proline residues in HIF-1α by prolyl hydroxylase domain enzymes (PHD) or asparagine residue in HIF-1α by factor inhibiting HIF-1 (FIH) [109]. These hydroxylation reactions require the presence of oxygen and α-ketoglutarate as substrates. In oxygen rich environments, the hydroxylated subunit is bound by the von Hippel–Lindau (VHL) tumor suppressor protein, followed by E3 ubiquitin–ligase recruitment and proteosomal degradation of HIF-1α. Under hypoxic conditions, inhibited PHD activity provides the stabilization of HIF-1α and afterwards translocation to nucleus. In the nucleus, HIF-1α dimerizes with HIF1-β and together with p300/CBP (CREB-binding protein) binds to the hypoxia response element motif in the promoters of target genes, regulating their transcription (Fig. 1.5) [110]. HIF-1 activates the transcription of different genes that regulate angiogenesis, inflammation and glucose metabolism, cell proliferation, and metastasis [111].

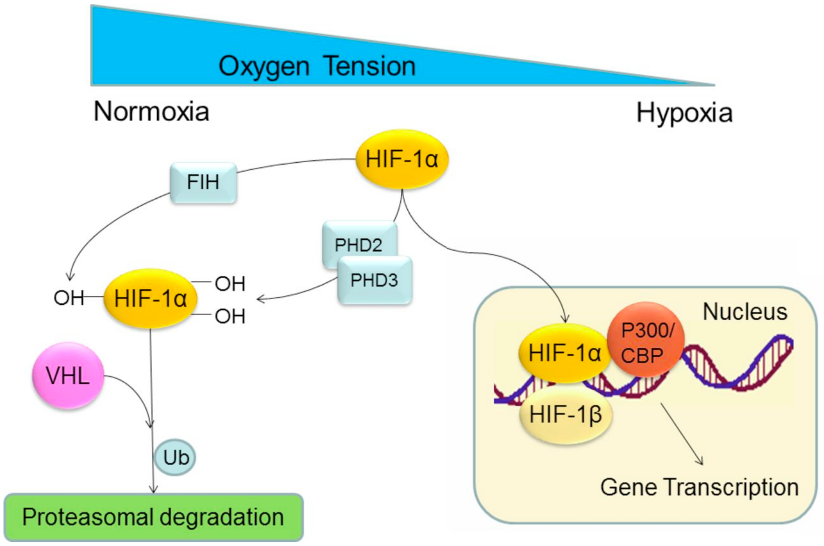

Figure 1.5: Description of HIF-1 regulation. Under normoxic conditions, HIF-1α is hyroxylated followed by VHL binding and proteasomal degradation. Under hypoxia, hydroxylase activity is significantly reduced and accumulating HIF-1α combines with HIF1-β and binds to DNA target sequences together with co-factors, such as the p300/CBP (Figure is taken from Tal *et al.* [112]).

In addition to oxygen-dependent regulation, HIF stabilization is also possible via cytokines, reactive oxygen species or mutations in various tumor suppressor and oncogenes [113]. Activation of PI3K and MAPK/ERK pathways by signaling through tyrosine kinases or G protein-coupled receptors can increase the HIF-1α protein levels, eventually increasing HIF-1 activity [111].

In many types of human cancers, HIF-1α overexpression has been shown on the protein level. In cervix, breast, brain, ovary, uterus, and gastrointestinal tumors, high levels of HIF-1α are significantly associated with mortality [111]. In HCC, significantly elevated protein levels were also positively associated with reduced survival and enhanced metastatic potential [114]. However, decreased mortality was observed in neck and non-small-cell lung cancer patients with HIF-1α overexpression suggesting that the effect of HIF-1α upregulation is dependent on the cancer type and the combination of mutations involving apoptotic and/or survival factors [111].

In innate immune cells, in addition to canonical activation, HIF activity has been found to be regulated independent from hypoxia in case of inflammation or in response to infectious microorganisms. In macrophages, HIF-1α stabilization was observed after bacterial infection under normoxic conditions [115]. Interestingly, LPS, a potent inducer of pro-inflammatory responses in macrophages, induced HIF-1α protein accumulation in macrophages [116]. This HIF-1α accumulation was a result of increased messenger ribonucleic acid (mRNA) transcription through the NF-κB pathway, which is independent from hypoxia-related post-translational regulation [117]. Besides LPS, the pro-inflammatory cytokine TNF-α was described to induce HIF-1α expression in wound macrophages under normoxia [118]. Additionally, HIF-1α deletion in macrophages of mice caused impaired inflammatory responses. Myeloid cell depletion of HIF-1α resulted in impaired aggregation, invasion, and motility in response to bacterial infection, which were related to metabolic defects such as decreased glycolysis and energy generation, altogether indicating the importance HIF-1α in the regulation of myeloid cell-mediated inflammation [119].

1.5 Aim of the study

Cachexia has been a significant problem for the clinical management of chronic diseases for a long time, especially for cancer patients. Most of the studies in cachexia research focused on skeletal muscle wasting and atrophy mechanisms due to the negative physical effect of muscle loss on patients' quality of life. However, accumulating evidence in recent years have shown the importance of fat loss for energy metabolism of cancer cachexia patients.

Cancer cachexia has been mainly addressed in solid tumors such as gastrointestinal, pancreatic, and lung cancer, yet not in liver cancer apart from few studies. The first aim of this project was to investigate cachexia in liver cancer using a HCC mouse model and to address whether cachexia induces any morphological, metabolic or molecular changes during development of liver cancer.

Increased inflammation, a hallmark of cachexia, is important in the course of diseases affecting peripheral organs. Tumor cells and immune cells, especially activated macrophages, are suggested to be the source of increased cachexia-associated inflammation. As a second aim of this project, considering the involvement of HIF-1α in the regulation of inflammatory responses, we investigated the effect of HIF-1α in tumor and myeloid cells in the course of liver CAC.

2 Materials

2.1 Animals

Strain name	**Features**
C57BL/6	C57BL/6J mice from Jackson laboratory
ASV-B	C57BL/6J background, SV40 oncogene expressed in Y chromosome under control of the liver specific anti-thrombin III gene
ASV-B Hif1a^{HC}	C57BL/6J background, SV40 oncogene expressed in Y chromosome under control of the liver specific anti-thrombin III gene Floxed exon 2 of *Hif1a* and Cre expression under control of the Lysozyme M gene resulting in myeloid cell-specific expression
ASV-B Hif1a^{MC}	C57BL/6J background, SV40 oncogene expressed in Y chromosome under control of the liver specific anti-thrombin III gene Floxed exon 2 of *Hif1a* and Cre expression under control of the Albumin gene resulting in hepatocyte-specific expression

2.2 Cells

Name	**Type**	**Source**
L929 cells	Cell line	The American Type Culture Collection
Bone marrow derived macrophage (BMDM) cells	Primary cells	BMDMs were isolated from mice as described in Section 3.6.2.

2.3 Antibodies

2.3.1 Primary antibodies

Name	**Catalog no**	**Manufacturer**	**Application**
Actin	A5441	Sigma	WB (1:5000)
F4/80	14-4801	eBioscience	IF (1:2000)
Ki67 (D3B5)	12202	Cell Signaling Technology	IF (1:3000)
Tyrosine Hydroxylase	AB152	Millipore	WB (1:2000)
Ym1	01404	StemCell Technologies	IF (1:5000)

WB: Western blot, IF: Immunofluorescence

2.3.2 Secondary antibodies

Name	**Catalog no**	**Manufacturer**	**Application**
Anti-Mouse	7076	Cell Signaling	WB (1:5000)
Anti-Rabbit	7074	Cell Signaling	WB (1:5000)
ImmPRESS HRP Anti-Rabbit IgG (Peroxidase)	MP-7401	Vector Lab	IF
ImmPRESS™ HRP Anti-Rat IgG, Mouse adsorbed (Peroxidase)	MP-7444	Vector Lab	IF

WB: Western blot, IF: Immunofluorescence

2.4 Buffers and solutions

Name	**Recipe**	**Application**
Ammonium-Chloride-Potassium lysing buffer (pH 7.3)	150 mM NH_4Cl 10 mM $KHCO_3$ 0.1 mM EDTA	Erythrocytes lysis
Blocking buffer	5% (w/v) milk powder in TBS-T	Western blot
Caspase activity measurement buffer	100 mM HEPES (pH 7.5) 10% (w/v) Sucrose 0.1% (w/v) CHAPS 2% (v/v) DMSO 10 mM DTT 50 µM fluorogenic Caspase-Substrate ± 100 µM Caspase-Inhibitor	Apoptotic activity measurement
Caspase lysis buffer	100 mM HEPES (pH 7.5) 10% (w/v) Sucrose 0.1% (v/v) IGEPAL® CA-630 10 mM DTT 1 Tablet Complete Mini	Apoptotic activity measurement
Krebs-Ringer buffer (pH 7.4)	12 mM HEPES (pH 7.5) 4.9 mM KCl 121 mM NaCl 1.2 mM $MgSO_4$ 0.33 mM $CaCl_2$ 3.5% (w/v) BSA (fatty acid-free) 0.1% (w/v) Glucose	*Ex vivo* lipolysis assay
Proteasome activity measurement buffer	50 mM Tris (pH 8,0) 0.5 mM EDTA 40 µM fluorogenic Proteasome-Substrate ± 40µM MG-132	UPS activity measurement
Proteasome lysis buffer	10 mM Tris (pH 7.5) 1 mM EDTA 2 mM ATP 20% (v/v) Glycerol	UPS activity measurement

	4mM DTT	
RIPA lysis buffer	10 mM Tris-HCl (pH 7.5) 150 mM NaCl 0.25% SDS 1% sodium deoxycholate 1% Nonidet P40 add solution directly before use: 2 mM PMSF 1 mM DTT 10 mM NaF 1 mM Na_3VO_4 2 µM Leupeptin 4,4x10^{-4} TIU/ mg Aprotinin	Protein extraction
Running buffer	25 mM Tris 190 mM Glycine 0.1% (w/v) SDS	SDS-PAGE
Separation buffer, 4x (pH 8.8)	1.5 M Tris-HCl 0.4% (w/v) SDS	SDS-PAGE
Stacking buffer, 4x (pH 6.8)	0.5 M Tris 0.4% (w/v) SDS	SDS-PAGE
Transfer buffer	25 mM Tris 192 mM Glycine 20% (v/v) methanol	Western blot
Tris-buffered saline-Tween 20 (TBS-T)	50 mM Tris-HCl (pH 7.5) 100 mM NaCl 0.05% (v/v) Tween 20	Western blot

UPS: Ubiquitin-proteasome system, SDS-PAGE: SDS-polyacrylamide gel electrophoresis

2.5 Chemicals and reagents

Chemical/Reagent name	Catalog no	Manufacturer
Adenosine 5’-triphosphate di sodium salt (ATP)	A6419	Sigma Aldrich, St. Louis, USA
Agarose Serva Wide Range	11406.02	Serva, Heidelberg, Germany
Albumin Fraction V	8076.3	Carl Roth, Karlsruhe, Germany
Albumin Fraction V, fatty acid-free	0052.2	Carl Roth, Karlsruhe, Germany
Albumin from bovine serum (BSA), protein standard	P0914	Sigma Aldrich, St. Louis, USA
Amplification Diluent, 1x	FP1498	PerkinElmer, Waltham, USA
Aprotinin	A162.2	Carl Roth, Karlsruhe, Germany
AR6 buffer, 10x	AR600250ML	PerkinElmer, Waltham, USA
CHAPS	17038.02	Serva, Heidelberg, Germany
cOmplete Tablets, Mini EASYpack	04693124001	Roche Diagnostics, Basel, Switzerland
Dako Antibody diluent	S3022	Dako, Carpinteria, USA
Dako Target retrieval solution	S1699	Dako, Carpinteria, USA
DAPI Spectral	FP1490	PerkinElmer, Waltham, USA
Diethyl dicarbonate (DEPC)-Treated water	AM9906	Thermo Fisher Scientific, Waltham, USA

Dithiothreitol (DTT)	6908.2	Carl Roth, Karlsruhe, Germany
DTT solution (1M)	43816	Sigma Aldrich, St. Louis, USA
di-Sodium hydrogen phosphate	P030.2	Carl Roth, Karlsruhe, Germany
Dimethyl sulfoxide (DMSO) for cell culture	A3672,0100	AppliChem, Darmstadt, Germany
DNA Ladder, GeneRuler 100bp	SM0242	Thermo Fisher Scientific, Waltham, USA
DNA Loading Dye, &x	R0611	Thermo Fisher Scientific, Waltham, USA
DNA Stain Clear G	39804.02	Serva, Heidelberg, Germany
Dnase I	AM2222	Thermo Fisher Scientific, Waltham, USA
Dnase I Buffer (10X)	8170G	Thermo Fisher Scientific, Waltham, USA
Deoxynucleotide (dNTP) Mix 10 mM each	R0192	Thermo Fisher Scientific, Waltham, USA
EDTA solution pH:8 (0.5M)	EMR034500	EuroClone, Pero, Italy
Ethanol, absolute + MEK	7124094	Fischar, Saarbrücken, Germany
Ethanol, absolute	20821.330	VWR, Fontenay-sous-Bois, France
Ethylene diamine tetraacetic acid (EDTA)	ED-100G	Sigma Aldrich, St. Louis, USA

Eosin Y (yellowish)	1159350025	Merck Millipore, Darmstadt, Germany
Fetal bovine serum (FBS)	10270-106	Thermo Fisher Scientific, Waltham, USA
Formaldehyde, 4%	6338015	Otto Fischar, Saarbrücken, Germany
Formaldehyde, 37%	252549-500	Sigma Aldrich, St. Louis, USA
Glutamax 100X	35050-038	Gibco Life Technologies, Paisley, UK
Glycerol	7530.1	Carl Roth, Karlsruhe, Germany
Glycine	A1067,1000	AppliChem, Darmstadt, Germany
Hematoxylin	72804	Thermo Fisher Scientific, Waltham, USA
HEPES buffer solution (1 M)	15630-056	Gibco Life Technologies, Paisley, UK
Hydrogen chloride (HCl)	141020.1211	AppliChem, Darmstadt, Germany
IGEPAL® CA-630	I8896	Sigma Aldrich, St. Louis, USA
Isopropanol	20842.330	VWR, Fontenay-sous-Bois, France
Leupeptin Hemisulfate	CN33.2	Carl Roth, Karlsruhe, Germany
Lipopolysaccharides from *Escherichia coli* (LPS)	L2755	Sigma Aldrich, St. Louis, USA

Maxima RT 10.000 units	EP0742	Thermo Fisher Scientific, Waltham, USA
MG-132	B-200	Boston Biochemicals
Methanol	20847.295	VWR, Fontenay-sous-Bois, France
Milk powder	T145.3	Carl Roth, Karlsruhe, Germany
Mouse Interferon-γ (Ifn-γ) Recombinant Protein	14-8041-62	eBioscience, San Diego, USA
Mouse Interleukin-4 (Il-4) Recombinant Protein	14-8311-63	eBioscience, San Diego, USA,
Nonidet P40	A1694,0250	AppliChem, Darmstadt, Germany
NucleoZOL	740404.200	Macherey-Nagel, Düren, Germany
NuPAGE® LDS sample buffer (4x)	NP0007	Thermo Fisher Scientific, Waltham, USA
Oligo deoxy-thymidine (dT) 18 Primer	SO132	Thermo Fisher Scientific, Waltham, USA
Opal 520 Reagent Pack	FP1487001 KT	PerkinElmer, Waltham, USA
Opal 570 Reagent Pack	FP1488001 KT	PerkinElmer, Waltham, USA

Penicillin/Streptomycin (Pen-Strep)	A2212	Merck Millipore, Darmstadt, Germany
Phosphate buffered saline (PBS) powder	L182-50	Merck Millipore, Darmstadt, Germany
Phosphate buffered saline w/o Ca^{2+} and Mg^{2+} (PBS)	14190-094	Thermo Fisher Scientific, Waltham, USA
Potassium chloride (KCl)	6781.3	Carl Roth, Karlsruhe, Germany
Potassium dihydrogen phosphate (KH_2PO_4)	3904.2	Carl Roth, Karlsruhe, Germany
Power SYBR™ Green PCR Master Mix (2X)	4367662	Applied Biosystems, Warrington, UK
Quick Start™ Bradford Dye	5000205	Bio-Rad, Hercules, USA
Random Hexamer	SO142	Thermo Fisher Scientific, Waltham, USA
Rotiphorese® Gel 30 Acrylamide solution	3029.1	Carl Roth, Karlsruhe, Germany
Rotiphorese® 50x Tris Acetate EDTA (TAE) Buffer	CL86.2	Carl Roth, Karlsruhe, Germany
RPMI 1640 medium	21875-034	Thermo Fisher Scientific, Waltham, USA
RT Buffer (5x)	EP0742	Thermo Fisher Scientific, Waltham, USA

SERVA Triple Color Protein standard III	39258	Serva, Heidelberg, Germany
Sodium chloride (NaCl)	A1371,5000	Carl Roth, Karlsruhe, Germany
Sodium deoxycholate	3484.3	Carl Roth, Karlsruhe, Germany
Sodium dodecyl sulfate (SDS)	2326.3	Carl Roth, Karlsruhe, Germany
Sodium fluoride (NaF)	2618.1	Carl Roth, Karlsruhe, Germany
Sodium hydroxide (NaOH)	P031.1	Carl Roth, Karlsruhe, Germany
Sodium orthovanadate (Na_3VO_4)	A2196,0010	AppliChem, Darmstadt, Germany
Sucrose	S7903	Sigma Aldrich, St. Louis, USA
TBST	S3306	Dako, Carpinteria, USA
TEMED(N,N,N´,N´-tetramethylethylendiamin)	2367.3	Carl Roth, Karlsruhe, Germany
Trichlormethan/Chloroform	7331.2	Carl Roth, Karlsruhe, Germany
TRIS	5429.5	Carl Roth, Karlsruhe, Germany
Triton™ X-100	3051.3	Carl Roth, Karlsruhe, Germany
Trypan Blue Stain	15250-061	Thermo Fisher Scientific, Waltham, USA
Trypsin EDTA solution	L2143	Merck Millipore, Darmstadt, Germany
Tween®-20	P1379-500	Sigma Aldrich, St. Louis, USA

Western Lightning™ Plus-ECL	NEL103E001EA	Perkin Elmer, Waltham, USA
VECTASHIELD HardSet Antifade Mounting Medium	H-1400	Vector Lab, Burlingame, USA
Vitro-Clud®	04-0001	R.Langenbrinck, Emmendingen, Germany

2.6 Consumables

Name	**Catalog no**	**Manufacturer**
Amersham Protran Premium 0.2µm nitrocellulose membrane	10600004	GE Healthcare, Freiburg, Germany
Cell Strainer, 100 µm	431752	Corning, Durham, USA
Corning® Ultraviolet (UV)-Transparent Microplates	CLS3635	Sigma Aldrich, St. Louis, USA
Coverslip AutomatStar24x60mm	k12460a1,0	Engelbrect, Edermünde, Germany
Filter paper (Gel dryer)	1650962	Bio-Rad, Hercules, USA
Micro tube K3E	41.1504.005	Sarstedt, Nümbrecht, Germany
Micro tube Z-Gel	41.1500.005	Sarstedt, Nümbrecht, Germany
Plastic Petri Dish (92x16mm)	82.1472.001	Sarstedt, Nümbrecht, Germany

Superfrost Plus™ Adhesion Microscope Slides	J1800AMNT	Menzel, Braunschweig, Germany
22G needle	4657624	Braun, Melsungen, Germany
27G needle	4657705	Braun, Melsungen, Germany

2.7 Kits

Name	**Catalog no**	**Manufacturer**
Bio-Plex Pro™ Mouse Th17 Assay Panel A 6-Plex	M6000007NY	Bio-Rad, Hercules, USA
DC™ Protein Assay Kit I	5000111	Bio-Rad, Hercules, USA
iScript™ cDNA Synthesis Kit	170-8897	Bio-Rad, Hercules, USA
Glycerol Colorimetric Assay Kit	10010755	Cayman, Michigan, USA
Ketone Body Assay Kit	MAK134-1KT	Sigma Aldrich, St. Louis, USA
Taq PCR Master Mix Kit	201445	Qiagen, Hilden, Germany

2.8 Primers

2.8.1 Genotyping primers

Gene	**Primer Sequence**	**Product length (bp)**	**T_a (°C)**	**Working concentration (nM)**
SV40	**F:** ACTTTGGAGGCTTCTGGGAT **R:** GGTGTAAATAGCAAAGCAAGCA	618	60	200
Cre	**F:** GCCAGCTAAACATGCTTCATC **R:** ATTGCCCCTGTTTCACTATCC	750	58	200
Hif1a	**F:** GGAGCTATCTCTCTAGACC **R:** GCAGTTAAGAGCACTAGTTG	200 (WT) 250 (KO)	57	200

(WT: wild-type, KO: knockout)

2.8.2 Quantitative polymerase chain reaction primers

Gene	**Primer Sequence**	**Product length (bp)**	**T_a (°C)**	**Working concentration (nM)**
B2m	**F:** TTCTGGTGCTTGTCTCACTGA **R:** CAGTATGTTCGGCTTCCCATTC	104	61	500
Ucp1	**F:** AAGCTGTGCGATGTCCATGT **R:** AAGCCACAAACCCTTTGAAAA	65	58	500
Pgc1a	**F:** AGACAAATGTGCTTCGAAAAAGAA **R:** GAAGAGATAAAGTTGTTGGTTTGGC	83	60	500
Pparg	**F:** CAAGAATACCAAAGTGCGATCAA **R:** GAGCTGGGTCTTTTCAGAATAATAAG	69	60	500

Prdm16	**F:** GCACGGTGAAGCCATTCATATG **R:** TCGGCGTGCATCCGCTTGTG	88	58	500
Cidea	**F:** GCTTCAAGGCCGTGTTAAGG **R:** CGTCATCTGTGCAGCATAGG	59	60	500
Arg1	**F:** CTCCAAGCCAAAGTCCTTAGAG **R:** AGGAGCTGTCATTAGGGACATC	185	60	500
Mrc1	**F:** TGATTACGAGCAGTGGAAGC **R:** GTTCACCGTAAGCCCAATTT	126	60	500
Clec10a	**F:** GGCACAAAACCCAGCAAGAC **R:** TGGGACCAAGGAGAGTGCTA	193	61	500
Il10	**F:** GCTCTTACTGACTGGCATGAG **R:** CGCAGCTCTAGGAGCATGTG	105	60	500
Tnfa	**F:** CCATTCCTGAGTTCTGCAAAGG **R:** AGGTAGGAAGGCCTGAGATCTTATC	85	59	500
Nos2	**F:** AAGCCCCGCTACTACTCCAT **R:** AAGCCACTGACACTTCGCA	191	59	500
Cd274	**F:** CTCGCCTGCAGATAGTTCCC **R:** GTCCAGCTCCCGTTCTACAG	172	59	500
Lipe	**F:** TGTCACGCTACACAAAGGCT **R:** GGTCACACTGAGGCCTGTC	148	60	250

2.8.3 Design of primers

For browning marker genes *Ucp1, Pgc1a, Pparg Prdm16, Cidea* [46] as well as Mrc1 [120] published primer sequences were used. The rest of the primers were designed using NCBI Primer Blast tool with the following parameters: 1) PCR product size of 70 - 250 bp, 2) Primer T_m of 57 - 63°C, 3) Preference of primers spanning exon junctions, 4) Separation of primer pairs by at least one intron. The secondary structure tendencies of designed primer pairs were analyzed via the OligoAnalyzer 3.1

(Integrated DNA Technologies, USA) online tool. Product length and melting temperature (T_m) were calculated using the Oligonucleotide Properties Calculator (Northwestern University, Evanston, USA) website.

2.9 Substrates and inhibitors

Fluorogenic substrate name (Catalog No)	**Target Activity**	**Inhibitor (Catalog No)**	**Manufacturer**
Benzyloxycarbonyl-Leu-Leu-Glu-7-amido-4-methylcoumarin [Z-LLE-AMC] (BML-ZW9345-0005)	trypsin-like activity	MG-132 (BML-PI102-0005)	Enzo Life Sciences, Lörrach, Germany
Succinyl-Leu-Leu-Val-Tyr-7-amido-4-methylcoumarin [LLVY-AMC] (BML-P802-0005)	chymotrypsin-like activity	MG-132 (BML-PI102-0005)	Enzo Life Sciences, Lörrach, Germany
Benzoyl-Val-Gly-Arg-7-amidocoumarin [Bz-VGR-AMC] (BML-BW9375-0005)	peptidyl-glutamyl-protein-hydrolysing activity	MG-132 (BML-PI102-0005)	Enzo Life Sciences, Lörrach, Germany
Ac-DEVD-AMC (ALX-260-031-M005)	Caspase-3 activity	Ac-DEVD-CHO (ALX-260-030-M005)	Enzo Life Sciences, Lörrach, Germany

Ac-VEID-AMC (ALX-260-064-M005)	Caspase-6 activity	Ac-VEID-CHO (ALX-260-062-M005)	Enzo Life Sciences, Lörrach, Germany

2.10 Instruments

Instrument	**Manufacturer**
AxioImager M2 Imaging System	Zeiss, Oberkochen, Germany
Decloaking Chamber™ NxGen	Biocare Medical, Pacheco, USA
EchoMRI-700™ Nuclear magnetic resonance (NMR) spectroscopy	Echo Medical Systems LLC, Houston, USA
ECL ChemoCam Imager	Intas, Göttingen, Germany
Heracell150i CO_2 Incubator	Thermo Fisher Scientific, Waltham, USA
Leica DFC345 FX	Leica Mikrosystems, Wetzlar, Germany
Mini-PROTEAN Vertical Electrophoresis system	Bio-Rad, Hercules, USA
Multi-Axle-Rotating-Mixer RM 5	CAT M. Zipperer, Staufen, Germany
Professional TRIO Thermal Cycler	Analytik Jena, Jena, Germany
Qiagen LiquiChip 200 workstation	Qiagen, Hilden, Germany
SONOPULS Ultrasonic homogenizer UW3100	Bandelin Electronic, Berlin, Germany

Sub-Cell® GT Cell Horizontal Electrophoresis System	Bio-Rad, Hercules, USA
Synergy HT Multi-Mode Microplate Reader	BioTek, Winooski, USA
TomoScope 30s Duo micro-CT Imaging	VAMP, Erlangen, Germany
Turrax Homogenizer, T10 basic	IKA, Staufen, Germany
UV solo TS Imaging System	Analytik Jena, Jena, Germany
xMark™ Microplate Absorbance Spectrophotometer	Bio-Rad, Hercules, USA
Vectra 3.0 automated quantitative imaging system	PerkinElmer, Waltham, USA
7500 Real-Time PCR System	Applied Biosystems, Thermo Fisher Scientific, Waltham, USA

2.11 Computer programs

Name	**Application**	**Manufacturer**
Bio-Plex Manager software	Luminex® assay	Bio-Rad, Hercules, USA
Endnote X8	Reference management	Clarivate Analytics, Philadelphia, USA
Fiji - Adiposoft	Adipocyte cell size analysis	CIMA, University of Navarra
Gen5 Software	Microplate reader control	BioTek, Winooski, USA

GraphPad Prism 6.0	Figure preparation, statistical analysis	GraphPad Software, California, USA
ImageJ	Western blot	National Institute of Health, Washington, USA
inForm® Advanced Image Analysis Software	Cell quantification of multiple biomarkers	PerkinElmer, Waltham, USA
Microsoft Excel	Adipocyte cell size analysis	Microsoft, Washington, USA
Microwin 2000	Fluorescence measurement	BERTHOLD Technologies, Bad Wildbad, Germany
Vectra program	Automated quantitative imaging of tissues	PerkinElmer, Waltham, USA
7500 Software v2.0.5	7500 Real-Time PCR System control	Applied Biosystems, Thermo Fisher Scientific, Waltham, USA

3 Methods

3.1 Animals

All mice were housed and bred in the animal facility of the University Hospital RWTH Aachen. Mice were given sterile water and standard rodent chow *ad libitum* and were kept at constant room temperature (RT) (22±2°C) with a 12-hour light/dark cycle under specific pathogen-free conditions. All experiments were approved by local authorities (LANUV NRW, Germany) and conducted in accordance with the national and institutional guidelines for care, welfare, and treatment of animals.

3.1.1 ASV-B mice as a HCC animal model

ASV-B mice were initially developed by Evelyne Dubois and colleagues in 1991 [121]. The model was established via insertion of a 700-base pair regulatory sequence from the anti-thrombin III gene together with the SV40 large T antigen on the Y chromosome. The integration of anti-thrombin III gene promoter provides hepatocyte-specific expression and the SV40 large T oncogene initiates malignant transformation. HCC development is restricted to male mice due to integration of the transgene on the Y chromosome. ASV-B mice first were established as a hybrid line of C57BL/6J and 3DBA/2 background. Then, mice were backcrossed with C57BL/6J mice (>25 generations). In this model, pathological analysis confirmed that hepatocyte neoplasia occurs at age of 8 weeks, adenoma nodules are observed by the 12th week and diffuse hepatocarcinoma is detected at the age of 16 weeks whereas fibrosis does not occur in this model [122] (Figure 3.1).

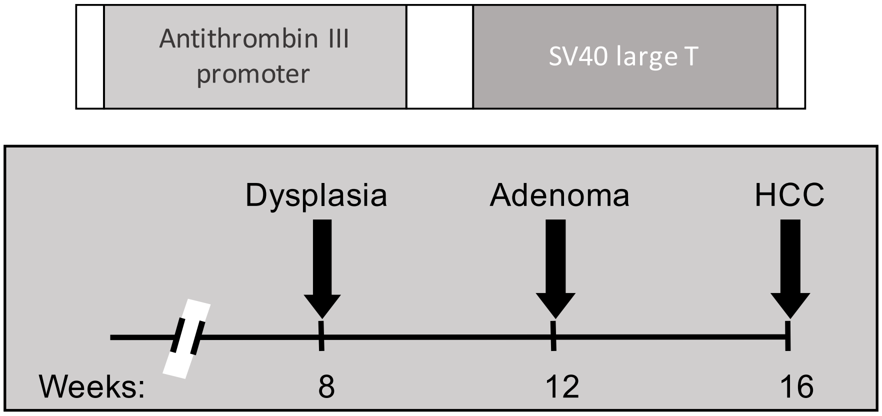

Figure 3.1: ASV-B mice general scheme. ASV-B mice express the SV40 large T antigen under control of the anti-thrombin III promoter on the Y chromosome (upper part). Tumor progression in ASV-B mouse liver in relation to age (lower part).

3.1.2 Hepatocyte- and myeloid cell-specific *Hif1a* knockout in ASV-B mice

ASV-B mice were obtained from the Inserm research institute (Paris, France) and bred to C57BL/6J mice carrying both alleles of the *Hif1a* gene flanked by loxP sites around exon 2 (Hif1a+^{f}/+^{f}). C57BL/6J Hif1a+^{f}/+^{f} mice were created and provided by Randall Johnson's group (University of California San Diego, La Jolla, USA) [123]. Then, conditional knockout of *Hif1a* gene was achieved via the Cre-loxP system. This system, in which the tissue-specifically expressed Cre recombinase is able to remove DNA sequences flanked by loxP sites, is used to get conditional knockout strains [124]. C57BL/6J AlbCre mice (expressing Cre recombinase driven by Albumin promoter, specifically in liver) and C57BL/6J LysMCre mice (expressing Cre recombinase driven by Lysozyme M promoter, specifically in myeloid cells) had been previously established and were provided by Randall Johnson [125, 126]. Hepatocyte-specific knockout of *Hif1a* in ASV-B mice was achieved by breeding male ASV-B Hif1a+^{f}/+^{f} mice with female C57BL/6 Hif1a+^{f}/+^{f} AlbCre mice.

Cre-positive male mice (ASV-B Hif1a+^{f}/+^{f} AlbCre+) were used as knockouts (termed ASV-B Hif1a^{HC}) and male littermates negative for Cre expression were used as wild-type controls (ASV-B WT).

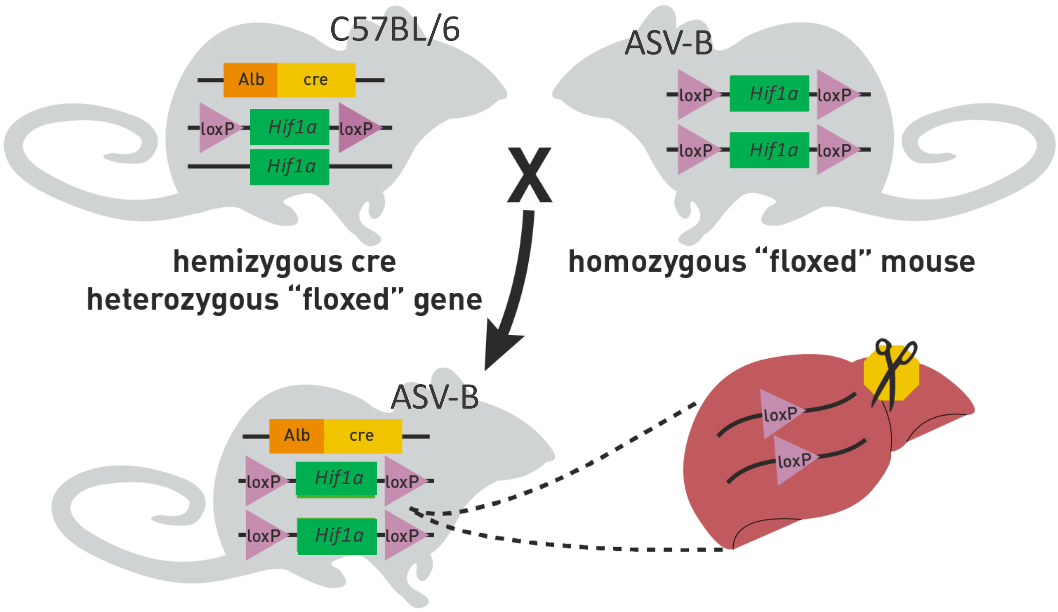

Figure 3.2: Schematic representation of Cre-loxP system for *Hif1a* knockout in liver cells. Figure was modified from The Jackson Laboratory (https://www.jax.org/news-and-insights/jax-blog/2011/september/cre-lox-breeding-for-dummies).

The myeloid cell-specific knockout of *Hif1a* in ASV-B mice was achieved by breeding male ASV-B Hif1a+^{f}/+^{f} mice with female C57BL/6 Hif1a+^{f}/+^{f} LysCre (Figure 3.3). Again, Cre-positive male mice (ASV-B Hif1a+^{f}/+^{f} LysMCre+) were used as knockouts (termed ASV-B Hif1a^{MC}) and male littermates negative for Cre expression were used as wild-type controls (ASV-B WT).

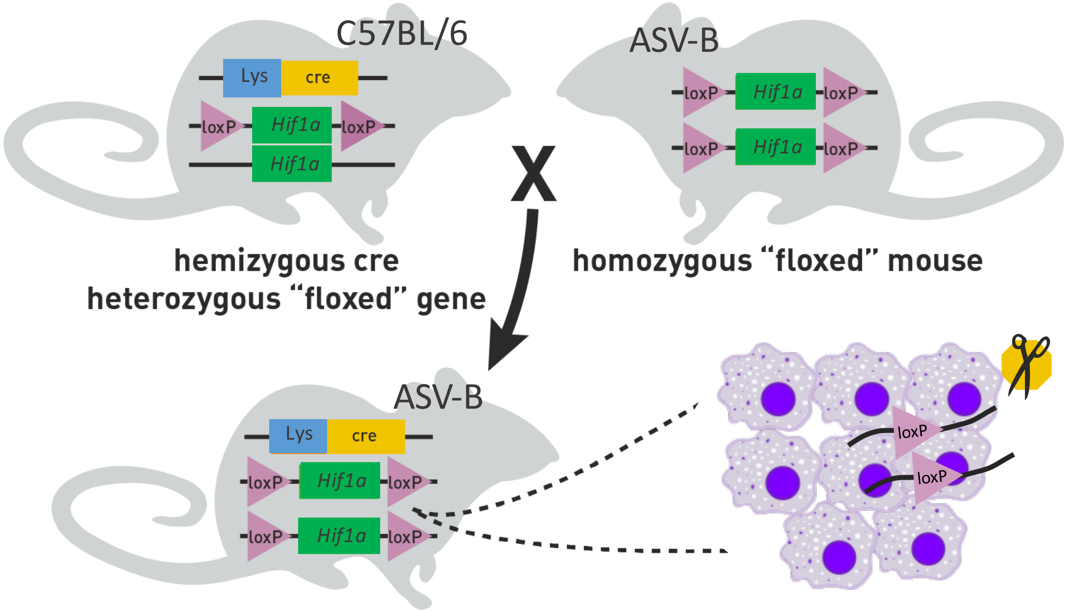

Figure 3.3: Schematic representation of Cre-loxP system for *Hif1a* knockout in myeloid cells (and macrophages in tissue). Figure was modified from The Jackson Laboratory (https://www.jax.org/news-and-insights/jax-blog/2011/september/cre-lox-breeding-for-dummies).

When indicated, male C57BL/6J mice (Jackson Laboratory) were used for control purposes in the experiments.

3.1.3 Tissue collection

Animals were sacrificed at 12, 16, and 18 weeks of age depending on the experimental setup. Following animal sacrifice by isoflurane and cervical dislocation, the abdominal cavity was immediately opened and blood was collected from the inferior vena cava using a 22G needle. Collected blood was used for serum isolation or directly sent to the Biochemistry Laboratory at the animal facility of the University Hospital RWTH Aachen. Afterwards, liver tissue, epididymal white adipose tissue (eWAT), skeletal muscle (gastrocnemius (GC), tibialis anterior (TA), soleus, and extensor digitorum longus (EDL)), as well as brain were excised and rapidly measured for weight. Collected tissues were either frozen in liquid nitrogen and stored at -80°C or fixed in 4% formaldehyde and later embedded in paraffin.

3.2 Monitoring and imaging of animals

3.2.1 Body weight, food intake and body composition measurements

Body weight and food intake of mice were measured weekly between the age of 12 and 18 weeks. Following body weight measurement, body composition was analyzed with the nuclear magnetic resonance (NMR) spectroscopy device EchoMRI-700™ (Echo Medical Systems LLC, Houston, USA) to measure total body fat and lean mass.

3.2.3 Computed tomography imaging of mice

Micro computed tomography (µCT) imaging of mice was performed using a dual-energy gantry-based flat-panel microcomputed tomography scanner (TomoScope 30s Duo, CT Imaging, Erlangen, Germany) in the Institute for Experimental Molecular Imaging, University Hospital RWTH Aachen in collaboration with the group of Univ.-Prof. Dr. Dr. Twan Lammers. The dual-energy X-ray tubes of the µCT were operated at voltages of 40 and 65 kV with currents of 1.0 and 0.5 mA, respectively. To cover the entire mouse, three sub-scans were performed, each of which acquired 720 projections with 1,032 × 1,012 pixels during one full rotation with durations of 90 s. 14 week old animals were sacrificed and immediately placed into the device. After acquisition, volumetric data sets were reconstructed using a modified Feldkamp algorithm with a smooth kernel at an isotropic voxel size of 35 µm. The fat-containing tissue regions, which appear hypo-intense in the µCT data, were segmented using an automated segmentation method with interactive correction of segmentation errors [127]. The volumetric fat percentage was computed as the ratio of (subcutaneous and visceral) fat volume to the entire body volume.

3.3 Hematological and biochemical methods

3.3.1 Blood count

After mice were sacrificed, 100 µl blood samples were collected into EDTA-tubes (EDTA micro tube, Sarstedt, Germany) and mixed by inverting. Complete blood count was performed via an automated analyzer in the Biochemistry Laboratory of the Institute for Laboratory Animal Science at the University Hospital RWTH Aachen.

3.3.2 UPS and apoptotic activities

To measure the catabolic activity in muscle at the biochemical level, the ubiquitin–proteasome system (UPS) and apoptotic activity assays were performed. For these assays, frozen gastrocnemius (GC) muscle tissues were first pulverized with a cooled mortar and pestle, then homogenized in lysis buffer. Protein extracts were kept at 4°C during the procedures.

3.3.2.1 GC tissue extraction

50 mg GC tissue powder was mixed with 200 µl of cold proteasome lysis buffer and homogenized on ice for 2 min. Later, the lysates were sonicated for 20 seconds and centrifuged at 13,000 *g* for 15 min at 4°C. Sonication and centrifugation steps were repeated and supernatant was collected afterwards. Protein concentration was determined by the Bradford assay and the rest of the supernatant was stored at -80°C until proteasome activity measurement.

For apoptotic activity assay, 150 µl of caspase lysis buffer was added to 50 mg GC tissue powder. The homogenates were subjected to three freeze/thaw cycles via freezing in liquid nitrogen and thawing at 37°C in a water bath. After that, samples were centrifuged at 20,000 *g* for 30 min at 4°C. Supernatants were collected and protein concentrations were determined by the Bradford assay. For caspase activity measurements, supernatants were stored at -80°C.

3.3.2.2 Bradford assay for quantification of protein concentration

The protein concentrations of the tissue extracts were determined using the Quick Start™ Bradford Dye Reagent (Bio-Rad). First, samples were diluted 1:20 with assay buffers. 5 µl of diluted samples were mixed with 250 µl Bradford dye and incubated at RT for 5 min in the dark. Optical density was measured at 595 nm wavelength using xMark™ Microplate Absorbance Spectrophotometer (Bio-Rad). BSA protein dilutions were used to generate standard curves and to calculate sample concentrations.

3.3.2.3 UPS activity assay

UPS activity was determined using fluorogenic substrates for trypsin-like, chymotrypsin-like, and peptidyl-glutamyl-hydrolyzing activity of the proteasome subunits. 100 µg protein was mixed with 40 µM fluorogenic substrate (listed in Section 2.8) in 75 µl proteasome activity measurement buffer with/without a proteasome inhibitor (MG132, 40 µM) and then completed to 150 µl by adding dH_2O. The cleavage of each substrate by the proteasome in the sample emitted fluorescence releasing the fluorogenic AMC. The fluorescence intensity was measured using black plates in fluorometer for 30 min in 3 min intervals at 37°C at 360 nm excitation and 460 nm emission wavelengths. Measurements with inhibitors were subtracted from measurements without inhibitors to calculate the actual amount of fluorescence. Enzyme activity was calculated using the free AMC standard curve and expressed as nmol/mg/min.

3.3.2.4 Apoptotic activity assay

Apoptotic activity was detected by measuring caspase-3 and caspase-6 activities using fluorogenic substrates. 100 µg protein was mixed with 50 µM fluorogenic substrate (listed in Section 2.8) in 75 µl caspase activity measurement buffer with/without 100 µM substrate inhibitor (listed in Section 2.9) and completed to 150 µl by adding dH_2O. The cleavage of each substrate by the caspases in the sample emitted fluorescence releasing the fluorogenic AMC. The emitted fluorescence was measured using black plates in fluorometer for 1 hour in 6 min intervals at 37°C at 360 nm excitation and 460 nm emission wavelength. Caspase activity was calculated by comparing fluorescence values to the standard curve of free AMC and showed as nmol/mg/min.

3.3.3 Luminex® assay for cytokine measurement from blood serum

Luminex® xMAP® technology uses a microsphere-based flow cytometric approach for multiplex analysis. It is based on the use of polystyrene or paramagnetic beads that are internally dyed with fluorophores of different intensities. Each bead is given a unique number and then, individual bead sets are coated with a capture antibody for one specific antigen. To measure and quantify multiple targets within a sample simultaneously, multiple antigen-specific beads can be combined and added to the sample in a 96-well plate format. Next, biotinylated detection antibodies are added to the mixture to form an antibody-antigen sandwich. Phycoerythrin (PE)-conjugated streptavidin binds to biotinylated detection antibodies and samples are analyzed in Luminex® instrument. Dual-laser flow-based detection system of the Luminex® instrument allows to detect the bead and identify the target using one laser and also allows to determine the magnitude of the PE-derived signal for quantification using a second laser (Figure 3.4).

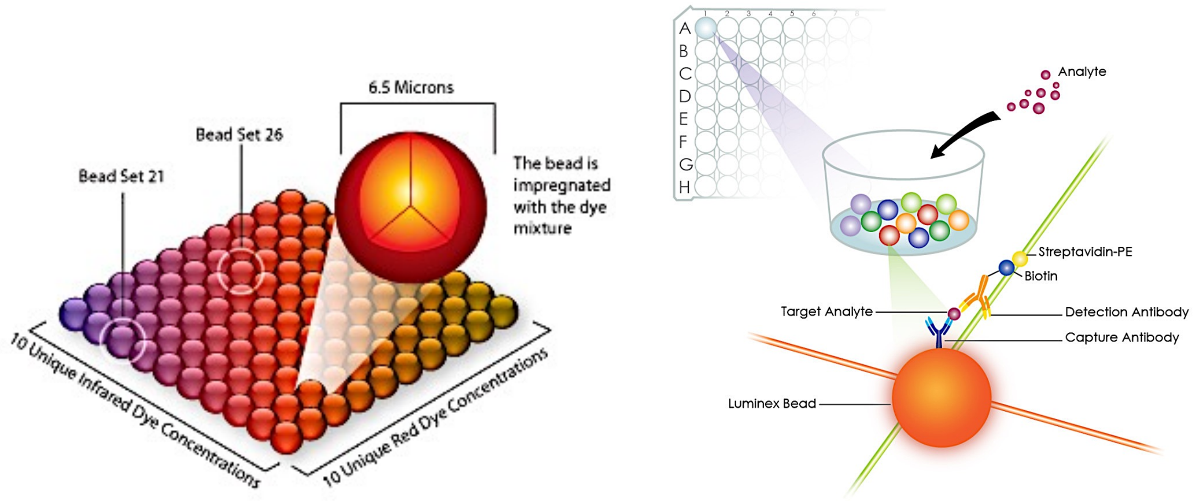

Figure 3.4: Illustration of beads and general assay principle of the Luminex® technology. (Figures were taken from https://www.thermofisher.com/de/de/home/life-science/protein-biology/protein-assays-analysis/luminex-multiplex-assays.html and https://whitesci.co.za/brand/rnd-systems/luminex-immunoassay-guide/).

500 µl blood was transferred to serum-gel Z tubes (Sarstedt, Germany), allowed to clot for 30 min at RT and centrifuged at 10,000 *g* for 5 min. The serum was collected and stored at -80°C until use. Samples were diluted 1:2 with Bio-Plex sample diluent and the fluorescence measurement of the beads was performed with the Qiagen LiquiChip 200 workstation (Qiagen, Hilden, Germany). The machine had been switched on one hour before the assay to warm up and calibrated using the calibration kit of Bio-Plex® system. A flat-bottom 96-well plate was used and washed manually using a magnetic plate. A standard curve was prepared as described in the manual and standards and samples were measured in duplicates. 50 µl beads together with 50 µl standard, diluted sample or blank (Bio-Plex sample diluent) were added to the wells and incubated in the dark for 1 hour at RT on a shaker. After incubation, beads were washed three times with 100 µl wash buffer and detection antibody mix of 25 µl was added to each well for another incubation of 30 min at dark at RT on shaker. Beads were washed again and 50 µl streptavidin-PE was added to the wells. After 10 min incubation at dark on a shaker, beads were washed and mixed with 125 µl assay buffer. Then the plate was immediately measured for fluorescence emission of the beads in the workstation. Cytokine concentrations were calculated using the Bio-Plex

Manager software (Bio-Rad, Hercules; CA USA) and reference standard values provided by the manufacturer.

3.3.4 *Ex vivo* lipolysis assay

eWAT were excised from 16 week old mice and cut into 20 mg pieces. Tissue pieces were put in 1.5 ml Krebs-Ringer buffer on ice until mouse dissection was completed. Then, tissues were transferred to 200 µl Krebs-Ringer buffer and incubated at 37°C for 4 hours together with a blank sample including only Krebs-Ringer buffer. Following incubation, samples were centrifuged at 21,000 *g* for 30 s and the supernatants were collected and stored at -20°C. From these supernatants, released glycerol was measured using the Glycerol Colorimetric Assay Kit (Cayman). Briefly, 10 µl of each supernatant and glycerol standard were added to a 96-well plate. Subsequently, 150 µl enzyme buffer solution was added into the wells to initiate the reaction. The enzyme buffer solution contains three enzymes (glycerol kinase, glycerol phosphate oxidase, peroxidase) in salt solution that will initiate a series of reactions to metabolize the glycerol and to produce a purple product (Quinoneimine dye) at the end. After 15 min incubation at RT, the plate was read at 540 nm absorbance in Synergy HT Multi-Mode Microplate Reader (BioTek, Winooski, USA) and glycerol amounts were calculated according to the standard curve.

3.3.5 Catecholamine measurement

Catecholamine amounts were measured with high-performance liquid chromatography (HPLC). eWAT tissue was excised from 16 week old mice and frozen. Later, 100 g tissue was sonicated in 200 µl 0.3 M perchloric acid for 30 s on ice. Then, samples were centrifuged at 7,600 *g* for 10 min at 1°C. Supernatants, cleaned from residue, were collected and used for measurement in HPLC system. Cell culture media supernatants were collected from bone marrow-derived macrophage (BMDM) cells and stored at -80°C until directly injected into the system. All measurements were performed by a service laboratory with special HPLC expertise (Laboratory for Stress Monitoring, Hardegsen, Germany) (http://lsm-speziallabor.de/fr_home.html).

3.3.6 Protein analysis

3.3.6.1 Protein extraction from tissue

50 mg frozen eWAT samples were pulverized using precooled metal mortar and pestle. Tissues were homogenized in 100 µl RIPA buffer and sonicated for 20 s for 6 cycles at 10% power. Later, samples were put on ice for 1 hour and were centrifuged for 15 min at 12,000 *g* at 4°C. The fat layer on top of the sample was discarded and supernatant was transferred to a new tube using a 27G needle. The centrifuge step was repeated twice more to remove fat from samples and clean lysates were transferred to clean tubes.

3.3.6.2 Lowry assay for quantification of protein concentration

The protein concentrations were determined using colorimetric DC Protein Assay (Bio-Rad). Microplate assay protocol was applied following the manufacturer’s manual. First, working reagent A’ was prepared by mixing 1 ml reagent A with 20 µl reagent S. Then, six different dilutions of BSA (0.2-1.5 mg/ml) for standard curve, and 1:5 or 1:10 dilutions of the samples were prepared. 5 µl standard/sample was pipetted into well and 25 µl of reagent A’ was added, subsequently. Finally, 200 µl of reagent B was added and the mixture was incubated for 15 min at RT. The plate was read in Synergy HT Multi-Mode Microplate Reader (BioTek, Winooski, USA) at 750 nm.

3.3.6.3 SDS-polyacrylamide gel electrophoresis

Protein separation according to molecular weight was performed via SDS-polyacrylamide gel electrophoresis system with denaturing conditions. The detergent SDS has a strong negative charge, hence it is able to denature the protein structure.

SDS treatment also provides continuous negative charge on proteins, thereby they can be separated according to their molecular weight. A discontinuous gel composed of upper stacking gel and lower separating gel was prepared using Mini-PROTEAN Vertical Electrophoresis system (Bio-Rad, Hercules, USA). Separating and stacking gels were prepared as described below and used after complete polymerization:

	Separating (10%)	Stacking (3%)
Separation buffer, 4x	5 ml	
Stacking buffer, 4x		2.5 ml
dH_2O	8.3 ml	5 ml
30% Acrylamide	6.7 ml	1 ml
20% APS	175 µl	80 µl
TEMED	5 µl	5 µl

40 µg protein samples were denatured before gel loading by mixing with 1x NuPAGE LDS Sample Buffer, 50 mM DTT and then boiling for 5 min at 95°C. 20 µl of denaturated samples together with SERVA Triple Color Proteinstandard III were loaded into the gel and the gel was run in the electrophoresis chamber filled by running buffer at 120 Volt for 2 hours.

3.3.6.4 Western blot

For detection, the proteins separated on the gel were transferred to a membrane via the western blot system. Here, a western blot sandwich was prepared in a classical way as the gel and nitrocellulose membrane were covered by filter papers and blotting pads. The sandwich was placed into Mini Trans-Blot® Module of Mini-PROTEAN Vertical Electrophoresis system (Bio-Rad, Hercules, USA) and the tank was filled with transfer buffer. An icepack was also placed into the tank and constant voltage of 70 Volt was applied for 2 hours. After transfer was completed, the membrane was washed with TBS-T and incubated in blocking buffer for 1 hour at RT with continuous shaking. After that, the membrane was incubated overnight with primary antibody in blocking buffer at 4°C with constant shaking. Next day, the membrane was washed three times with TBS-T for 10 min each and incubated with horse radish peroxidase

(HRP)-conjugated secondary antibody in blocking buffer for 1 hour at RT. The membrane was washed again three times with TBS-T for 10 min each and developed by adding Western Lightning Plus-ECL (chemiluminescence substrate and the oxidising reagent, PerkinElmer) for immunodetection. The membrane was visualized in ECL ChemoCam Imager (Intas, Göttingen, Germany). Relative protein amounts were calculated with densitometry analysis of membrane images via ImageJ software.

3.4 Molecular analysis

3.4.1 Genotyping of animals

3.4.1.1 DNA isolation and polymerase chain reaction

Genotyping of animals was performed by conventional polymerase chain reaction (PCR) followed by agarose gel electrophoresis. 2-3 mm long tail biopsies were taken from 4 week old mice and subjected to 600 μl 0.05 M NaOH buffer at 95°C for 10 min. After cooling on ice for 10 min, 50 μl 1 M Tris-HCl, pH 8, was added into each sample and then vortexed. Samples were kept at 4°C for short-term use and at -20°C for long-term storage. After basic DNA isolation, samples were analyzed to identify the status of the SV40 oncogene, Cre recombinase and *Hif1a* gene. During the genotyping procedure, sterile and PCR-clean materials were used.

For the SV40 PCR, 12.5 μl *Taq* PCR Master mix, 2x (Qiagen), 10.5 μl nuclease free water, 0.5 μl forward primer (0.2 μM), 2 μl reverse primer (0.2 μM), and 1 μl mouse DNA were added into the PCR tube.

For the Cre PCR, 12.5 μl *Taq* PCR Master mix, 2x (Qiagen), 7.5 μl nuclease free water, 0.5 μl forward primer (0.2 μM), 0.5 μl reverse primer (0.2 μM), and 4 μl mouse DNA were added into the PCR tube.

For the *Hif1a* PCR, 12.5 μl *Taq* PCR Master mix, 2x (Qiagen), 10.5 μl nuclease free water, 0.5 μl forward primer (0.2 μM), 0.5 μl reverse primer (0.2 μM), and 1 μl mouse DNA were added into the PCR tube.

As a negative control, nuclease free water was added instead of DNA in each PCR setup. The samples were incubated in thermal cycler with the program setups of specific PCR reactions as described below:

SV40 PCR program:

Denaturation	1 min 45 s	94°C	
	1 min	94°C	35x
Annealing	45 sec	60°C	
Elongation	50 sec	72°C	
	10 min	72°C	
Storage	∞	4°C	

Cre PCR program:

Denaturation	3 min	94°C	
	45 s	94°C	35x
Annealing	45 s	58°C	
Elongation	1 min	72°C	
	10 min	72°C	
Storage	∞	4°C	

Hif1a PCR program:

Denaturation	1min 45 s	94°C	
	25 s	94°C	35x
Annealing	45 s	57°C	
Elongation	1 min	72°C	
	10 min	72°C	
Storage	∞	4°C	

3.4.1.2 Agarose gel electrophoresis

PCR results were analyzed using agarose gel electrophoresis. 2% agarose gel was prepared by adding 2.5 g agarose in 150 ml 1x Tris acetate-EDTA (TAE) buffer and boiled in a microwave oven until agarose was completely dissolved. After cool down to ~60°C, 10 µl of DNA Stain Clear G (Serva) was added to the solution and mixed. Then, the solution was immediately transferred to a comb inserted gel tray and left to solidify. Combs were removed and the solidified gel was placed into gel chamber filled with 1x TAE buffer. 6 µl DNA ladder (100bp, Thermo Fisher Scientific) and PCR products mixed with 4 µl 6x Loading dye (Thermo Fisher Scientific) were loaded into the wells and the gel was run with a power of 5-6 Volt/cm for 40 min. Gels were visualized under an ultraviolet (UV) solo TS Imaging System (Analytik Jena, Jena, Germany). Agarose gel readouts were performed according to the presence of the bands for Cre and SV40 PCR results. For *Hif1a* PCR results, heterozygous floxed mice were detected with double bands, wherein the larger size of PCR product compared to WT was due to the insertion of loxP sites. Homozygous floxed mice were identified with a single band of larger PCR product.

3.4.2 Gene expression analysis

3.4.2.1 RNA isolation

Total RNA from eWAT was isolated using NucleoZOL reagent. Briefly, 100 mg frozen eWAT samples were pulverized using precooled metal mortar and pestle. For lysis, crushed tissue samples were mixed with 1 ml NucleoZOL reagent and samples were centrifuged for 10 min at 12,000 *g* at 4°C. The fat layer on top of the sample was discarded and the supernatant was transferred to a new tube. 400 µl RNase-free water was added into the samples and tubes were shaken vigorously for 15 s followed by 5 min incubation at RT. Then, samples were centrifuged for 10 min at 12,000 *g*, 4°C. The pellet contains DNA, protein and polysaccharides while RNA is solubilized in the supernatant. 1 ml of supernatant was transferred to a clean tube and mixed with 1ml of isopropanol for precipitation. The samples were incubated at RT for 10 min followed by centrifugation for 10 min, 12,000 *g* at 4°C. After this step, the RNA pellet was visible at the bottom of the tube. Next, the pellet was washed with 500 µl of 75% ethanol and centrifuged for 3 min at 8,000 *g* at 4°C, twice. Following the second washing step, supernatant was removed and RNA pellet was dissolved in 30 µl RNase-free water. RNA quantity was detected using Synergy HT Multi-Mode Microplate Reader (BioTek, Winooski, USA) at 260 nm and purity was checked by the 260/280 ratio.

3.4.2.2 complementary DNA (cDNA) synthesis

Before cDNA synthesis, RNA samples were treated with DNase in order to eliminate potential DNA contamination. First, 2,000 ng RNA sample was diluted to 8 µl volume with diethyl dicarbonate (DEPC)-treated water and then, 1 µl of 10x DNase I Buffer and 1 µl of 2U/µl DNase were added for 15 min incubation at 37°C. After that, 1 µl 25 mM EDTA was added to stop the enzyme reaction and the samples were incubated at 65°C for 10 min for enzyme inhibition. Samples were further diluted with 3 µl DEPC-treated water. For cDNA synthesis, each RNA sample was mixed with 0.25 µl of 100 µM random hexamer, 0.75 µl of 100 µM oligo deoxy-thymidine (dT)18, and 1 µl of 10 mM deoxynucleotide (dNTP) mix and incubated for 5 min at 65°C for denaturation. Afterwards, 4 µl of 5x RT buffer and 1 µl of 200 U/µl Maxima RT enzyme were added (total volume 20 µl) and the samples were incubated for annealing at 25°C for 10 min, for reverse transcription at 50°C for 15 min, and for enzyme inhibition at 85°C for 5 min.

3.4.2.3 Quantitative real-time polymerase chain reaction (qPCR)

Relative mRNA expression analyses in adipose tissue were performed via qPCR using the SYBR green-based method. PCR area and equipment were sterilized by UV radiation prior to preparation.

For each sample, 15 µg cDNA was mixed with 250/500 nM of target primer (listed in Section 2.8.2), 10 µl of 1x Power SYBR® Green PCR Master Mix and completed to 20 µl with nuclease free water. No template control sample using nuclease-free water was included and all samples were run in duplicates with optimal annealing temperature in 7500 Real-Time PCR System (Applied Biosystems, Thermo Fisher Scientific, Waltham, USA).

The following qPCR program was used with specific annealing temperatures as shown in Section 2.8.2 for each primer pair:

Holding stage	10 min	95°C

Cycling stage	15 s	95°C	40x
	60 s	annealing temperature	
Melt curve		60-95°C, 1°C rise per step	

Relative mRNA expressions were calculated using the comparative delta delta-CT method and normalized to *B2m* housekeeping gene. For that purpose, $-\Delta\Delta Ct$ was determined using the formula as below:

$-\Delta\Delta Ct = (Ct_{\text{target}, \textit{B2m}} - Ct_{\text{target, test gene}}) - (Ct_{\text{control}, \textit{B2m}} - Ct_{\text{control, test gene}})$. The relative gene of interest expression was determined by $2^{-\Delta\Delta Ct}$ calculation.

3.5 Histological analysis

3.5.1 Liver tumor area analysis

For liver tumor area analysis, tissues were first stained with hematoxylin and eosin (H&E). Livers were dissected from 16 week old ASV-B WT and ASV-B Hif1a^{MC} mice. 2-3 mm thick sections were cut from the left lobe of the liver and were fixed in 4% formaldehyde overnight at 4°C. Next day, tissues were washed with 1x PBS twice on a shaker and transferred to 70% Ethanol. Tissues were dehydrated by an overnight procedure and the next day embedded into paraffin at the IZKF immunohistochemistry facility (University Hospital RWTH Aachen). For histological evaluation, tissues were cut as 2-3 µm thick sections using a sledge microtome. The sections were deparaffinized in xylene three times for 10, 5, and 5 min. Subsequently, sections were re-hydrated in decreasing ethanol concentrations (100%, 100%, 96%, 70% ethanol in distilled water) for 5 min each, followed by rinsing in ultra-pure water. Then, for nuclei visualization, slides were stained with hematoxylin solution for 5 min, rinsed with warm tap water once and washed with fresh warm tap water for 10 min. For staining of the cytoplasm, sections were incubated with 1% eosin for 3 min and subsequently washed in 0.8% acetic acid solution until a pink color appeared. The final wash was performed in distilled water and then, the slides were dehydrated again using increasing ethanol concentrations (70%, 96%, 96%, 100% ethanol in distilled water) for 3 min each, followed by xylene. Finally, the sections were coverslipped after adding Vitro-Clud embedding medium.

H&E stained sections of ASV-B livers were used for analyses of tumor areas by medical student Johanna Wulfmeier as a part of her thesis. Two tissue sections per mouse were used for evaluation. Microscopic images were scanned using a Hamamatsu NanoZoomer 2.HT Tissue Slide Scanner (Hamamatsu, Herrsching, Germany) at x100 magnification in the Institute of Pathology, University Hospital RWTH Aachen. Tumor areas were quantified by ImageJ (Figure 3.5).

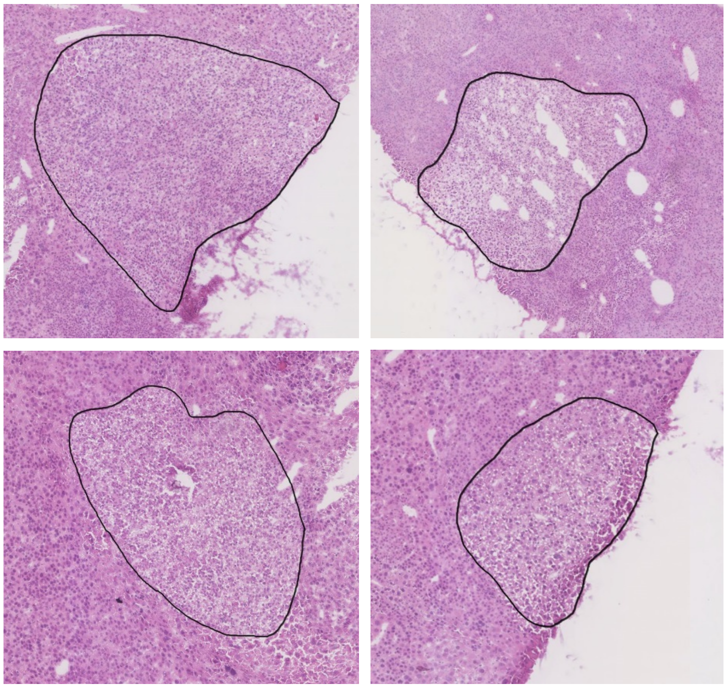

Figure 3.5: Representative images of H&E stained sections of ASV-B livers used for tumor area analysis. H&E stained liver sections of 16 week old ASV-B mice were analyzed for tumor area quantification using the ImageJ freeware.

3.5.2 Adipocyte cell size analysis

3.5.2.1 Hematoxylin and eosin (H&E) staining of eWAT

Dissected eWAT from gonadal pads of 16 week old mice were fixed in 4% formaldehyde overnight at 4°C. Following dehydration, H&E staining was performed as described in Section 3.5.1 for liver tissues.

3.5.2.2 Calculation of cell size of adipocytes

Pictures of representative areas from H&E stained eWAT sections were taken at 200x magnification and Fiji software with the Adiposoft macro was used to calculate cell size of a total of 35 images per group. The Adiposoft macro performs ‘pre-processing’, ‘simple segmentation’, and ‘grayscale watershed segmentation’ of each image and gives the cell count automatically together with the calculated area for each count. Minimal 20 µm and maximum 100 µm thresholds were set for adipocyte diameter and the program was run for automated measurement of adipocyte diameter followed by a manual correction of cell borders when required. Representative images show an example for labeling of cells by the software. After measurements of all pictures were completed in Adiposoft, a frequency distribution of cells was calculated for each group. Total adipocyte number within the distribution was subsequently calculated and the frequency was converted to a percentage of total adipocytes counted. These calculations were performed using Microsoft Excel (Microsoft, Washington, USA).

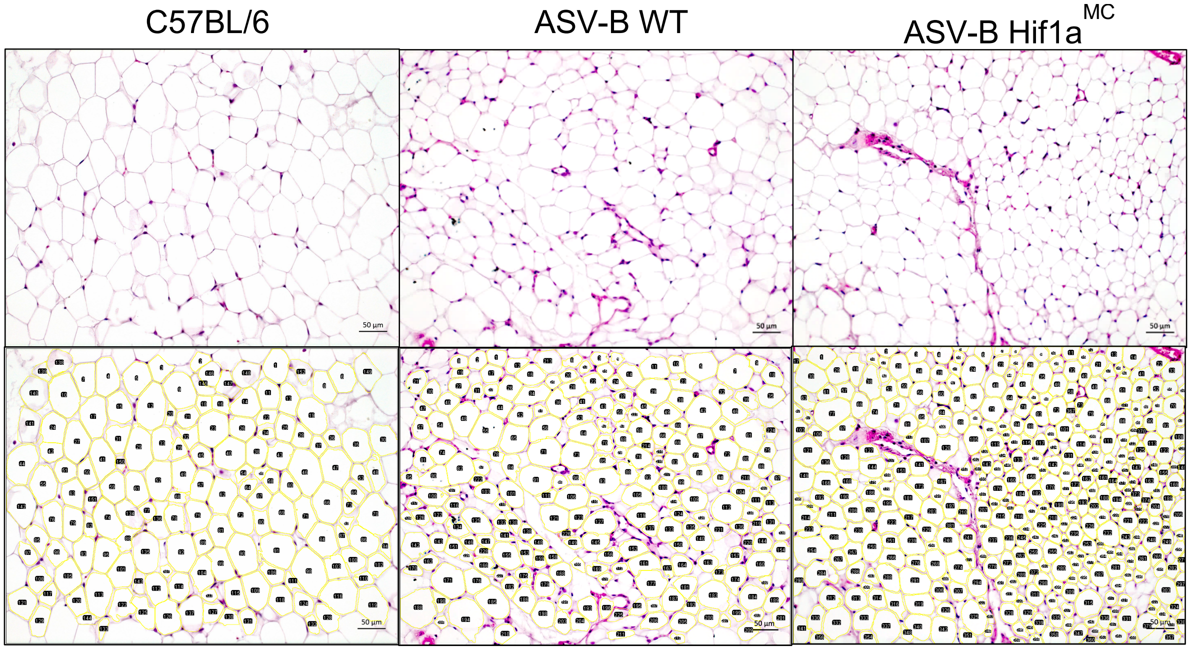

Figure 3.6: Representative images of adipocyte cell size analysis. H&E stained eWAT sections (upper panels) and analysis of pictures by Adiposoft software (lower panels) were shown. The cells were marked and numbered automatically by the software and manually corrected if required. Then calculated areas were given by the software and saved for overall analysis.

3.5.3 Multiplex immunofluorescence staining

The multiplex approach of immunohistochemistry-based staining methods provides a simultaneous visualization of multiple targets in a tissue sample. This approach utilizes the organic compound tyramide, which is activated by a catalyst (for instance HRP) and covalently binds to tyrosine residues on the surface or in the vicinity of protein antigens. Therefore, after activated by HRP catalysis, tyramide-fluorophore molecules can bind to the tissue at the site of antigen binding and gives not only antigen-specific but also amplified fluorescence signals. Furthermore, the heat resistant nature of tyramide-tyrosine binding provides stable fluorescence signal at a specific site during the heat-induced stripping of primary and secondary antibody (Figure 3.7). The removal of antibodies when protecting the signal allows the use of multiple antibody staining on the same tissue without any cross-binding.

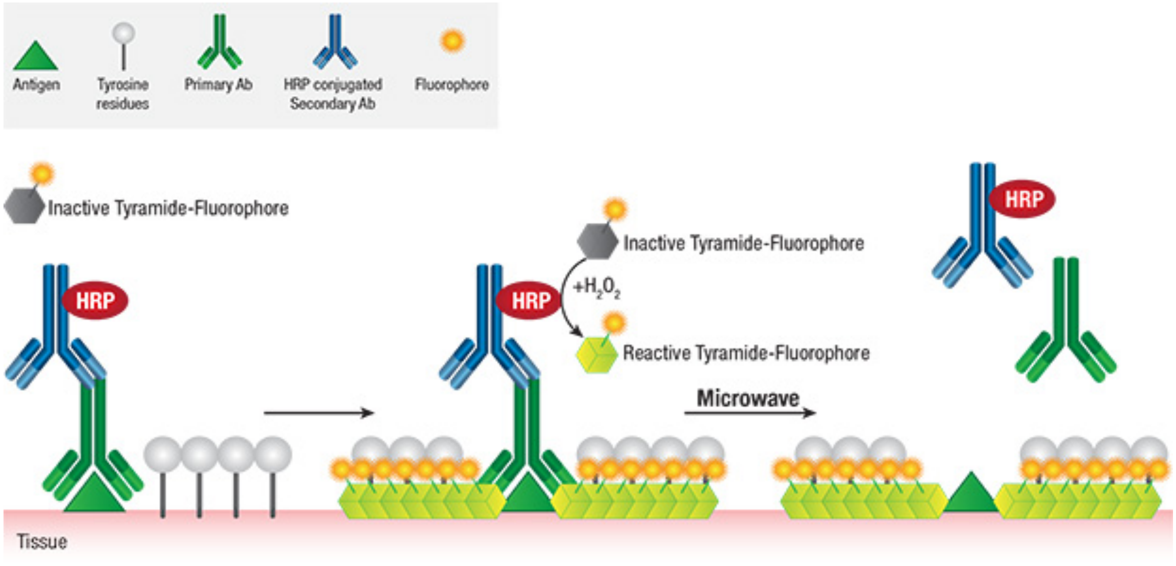

Figure 3.7: The description of immunofluorescence staining using tyramide-fluorophore for multiplex approach. (https://www.cellsignal.com/contents/resources-applications/fluorescent-multiplex-immunohistochemistry/fluoresence-mihc).

eWAT samples were stained using multiplex immunofluorescence staining. Paraffin embedding of formalin fixed eWAT was performed as described in Section 3.5.1. 2 µm paraffin sections from eWAT were deparaffinized in xylene three times for 10, 5, and 5 min. Subsequently, sections were re-hydrated in decreasing ethanol concentrations (100% / 100% / 96% / 70% ethanol/distilled water) for 5 min each followed by rinsing in ultra-pure water for 3 min. Then, the sections were fixed for 10 min in 3.5% formalin, washed in ultra-pure water for 2 min and washed in TBS-T (Dako) for 2 min. Antigen retrieval was done by 15 min of cooking at 110°C in Dako target retrieval solution in a Decloaking Chamber (Biocare Medical, USA). After the solution cooled down in icy-water, sections were washed first in ultra-pure water and then in TBS-T (Dako) for 2 min. Next, 100 µl Dako antibody diluent was dropped on each section for blocking of 10 min incubation at RT. Primary antibodies diluted in Dako antibody diluent and 100 µl solution was added on top of the sections for 30 min at RT followed by three washes for 2 min each with ultra-pure water. Afterwards, 100 µl corresponding secondary antibody (ImmPress anti-rabbit/rat IgG, Vector Lab) was added onto the sections and incubated at RT for 20 min. The sections washed again three times of 2 min with ultra-pure water. For permanent labeling of detection sites with a fluorescent tag, sections were treated with Opal 570 Reagent (PerkinElmer, 1:100 in amplification diluent) for 10 min at dark in RT. Subsequently, the antibodies were detached from sections by microwave cooking in AR6 buffer (PerkinElmer), where Opal fluorophore remained coupled. Then, sections were washed first in ultra-pure water and then in TBS-T (Dako) for 2 min. For the staining of second antigen, sections were directly blocked again and antibody staining procedure was repeated. Following secondary antibody treatment, antigens were labeled with another fluorescent tag, Opal 520 Reagent (PerkinElmer, 1:100 in amplification reagent) and subjected to microwave cooking. After washing, nuclei were stained with 50 µl spectral DAPI (PerkinElmer) solution (2 drops DAPI in 1 ml TBS-T) for 5 min followed by three times 2 min washing of TBS-T (Dako). Tissue sections were covered with VECTASHIELD HardSet mounting medium (Vector Lab). Fluorescent signals were detected, separated and recorded using the Vectra 3.0 automated quantitative imaging system (PerkinElmer, Waltham, USA). Quantification of signals was performed via the inForm image analysis software (PerkinElmer).

3.5.4 Neuron-macrophage distance calculation

Neuron-macrophage distance calculation was performed by our collaborator Univ.-Prof. Dr. Dr. Twan Lammers’s group at the Institute for Experimental Molecular Imaging, University Hospital RWTH Aachen. eWAT samples were stained with macrophage- (EGF-like module-containing mucin-like hormone receptor-like 1, F4/80) and sympathetic neuron- (tyrosine hydroxylase, TH) specific markers as described in Section 3.5.3. For the automated histological distribution evaluation of macrophages and neurons, the Definiens Developer XD 2.0.4 image analyzer was used. Macrophages were quantified using an algorithm in which neurons were segmented via thresholding followed by calculation of a distance map for each segmented object. A concentric ring of 100 µm was drawn around each respective neuron. The number of macrophages was determined within each of these rings and ratio of macrophages to neurons was calculated.

3.6 Cell Culture

3.6.1 L929-conditioned medium production

L929 mouse fibroblasts were cultured in RPMI 10% (RPMI supplemented with 10% FBS, 1%Glutamax, 100 U/ml penicillin, 100 µg/ml streptomycin) media. Cells were detached using Trypsin EDTA and seeded in T175 flasks containing 100 ml RPMI 10%. The cells were checked daily and when they became confluent, it was defined as Day 0. Cells were incubated for additional 10 days in 37°C in a cell culture incubator. After 10 days, cell media were sterilized by filtration using 20 µm filter and aliquots were stored at -80°C.

3.6.2 Isolation and stimulation of BMDM cells

Tibia, femur, and humerus were dissected from 8-11 weeks old female ASV-B WT and Hif1a^{MC} mice. Bones were sterilized in 70% ethanol for 5 min and washed with RPMI medium. After washing, 10 ml RPMI was added and bone marrow was collected after breaking the bones. Bone marrow suspension were transferred into 100 µm Cell Strainer and cells were centrifuged at 250 *g* for 10 min at 4°C. 5 ml of Ammonium-Chloride-Potassium lysing buffer was added on cell pellet and resuspended for 30 s. After adding 5 ml of 1x PBS, the suspension was centrifuged at 250 *g* for 10 min at 4°C. Afterwards, the cell pellet was dissolved in 10 ml of RPMI 10% and cells were counted with a hemocytometer. 1x10^{7} cells were seeded in plastic petri dishes (92x16mm). After overnight incubation, non-attached cells were collected and counted. 5x10^{6} cells were seeded in plastic petri dishes in growth medium (RPMI supplemented with 20% FBS and 30% L929-conditioned medium, 1%Glutamax, 100 U/ml penicillin, 100 µg/ml streptomycin) and incubated for a week to differentiate. Three days after seeding, 10 ml growth medium were added to the cells. At day seven, differentiated BMDMs were scraped in 1x PBS, 2 mM EDTA followed by 10 min, 250 *g*, 4°C centrifugation. The cell pellet was dissolved in replating medium (RPMI supplemented with 10% FBS and 15% L929-conditioned medium, 1%Glutamax, 100 U/ml penicillin, 100 µg/ml streptomycin). 2x10^{6} cells were seeded in 1 ml total volume into a well of 6-well plate and incubated for 6 hours. Next, the medium was changed to RPMI 10% and incubated for overnight. On the following day, BMDM cells were stimulated for classical activation by changing medium to RPMI 10% containing 100 ng/ml LPS (Sigma Aldrich) and 20 ng/ml Ifn-γ (eBioscience). Cells were stimulated for alternative activation by adding RPMI 10% containing 20 ng/ml Il-4 (eBioscience) and unstimulated cells were seeded in RPMI 10% as control. After 48 hours of stimulation, medium was collected and centrifuged at 400 *g* for 5 min at 4°C and stored at -80°C until use for catecholamine measurement.

3.7 Body composition analysis of HCC patients

63 HCC patients from the Department of General, Transplantation, and Visceral Surgery at the University Hospital RWTH Aachen were subjected to body composition analysis following the approval of the ethics committee of the University Hospital RWTH Aachen. Patients' age ranged from 21 to 86 years (mean 68), 45% were female and 55% male, BMI ranged from 17.7 to 36.3 kg/m^2 (mean 26), T stage was 34% T1, 30% T2, 26% T3 and 10% T4. CT scans of patients were performed during routine clinical work maximally 6 weeks before surgery. Abdominal scans were analyzed in a blinded approach in an anonymized format. At first, for each patient a single CT slice at the level of the third lumbar vertebra (L3) was selected and used as a standard landmark to measure the tissue cross-sectional area in cm^2 as previously reported [128]. CT scans with low quality image or missing parts of muscle tissue on the ventral, dorsal, or both lateral edges of the scan were excluded. After L3 selection, 47 patients became eligible for body composition analysis. L3 cross-sectional images were analyzed using the sliceOmatic software (version 5.0, TomoVision, Montreal, Canada) to determine skeletal muscle and adipose tissue area. Muscle areas included in the analysis were internal and external obliques, transversus abdominus, rectus abdominus, psoas, quadratus lumborum, and erector spinae muscles. Tissue Hounsfield unit (HU) thresholds were set up as recommended by the software, -29 to 150 HU for skeletal muscle, -150 to -50 for visceral adipose tissue (VAT), and -190 to -30 for subcutaneous adipose tissue (SAT). Cross-sectional areas (cm^2) were

determined by assigning a specific tag on different tissues. Total area of skeletal muscle, VAT, and SAT were normalized for stature of the patients to calculate the L3-muscle index, L3-VAT index, and L3-SAT index in cm^2/m^2 which provides a powerful estimation of total body skeletal muscle, VAT, and SAT mass [128]. Representative cross-sectional L3 images used in the analysis are shown in Figure 3.8.

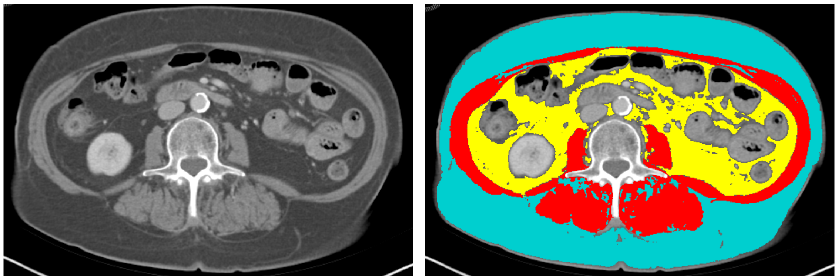

Figure 3.8: Representative L3 CT image of a patient (left) and colored version of the same image using sliceOmatic software (right). Red color shows muscle, yellow region represents VAT, and cyan shows SAT.

This cohort was considered to be too small for a cut-point analysis by optimal stratification, therefore, determined cut-off values based on tertiles were stratified by sex. For each index, sex-specific cut-off values were established by dividing the cohort into tertiles. Determining the cut-off at a tertile enables the comparison between groups with a relatively low/high value to be compared with the rest of the group, while not forcing subjects with a value around the cut-off in a low or high category. By the use of the lowest tertile as the reference group in comparison to the middle and high tertiles, statistical analyses were performed.

3.8 Statistical Analysis

For animal data, all statistical analyses were carried out using GraphPad Prism 6.0 software. Patient data were analyzed with SPSS v25 (IBM, New York, USA) software. All data were presented with mean and standard error of the mean (S.E.M.). Animal data were analyzed using two-way analysis of variance (ANOVA), one-way ANOVA followed by Tukey’s post-hoc tests or unpaired Student’s t-test according to experimental groups. Patient data were analyzed using Kaplan-Meier method and differences between body composition values and short-term, and 2-year survival were calculated using log-rank test. $P < 0.05$ was considered as statistically significant and the asterisks in the graphs indicate statistically significant changes with P values: * $P < 0.05$, ** $P < 0.01$ and *** $P < 0.001$. Each analysis was specified in the figure legends of the graphs together with sample size of the groups.

4. Results

4.1 ASV-B mice show cachexia during cancer development

The transgenic ASV-B model was used to investigate cancer cachexia in murine HCC. Many different mouse models have been used for cachexia studies for various cancer types. Mouse models of pancreatic cancer, lung cancer, colon cancer have been characterized for cachexia and utilized for cancer cachexia research for a better understanding of the molecular mechanisms and to develop new treatment approaches [80, 129]. Nevertheless, no transgenic liver cancer mouse model has been characterized and used for cachexia research until today.

4.1.1 Body weight and food intake was not affected in ASV-B mice

As explained in detail in Section 3.1.1, the ASV-B mouse is an established transgenic model that develops hepatocellular carcinoma. This mouse model is characterized at different time points in disease progression, as the liver develops neoplasia, adenoma and carcinoma at 8, 12 and 16 weeks of age, respectively.

As the initial step to characterize cachexia in ASV-B mice, body weight and food intake were monitored over the course of cancer development between 12 and 18 weeks of age (follow-up study). Age-matched healthy C57BL/6 mice were used as controls. During this period, ASV-B and C57BL/6 mice gained 2 g of body weight (Fig. 4.1A). Food intake of ASV-B and C57BL/6 mice were also comparable (Fig. 4.1B). In addition to the follow-up study, ASV-B mice were sacrificed at 12, 16, and 18 weeks of age in order to measure tissue weights. C57BL/6 mice were sacrificed when they were 16 weeks old, and their tissue weights were used as reference values. ASV-B mice showed significantly increased liver weights throughout the period of cancer development compared to tumor-free controls (5-fold increase at 18 weeks) (Fig. 4.1C), demonstrating that tumor burden contributes significantly to the total weight of ASV-B mice. Enlarged livers with tumor nodules and morphological differences of the abdomen of C57BL/6 and ASV-B mice can be seen in Fig. 4.1D at the age of 16 weeks.

These results illustrate the liver tumor progression of ASV-B mice. One the one hand, similar body weight increase and food intake were observed; on the other hand, noticeably different liver mass developed between ASV-B and healthy mice. Altogether, these results suggest tissue wasting in ASV-B mice during HCC progression.

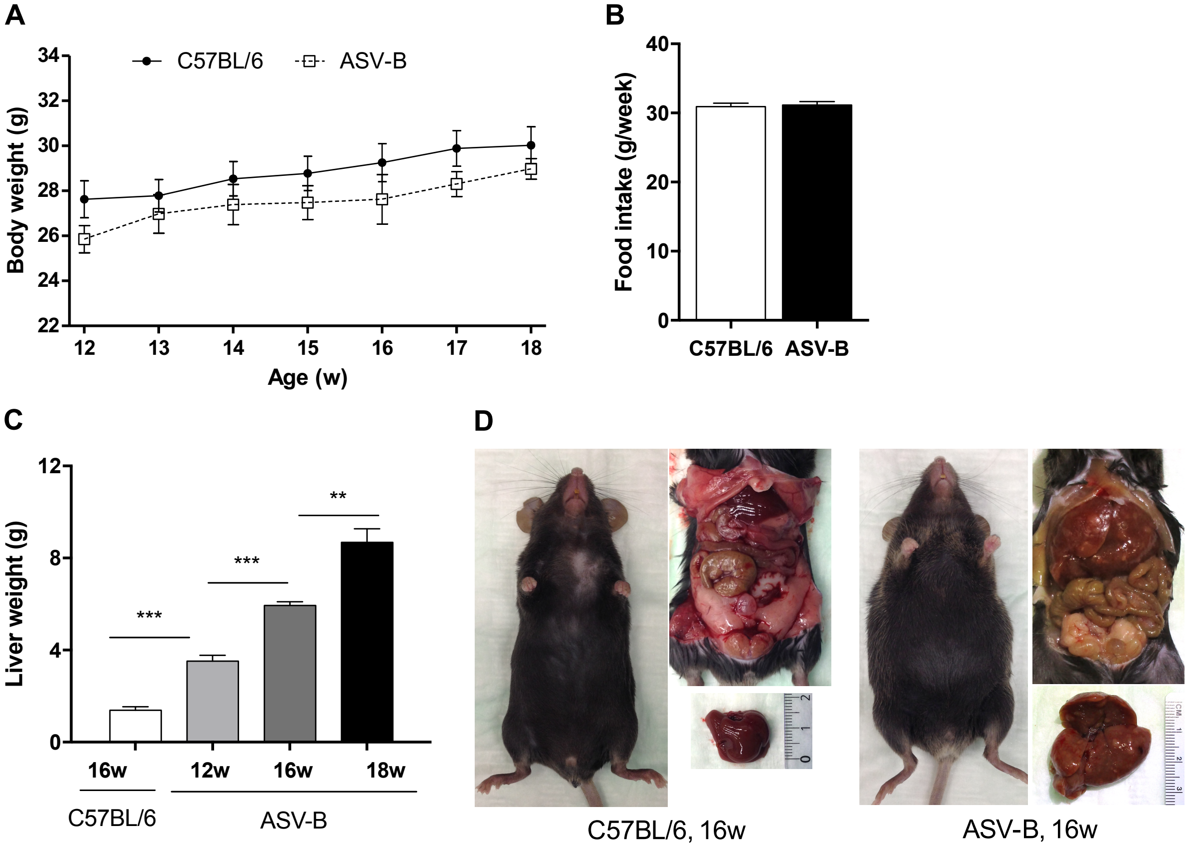

Figure 4.1: Body weight and food intake follow-up of ASV-B mice. A. Body weight of control C57BL/6 (n = 8) and ASV-B (n = 8) mice were measured as a follow-up study between 12 and 18 weeks of age. **B.** Food intake measurements were performed weekly from 12 to 18 weeks of age of C57BL/6 (n = 3) and ASV-B (n = 8) mice and represented as average weekly consumed food. **C.** Liver weight of sacrificed mice at different time points; C57BL/6 16 weeks old mice (16w, n = 8) and ASV-B 12 (12w, n = 8), 16 (16w, n = 8), and 18 weeks old (18w, n = 8) mice. **D.** The representative images of 16 weeks old healthy control C57BL/6 and ASV-B mice with visible tumor nodules in liver. Data show means with S.E.M. and were analyzed by two-way ANOVA (**A**), unpaired Student's *t*-test (**B**), one-way ANOVA followed by Tukey post hoc test (**C**); $^{**}P < 0.01$; $^{***}P < 0.001$.

4.1.2 Muscle and fat loss occurs in ASV-B mice

To evaluate wasting in muscle and fat tissues, different parts of skeletal muscles, heart, and gonadal fat tissue were excised and measured. ASV-B mice showed significantly reduced skeletal muscle mass until 16 weeks of age in gastrocnemius (GC), tibialis anterior (TA) and extensor digitorum longus (EDL) muscle compared to control mice (Fig. 4.2A). Heart mass was reduced in ASV-B mice in comparison to healthy mice; however, it was not affected in ASV-B mice at different time points.

For the analysis of fat tissue, gonadal fat tissue (also known as epididymal white adipose tissue (eWAT)) was measured. Compared to healthy mice, ASV-B mice showed significant fat loss already at 12 weeks of age and progressing throughout further cancer development (Fig. 4.2B). In addition, µCT analyses were performed to quantify and localize the fat tissue. As can be seen in the images, all fat depots were remarkably smaller in ASV-B mice compared to controls (Fig. 4.2C). Image quantification revealed that the total fat volume in ASV-B mice was 3.5-fold lower compared to control mice (Fig. 4.2D). Besides fat volume, liver volume was calculated using µCT images. In line with the liver mass results, liver volume of ASV-B mice was significantly higher than in controls (Fig 4.2E).

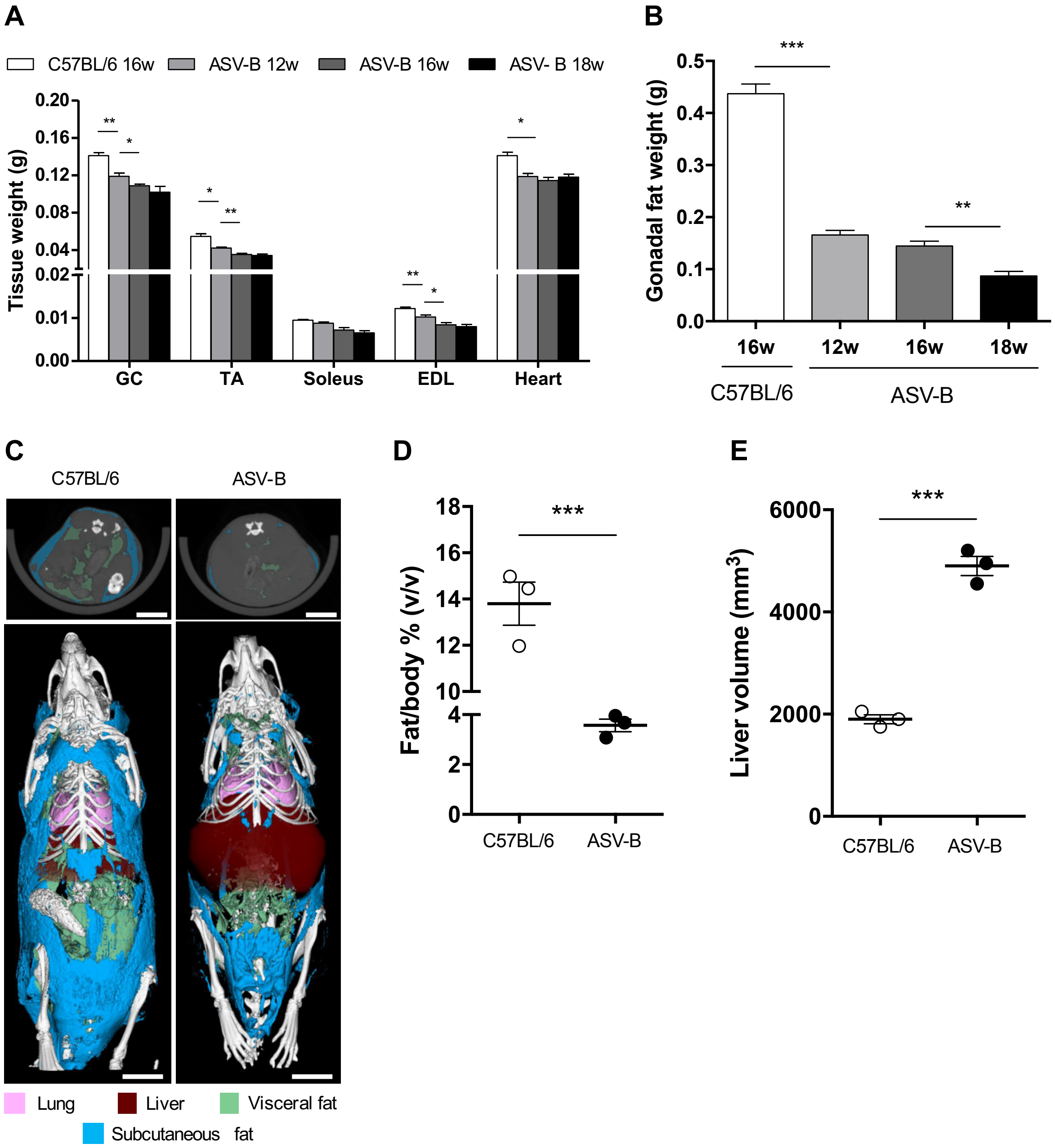

Figure 4.2: ASV-B mice showed muscle and fat loss. A. Different muscle parts (GC: Gastrocnemius, TA: Tibialis anterior, soleus and EDL: Extensor digitorum longus) were dissected and weighed for C57BL/6 mice (*n* = 3, 16 week old) and ASV-B mice at indicated time points (*n* = 8, 5, 4 in 12, 16, 18 week old, respectively). **B.** Gonadal fat was removed and measured (*n* = 8 per group) at the same time points as muscle tissues. **C.** µCT imaging at 14-week-old C57BL/6 and ASV-B mice, upper part shows representative 2D cross-sectional µCT images in transversal planes of the abdomen of one representative mouse from each group (subcutaneous and visceral fat tissue is indicated in blue and green color). Lower part shows representative images of three-dimensional volume renderings of segmented bones (white), lungs (pink), liver (brown) and fat (blue/green), scale bar 1 cm. **D.** Quantification of µCT imaging for fat volume (*n* = 3 per group). **E.** Quantification of µCT imaging for liver volume (*n* = 3 per group). Data represent means with S.E.M.

and analyzed by one-way ANOVA followed by Tukey post hoc test (**A**, **B**), unpaired Student's *t*-test (**D**, **E**); **P* < 0.05; ***P* < 0.01; *** *P* < 0.001.

During HCC development, total body weight in ASV-B mice was increased, evidently due to the increased tumor mass. However, in this model, skeletal and heart muscle amounts were significantly reduced, and notable fat loss was observed. Together, these results point out that cancer-induced cachexia occurs in ASV-B mice.

4.1.3 Complete blood count suggests anemia in ASV-B mice

Complete blood count analyses were performed to evaluate the effect of tumor formation on blood (Figure 4.3). No significant differences in white blood cell number between C57BL/6 mice and ASV-B tumor mice at the age of 16 weeks was found. Total red blood cell number was lower in tumor mice compared to healthy mice. In addition, two erythrocyte parameters, hemoglobin (HGB) and hematocrit (HCT, volume ratio of red blood cells) were significantly reduced in ASV-B mice. Likewise, the average volume of the red blood cells (mean corpuscular volume, MCV) and the amount of hemoglobin per red blood cell (mean corpuscular hemoglobin, MCH) were also decreased in ASV-B mice. Altogether, the decrease in all red blood cell parameters demonstrates anemia in ASV-B mice. In addition, tumor mice had increased platelet numbers (thrombocytosis) compared to healthy mice. In the clinic, thrombocytosis had been observed in HCC patients and was associated with bigger tumor volume and decreased survival [130].

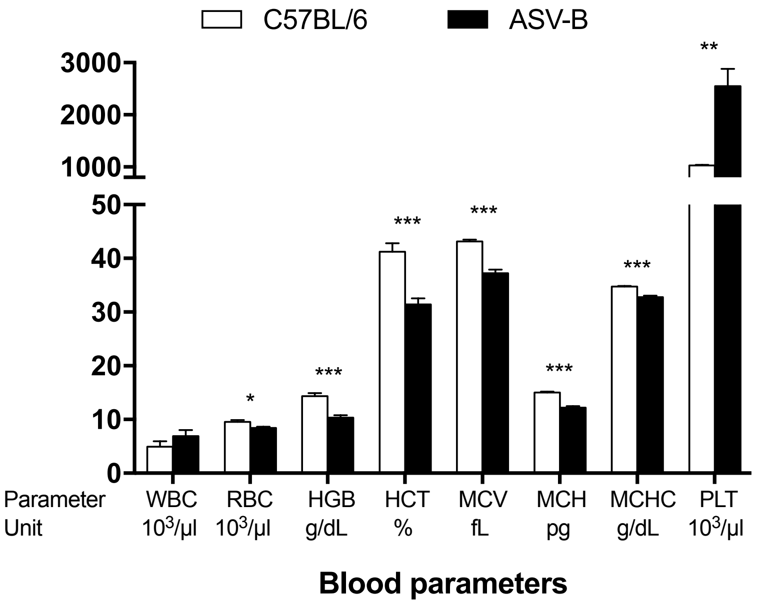

Figure 4.3: Blood values of ASV-B mice. Complete blood counts in C57BL/6 (*n* = 5) and ASV-B (*n* = 6) mice at 16 weeks of age. WBC: White blood cells, RBC: Red blood cells, HGB: Hemoglobin, HCT: Hematocrit, MCV: Mean corpuscular volume, MCH: Mean corpuscular hemoglobin, MCHC: Mean corpuscular hemoglobin concentration, PLT: Platelets. Data represent means with S.E.M. and analyzed by unpaired Student's *t*-test; $^{*}P < 0.05$; $^{**}P < 0.01$; $^{***}P < 0.001$.

4.2 Conditional knockouts of *Hif1a* in ASV-B mice reveals diverse outcomes regarding cachexia

As explained in section 1.2.3.3, inflammation is widely appreciated as a causal factor in cachexia. In earlier studies, inflammation and cachexia have been shown to be associated in animal tumor models as well as cancer patients [47]. Given the well-established importance of inflammation in cachexia and the role of HIF-1α in inflammation and tumor cells (Section 1.4), the significance of HIF-1α was investigated in ASV-B mice via knockout of *Hif1a* in tumor or myeloid cells by the Cre-loxP system.

4.2.1 ASV-B mice with hepatocyte-specific *Hif1a* knockout

A liver-specific knockout of *Hif1a* was achieved by using the Cre-loxP system together with hepatocyte-specific Albumin promotor (as explained in section 3.1.2). First, ASV-B mice were crossed with C57BL/6 mice harboring a hepatocyte-specific *Hif1a* knockout. Offspring mice were termed “ASV-B Hif1a^{HC}”. Following the establishment of the mouse lines, cachexia in ASV-B Hif1a^{HC} mice was analyzed. First, body weight follow-up of ASV-B wild-type (WT) and ASV-B Hif1a^{HC} mice was performed between 12 and 18 weeks of age (Fig. 4.4A). ASV-B WT littermates were heavier than ASV-B Hif1a^{HC} mice and both groups continued to gain weight until 14 weeks of age. ASV-B Hif1a^{HC} mice showed a subtle body weight decrease after 15 weeks, without reaching statistical significance. Next, tissue weights were compared between ASV-B WT and ASV-B Hif1a^{HC} mice. Liver (Fig. 4.4B) as well as skeletal muscle (GC, TA, soleus, EDL) (Fig. 4.4C) weights were not different between 18 week old ASV-B WT and ASV-B Hif1a^{HC} mice. Similarly, white adipose tissue (WAT), brown adipose tissue and heart masses were comparable (Fig. 4.4C).

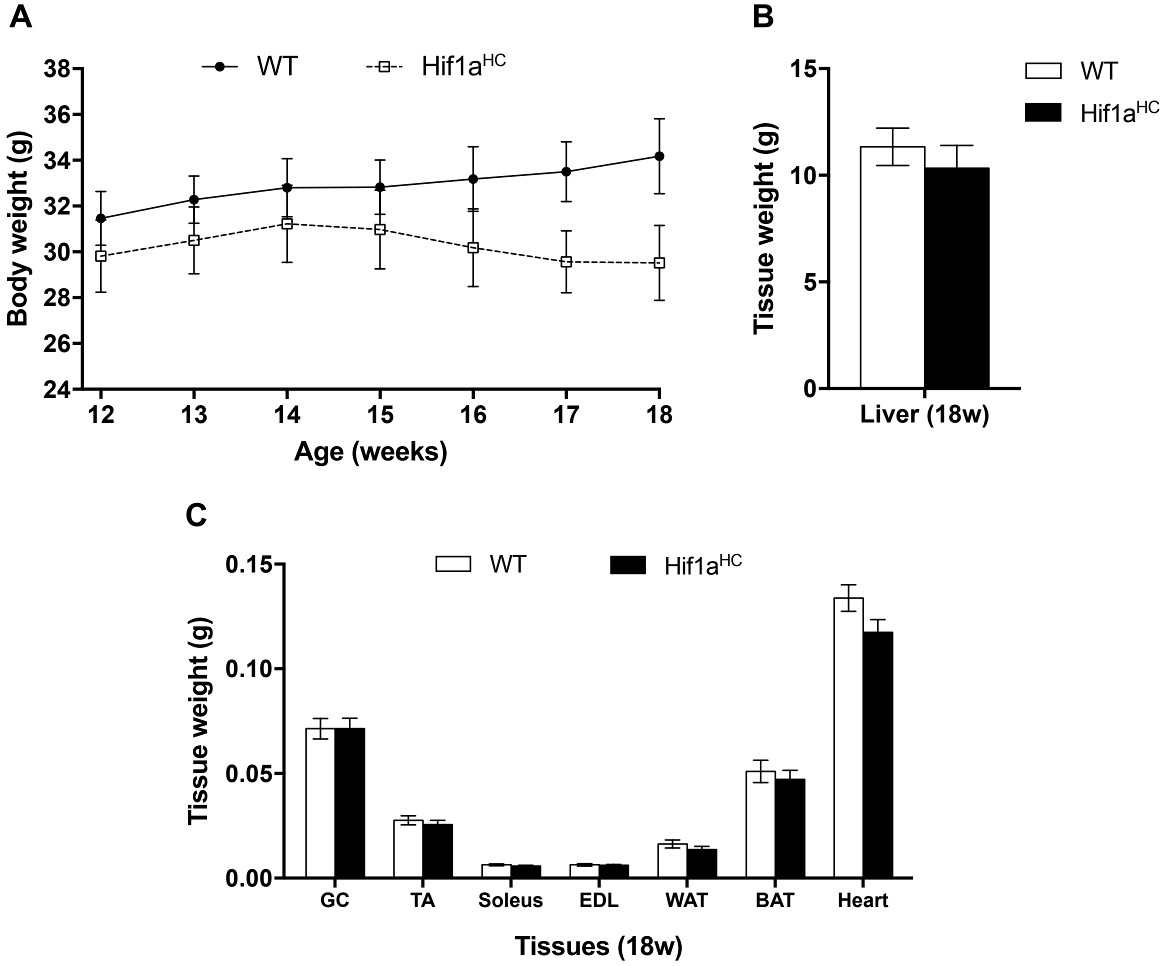

Figure 4.4: Body and tissue weight did not differ between ASV-B WT and Hif1a^{HC} mice. ASV-B WT (*n* = 5) and Hif1a^{HC} (*n* = 5) mice were used for **A.** Body weight follow-up measurement from

12 to 18 weeks of age, **B.** Liver weight at 18 weeks, **C.** Skeletal muscle (GC, TA, EDL, soleus), heart and fat tissue (epididymal WAT, BAT) weights at 18 weeks of age. Data show means with S.E.M. and were analyzed by two-way ANOVA (**A**), unpaired Student's *t*-test (**B**, **C**).

In addition to total body and tissue weights, body composition is another parameter utilized in the assessment of cachexia. Thus, body composition of mice was measured via NMR spectroscopy weekly between the age of 12 and 18 weeks. Total lean and fat amounts were calculated to total body weight and demonstrated as percentage. Lean mass was determined to increase through the cancer development, and no significant difference was observed between ASV-B WT and ASV-B Hif1a^{HC} mice (Fig. 4.5A). Total fat percentage at 12 weeks old age was 7.2% and 8% in ASV-B WT and ASV-B Hif1a^{HC} mice, respectively, and they maintained fat loss until 16 weeks old age.

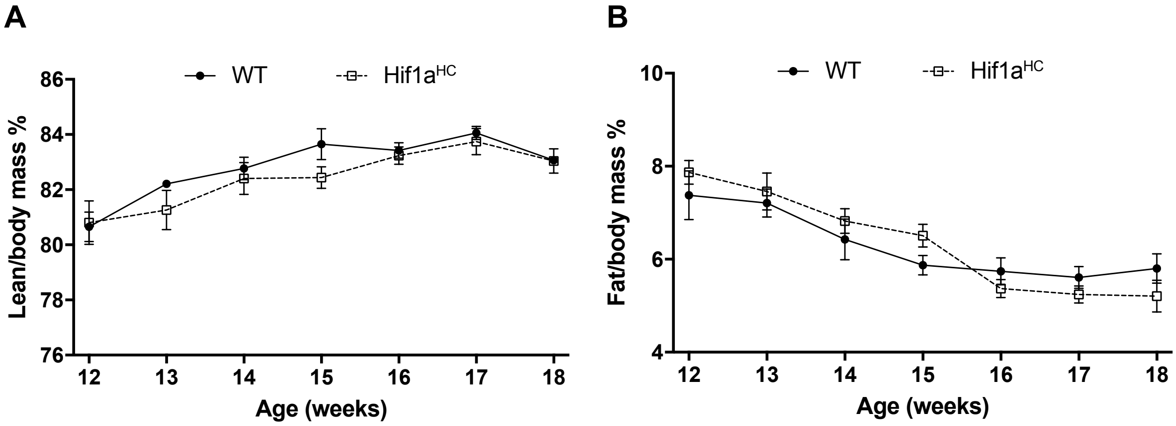

Figure 4.5: Body composition analyses of ASV-B WT (n = 5) and Hif1a^{HC} (n = 5). A. Lean and **B.** Fat mass amounts were calculated from NMR measurements and presented as percentage of total body mass. Data represent means with S.E.M. and analyzed by two-way ANOVA.

Although total lean mass increase was observed in NMR results, it was shown that ASV-B mice loose skeletal muscle during HCC progression, suggesting muscle wasting. To evaluate the wasting at the biochemical level, the ubiquitin–proteasome system (UPS) and apoptotic activities were tested in GC muscle. UPS activity were provided by measurements of enzyme kinetic assessments of trypsin-like, chymotrypsin-like and peptidylglutamyl-peptide hydrolysing (PGPH) activities in GC muscle extracts of C57BL/6, ASV-B WT and ASV-B Hif1a^{HC} mice. Trypsin-like and PGPH activities of the proteasome were increased in ASV-B WT and ASV-B Hif1a^{HC}

mice compared to C57BL/6 mice, however these activities did not change between ASV-B WT and ASV-B Hif1a^{HC} mice (Fig 4.6A). Caspase-3 and -6 activities were higher in ASV-B mice than C57BL/6 mice, but they were similar in ASV-B WT and ASV-B Hif1a^{HC} (Fig 4.6B). These results suggest protein breakdown in skeletal muscle tissue of ASV-B mice, however, no effect of the HIF-1α knockout in tumor cells was observed.

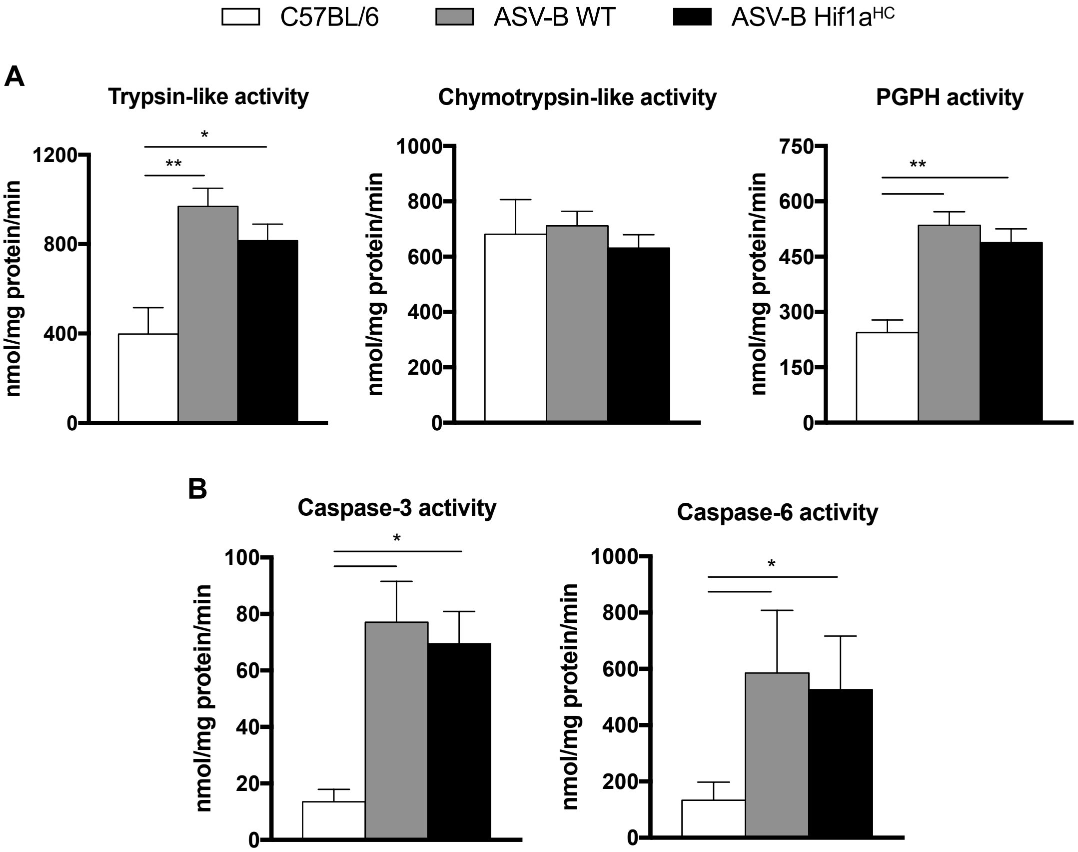

Figure 4.6: Proteolytic and apoptotic activities were increased in GC muscle of ASV-B WT and ASV-B Hif1a^{HC} mice. Control C57BL/6 (*n* = 3) mice were used as well as ASV-B WT (*n* = 7) and ASV-B Hif1a^{HC} (*n* = 7) mice. **A.** Proteasome activity was analyzed by measuring trypsin-like activity, chymotrypsin-like activity and PGPH activity. **B.** Apoptotic activity was checked by caspase-3 and caspase-6 activity. Data show means with S.E.M. and were analyzed by one-way ANOVA followed by Tukey post hoc test.

Collectively, body weight and composition measurements together with tissue analysis failed to indicate a significant effect of Hif-1α deletion in tumor cells for HCC-induced cachexia.

4.2.2 ASV-B mice with myeloid-specific *Hif1a* knockout

Hif1a in myeloid cells is important for the inflammatory function as explained in Section 1.4. More specifically, macrophages are thought to be involved in the inflammatory response in cancer cachexia [47]. Against this background, I sought to investigate the functional importance of macrophages for HCC-induced cachexia.

The myeloid cell-specific knockout of *Hif1a* was obtained by the Cre-loxP system in combination with the myeloid cell-specific lysozyme M promotor (as explained in Section 3.1.2). ASV-B mice were crossed with myeloid cell-specific *Hif1a* knockout mice, and offsprings were termed "ASV-B Hif1a^{MC}". Following the establishment of the mouse line, the effect of conditional knockout of *Hif1a* for ASV-B cachexia was investigated. First, body weight follow-up of ASV-B WT and ASV-B Hif1a^{MC} mice was measured between age of 12 and 18 weeks (Fig. 4.7A). Each group increased their total body weight by 2 to 3 g, and a statistically significant difference between the genotypes was not observed. When tissue weights were evaluated between ASV-B WT and ASV-B Hif1a^{MC} mice, liver weight (Fig. 4.7B) together with skeletal muscle (GC, TA, soleus, EDL), adipose tissue (WAT, BAT), and heart were similar (Fig. 4.7C).

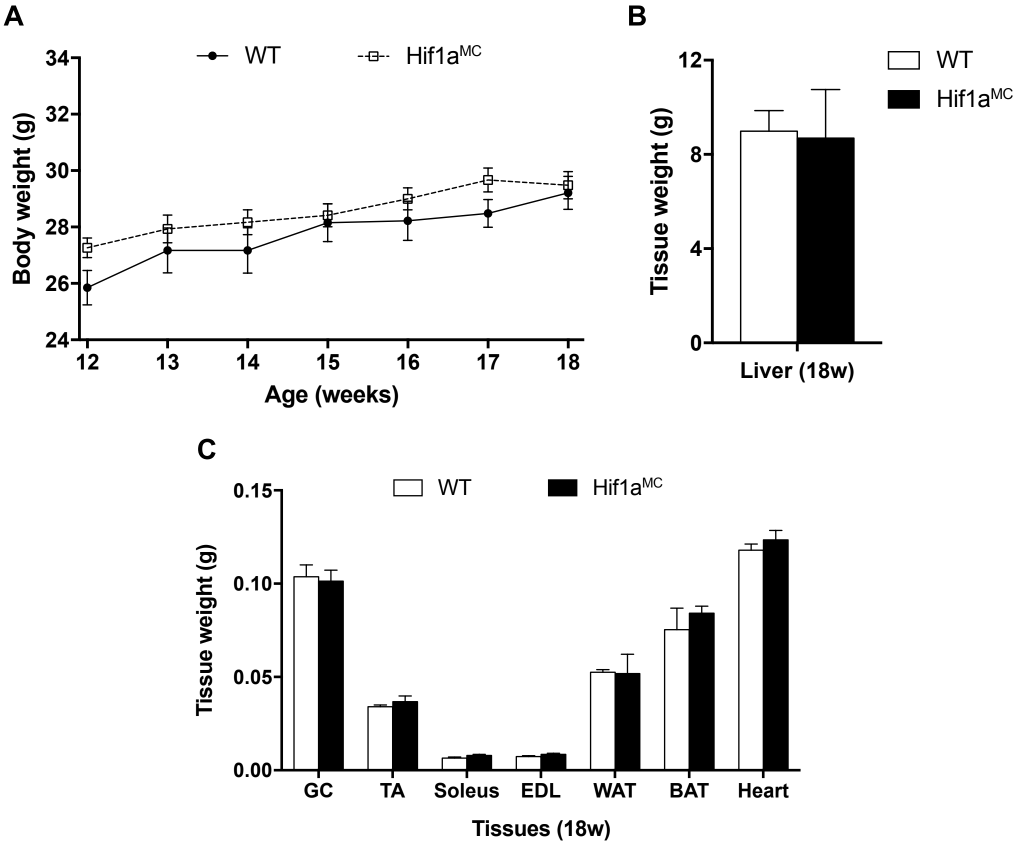

Figure 4.7: Body weight and tissue amounts were comparable between ASV-B WT and Hif1a^{MC} mice. ASV-B WT (*n* = 7) and Hif1a^{MC} (*n* = 6) mice were used for **A.** Body weight follow-up measurement from 12 to 18 weeks of age, **B.** Liver weight measurement at 18 weeks and **C.** Skeletal muscle (GC, TA, EDL, soleus), heart and fat tissue (epididymal WAT, BAT) weight at 18 weeks of age. Data show means with S.E.M. and were analyzed by two-way ANOVA (**A**), unpaired Student's *t*-test (**B**, **C**).

Body composition analysis was also performed weekly between 12 and 18 weeks in ASV-B mice with myeloid-specific *Hif1a* knockout. Fig. 4.8A shows the total lean mass ratio of mice between 12 and 18 weeks. The lean mass ratio was higher in ASV-B Hif1a^{MC} compared to WT mice during this period, however, the difference was not statistically significant. Total fat percentage decreased continuously starting from 13 weeks of age. For ASV-B WT mice, 9.1% fat amount dropped to 5.8%, while 8.5% fat amount dropped to 5% for ASV-B Hif1a^{MC} mice in this six-week period (Fig. 4.8B). Even though the fat percentage difference was not significant between the groups, reduced fat was detectable in ASV-B Hif1a^{MC} mice. As stated above, the myeloid cell-specific *Hif1a* knockout results in a pronounced inflammatory defect and inflammation is considered to be a driving factor for cachexia. Against this background, the reduced fat amount in ASV-B Hif1a^{MC} mice was unexpected.

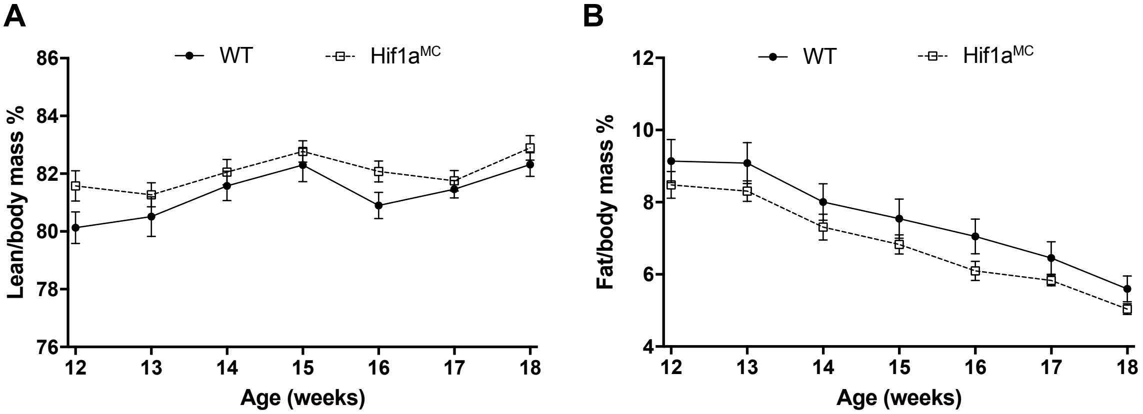

Figure 4.8: Body composition analyses of ASV-B WT (*n* = 7) and Hif1a^{MC} (*n* = 6). A. Lean and **B.** Fat mass amounts were calculated using NMR and presented as percentage of total body mass. Data represent means with S.E.M. and analyzed by two-way ANOVA.

UPS and apoptotic activities were also tested in GC muscle of ASV-B WT and ASV-B Hif1a^{MC} mice in order to analyze muscle wasting. Trypsin-like and PGPH activities of the proteasome were significantly increased in ASV-B WT and ASV-B Hif1a^{MC} mice (Fig. 4.9A). Caspase-3 and -6 activities were higher in ASV-B mice than in C57BL/6 mice, but they were comparable between ASV-B WT and ASV-B Hif1a^{MC} (Fig 4.9B). These results altogether suggest higher protein catabolism in GC skeletal muscle tissue in ASV-B WT and Hif1a^{MC} line although no effect of the cell-specific *Hif1a* knockout was observed.

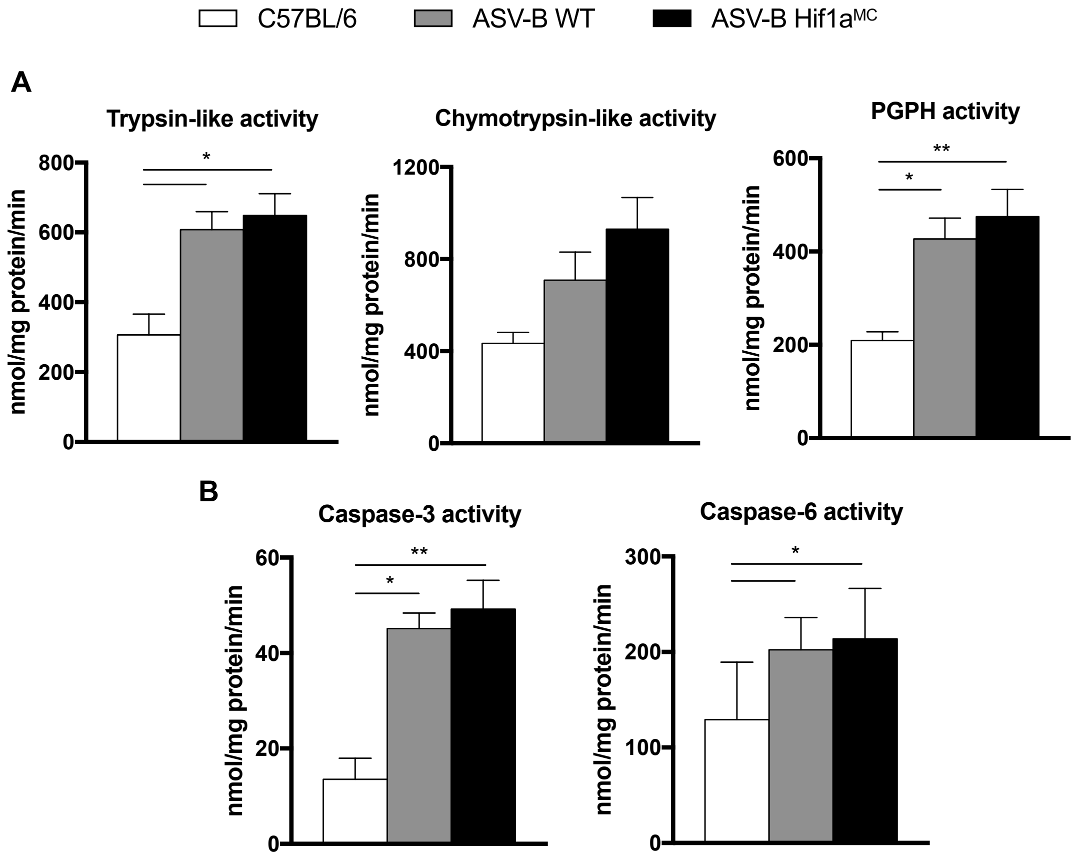

Figure 4.9: Proteolytic and apoptotic activities were increased in GC muscle of ASV-B WT and ASV-B Hif1a^{MC} mice. Control C57BL/6 (*n* = 3) as well as ASV-B WT (*n* = 10) and ASV-B Hif1a^{MC} (*n* = 10) mice were used. **A.** Proteasome activity was analyzed by measuring trypsin-like activity, chymotrypsin-like activity and PGPH activity. **B.** Apoptotic activity was determined by caspase-3 and caspase-6 activity. Data show means with S.E.M. and were analyzed by one-way ANOVA followed by Tukey post hoc test (**A**, **B**).

4.3 Effect of the myeloid cell-specific *Hif1a* knockout on cachexia in ASV-B mice

The observed fat loss dominated the cachexia phenotype in ASV-B mice. Of note ASV-B mice with myeloid cell-specific *Hif1a* knockout showed more total fat loss (3.5%) than mice with a hepatocyte-specific *Hif1a* knockout (2%). In addition to this, ASV-B mice with myeloid cell-specific *Hif1a* knockout had less fat than their WT counterparts while this not strictly the case in ASV-B mice upon hepatocyte-specific *Hif1a* deletion.

Taking all this into consideration, it was decided that the project would be continued with ASV-B mice bearing myeloid-specific *Hif1a* knockout by focusing on fat loss together with potential mechanism behind this observation.

4.3.1 ASV-B Hif1a^{MC} mice show less total fat amount

Body fat and liver were analyzed in detail with µCT imaging for ASV-B WT and ASV-B Hif1a^{MC} mice. Representative images (Fig. 4.10) show three-dimensional volume visualization of segmented bones, lungs, and fat. Automated image analysis of µCT imaging enabled the quantification of fat tissue and revealed that ASV-B Hif1a^{MC} mice had less fat volume than ASV-B WT ($P = 0.05$) (Fig. 4.10A), which is consistent with the previous NMR analysis. Liver volume was also calculated and visualized using µCT imaging (Fig. 4.10B). In ASV-B Hif1a^{MC} mice, liver volume was greater but not significantly different in comparison to ASV-B WT mice.

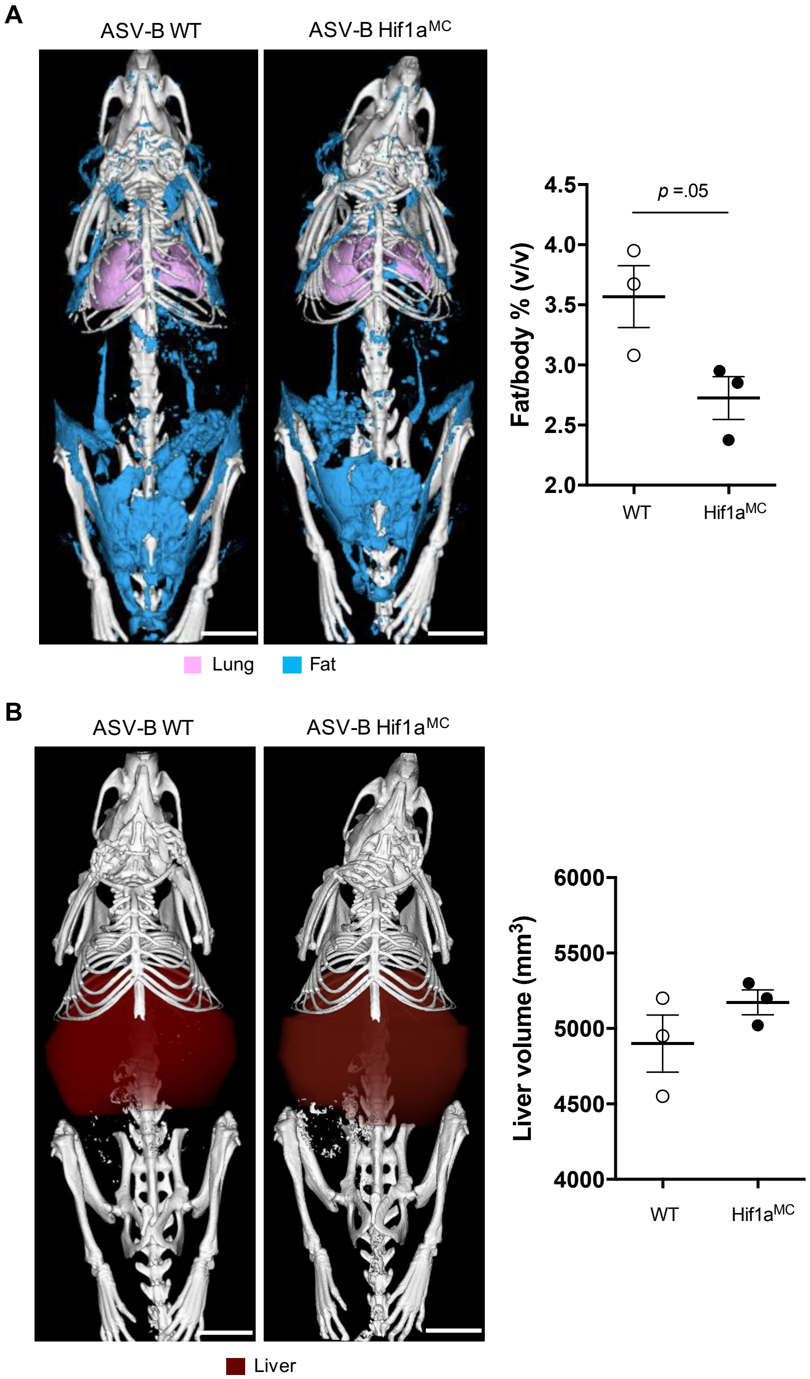

Figure 4.10: Body composition analysis of ASV-B WT and ASV-B Hif1a^{MC} mice. A. Representative images of three-dimensional volume renderings of segmented bones (white), lungs (pink), and fat (blue) upon *in vivo* µCT imaging (scale bar, 1 cm). These images indicate fat tissue locations throughout the body. Fat volume was calculated from images and presented as percentage of total body volume at the right side in the graph (n = 3 per group). **B.** Size and location of liver (brown) can be observed in representative µCT images of three-dimensional volume renderings (scale bar 1 cm). In the graph, liver volumes were calculated using µCT images (n = 3 per group). Data show means with S.E.M. and were analyzed by unpaired Student's t-test (A, B).

Next, liver weight of 12, 16 and 18 week old mice was measured to investigate whether the myeloid cell-knockout of *Hif1a* had an effect on tumor size. Liver values were similar at these time points (Fig. 4.11A). Tumor relative to whole liver area analyzed from H&E stained sections did not change in 16 week old ASV-B WT and Hif1a^{MC} mice (Fig. 4.11B).

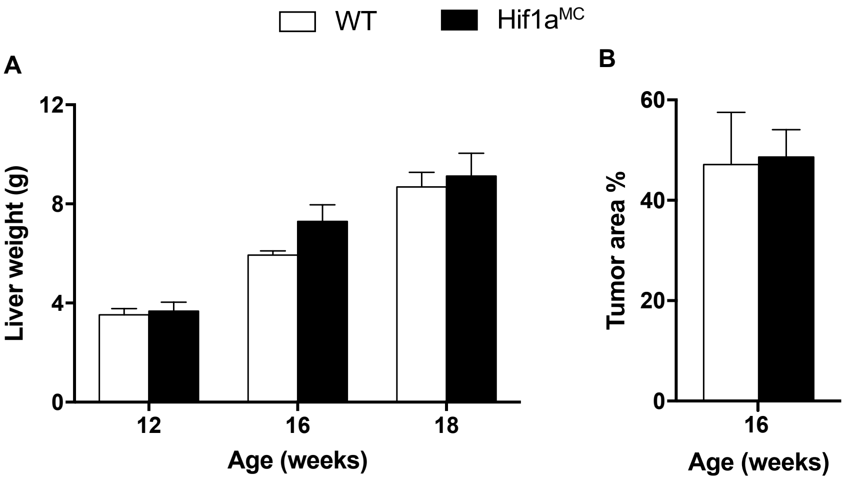

Figure 4.11. Liver weight and tumor area were not different between ASV-B WT and Hif1a^{MC} mice. A. Liver weight of mice (12, 16, 18 week old, *n* = 7, 4, 4, respectively) did not show differences between the genotypes. **B.** Quantification of H&E stained liver sections revealed that tumor area percentage of total liver area were similar in 16 week old ASV-B WT and Hif1a^{MC} mice (*n* = 3 per group). Data show means with S.E.M. and were analyzed by unpaired Student's *t*-test (**A, B**).

Blood count analysis showed that there was no difference in blood parameters of 16 weeks old ASV-B WT and ASV-B Hif1a^{MC} mice. Values of white and red blood cells, HGB, HCT, MCV, MCH, MCHC and platelets were comparable (Fig.4.12). These results revealed that the myeloid cell-specific knockout of *Hif1a* did not influence general blood count parameters in ASV-B mice.

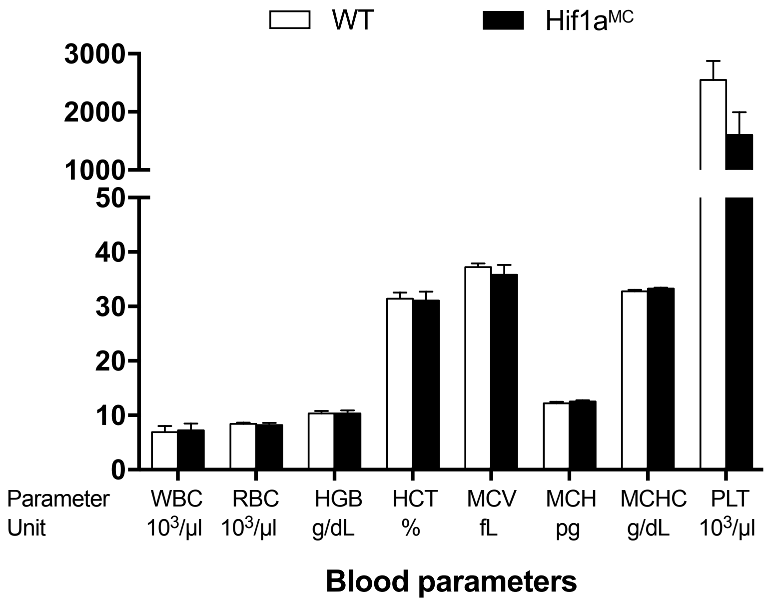

Figure 4.12: Blood values were not affected in ASV-B Hif1a^{MC} mice. Complete blood counts in ASV-B WT (*n* = 6) and Hif1a^{MC} mice and (*n* = 5) mice at 16 weeks of age were performed in automated analyzer. WBC: White blood cells, RBC: Red blood cells, HGB: Hemoglobin, HCT: Hematocrit, MCV: Mean corpuscular volume, MCH: Mean corpuscular hemoglobin, MCHC: Mean corpuscular hemoglobin concentration, PLT: Platelets. Data represent means with S.E.M. and analyzed by unpaired Student's *t*-test.

4.3.2 ASV-B WT mice have elevated levels of inflammatory cytokines

Inflammation is considered to be crucial for the pathogenesis of cachexia and elevated inflammatory cytokine levels in blood have been shown in different mouse models of CAC [74, 131]. To investigate blood serum cytokine levels in ASV-B mouse model, the Luminex® technology (explained in Section 3.3.3) was applied. ASV-B WT mice had significantly higher serum levels of pro-inflammatory cytokines Il-1β, Il-6, Tnf-α, Ifn-γ and Il-17a when compared to C57BL/6 mice. The level of the anti-inflammatory cytokine Il-10 was also elevated in ASV-B WT mice. Interestingly, ASV-B Hif1a^{MC} mice had lower levels of Il-1β, Il-6, and Tnf-α than ASV-B WT mice, which was statistically significant for Il-1β. Ifn-γ, Il-17a, and Il-10 levels were similar between the genotypes (Fig. 4.13).

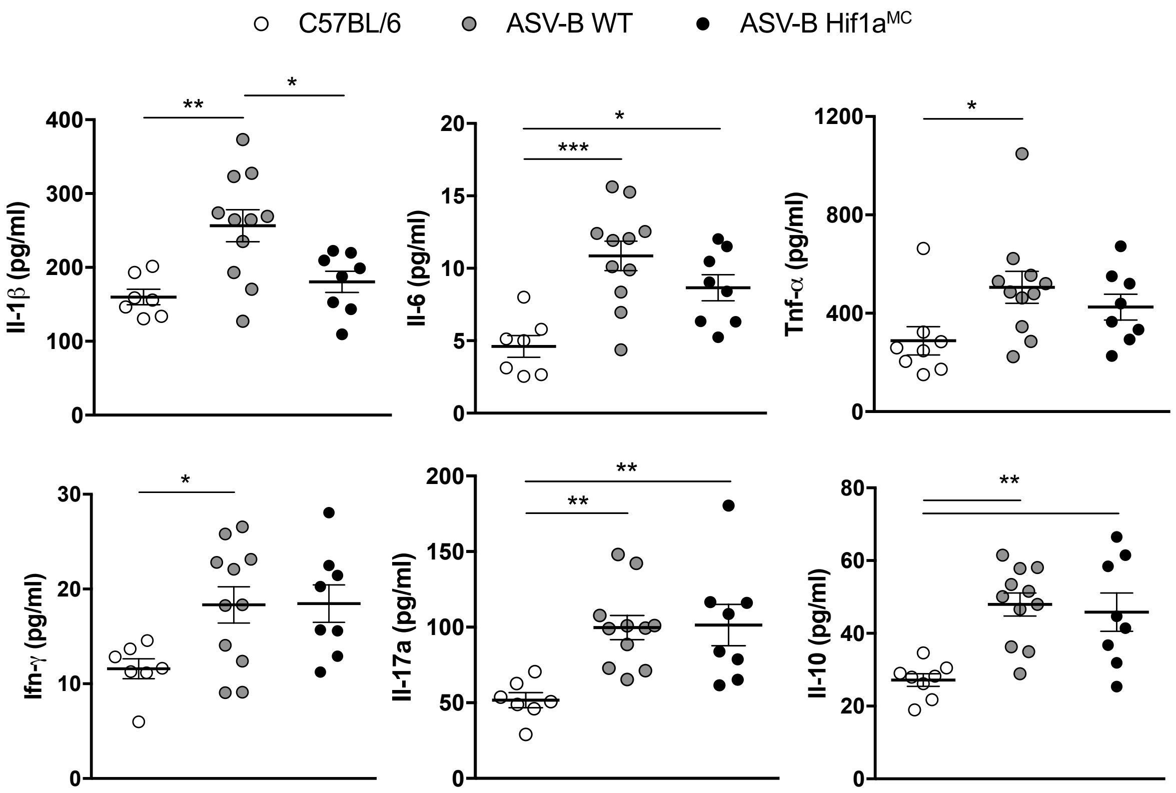

Figure 4.13: Serum cytokine levels increase in ASV-B mice. Serum collected from C57/BL6 (*n* = 7), ASV-B WT (*n* = 6) and ASV-B Hif1a^{MC} (*n* = 5) mice were analyzed for cytokine expression via immunoassay using magnetic beads. Data represent means with S.E.M. and analyzed by one-way ANOVA followed by Tukey post hoc test, $^{*}P < 0.05$; $^{**}P < 0.01$; $^{***} P < 0.001$.

As a biochemical marker of cachexia, inflammatory cytokine levels in ASV-B WT mice were higher than in C57BL/6 mice. Nevertheless, ASV-B Hif1a^{MC} mice showed a tendency towards lower levels of Il-1β, Il-6, Tnf-α compared to WT counterparts, which is a possible effect of the myeloid cell-specific *Hif1a* knockout in these mice.

4.4 Increased lipolysis and browning occurs in ASV-B mice

The results until this point indicated a striking fat tissue loss in ASV-B mice during HCC development. Since the fat amount in these mice dramatically drops between 12 and 18 weeks of age, further experiments were conducted using 16 weeks old mice. Lipolysis is a biochemical process for the breakdown of triglycerides from cellular fat droplets. Mainly, adipocytes of white adipose tissue store energy as lipids and they mobilize stored fat when required, like in fasting or during exercise for energy supply [132]. Moreover, in relation to cachexia, increased lipid mobilization has been described earlier in human gastrointestinal cancer [68, 70].

Given the loss of fat mass and volume in ASV-B mice, I hypothesized that increased lipolysis and lipid mobilization occurs in cancer-induced cachexia of ASV-B mice. To test this, adipocyte cell size was calculated in eWAT of ASV-B and control mice using H&E stained tissue sections. The quantification of adipocyte size revealed shrinkage of these cells in ASV-B mice. The frequency of relatively small cells (≤1,500 μm^2) was significantly higher and frequency of relatively big-size cells (≥2,000 μm^2) was significantly lower in ASV-B WT mice compared to C57BL/6 mice. When ASV-B WT and ASV-B $Hif1a^{MC}$ mice were compared, ASV-B $Hif1a^{MC}$ mice had a higher frequency of smaller adipocytes (≤1,000 μm^2) and a lower frequency of relatively large adipocytes (1,500-4,000 μm^2, statistically significant at 2,000 μm^2, Fig. 4.14A). Distribution of all adipocytes according to their cell area can be seen in a scatter plot diagram (Fig. 4.14B). Representative pictures show the general morphology of adipocytes that were used in this analysis (Fig. 4.14C).

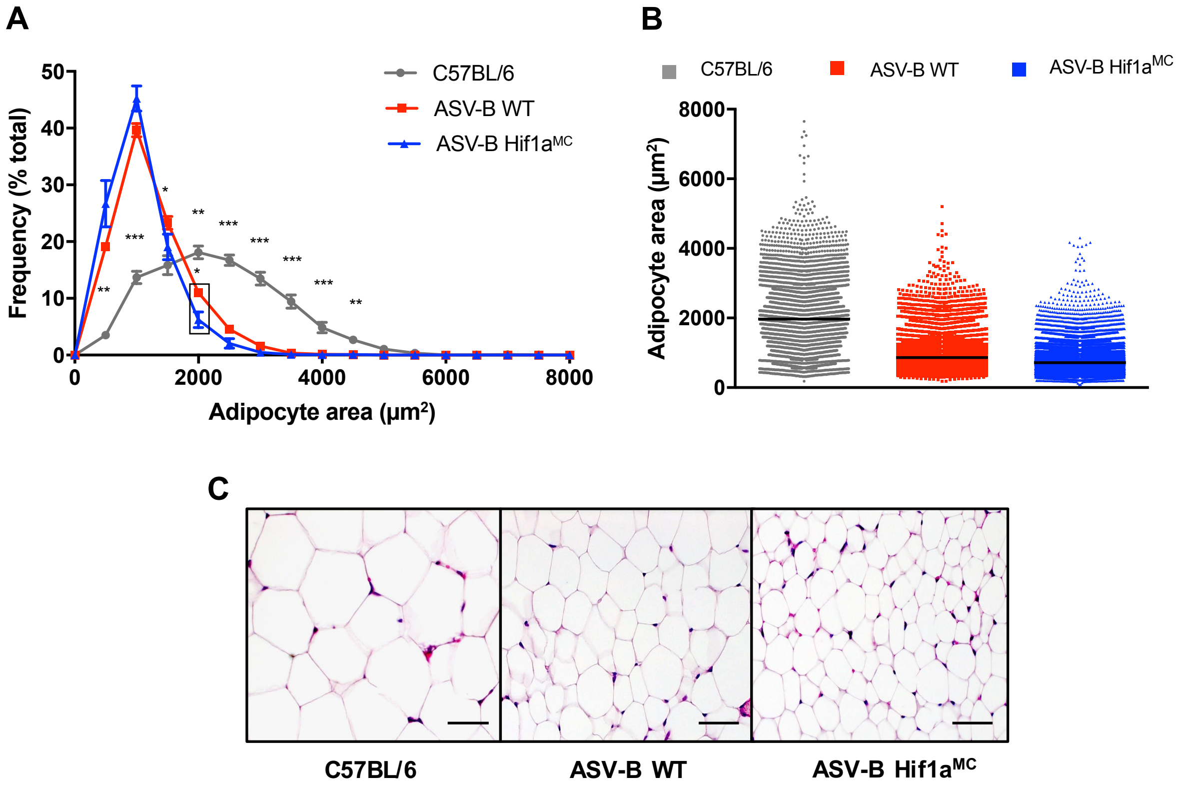

Figure 4.14: Adipocyte cell size is reduced in ASV-B mice. A. Adipocyte cell area analysis was performed as outlined in Methods. Cells were counted, and their areas were calculated automatically in H&E stained eWAT of C57BL/6 (*n* = 5), ASV-B WT (*n* = 4), and ASV-B Hif1a^{MC} (*n* = 4) mice at 16 weeks of age. **B.** Distribution of adipocytes according to their sizes in a scatter plot together with the mean of each group showed decreased cell area in ASV-B mice. **C.** Representative images of H&E staining in eWAT of 16 weeks old mice, scale bars, 50 μm. Data represent means with S.E.M. and analyzed by one-way ANOVA followed by Tukey post hoc test, $^{*}P < 0.05$; $^{**}P < 0.01$; $^{***}P < 0.001$ (**A**).

Next, glycerol release from fat tissues was analyzed via the *ex vivo* lipolysis assay. eWAT from ASV-B WT mice showed a comparable amount of glycerol release to C57BL/6 mice whereas ASV-B Hif1a^{MC} mice displayed an elevated glycerol release (Fig. 4.15A). In addition, catecholamine levels of eWAT extracts were measured via high-performance liquid chromatography (HPLC). Catecholamines are hormones which can be released from neurons, and they induce lipolysis in adipose tissues. Notably, increased noradrenaline concentration was detected in eWAT extracts from ASV-B WT mice in comparison to healthy C57BL/6 mice, while noradrenaline levels remained unaltered in ASV-B Hif1a^{MC} mice relative to ASV-B WT mice (Fig. 4.15B). Unlike noradrenaline, adrenaline was not detected in fat tissues of C57BL/6 and ASV-

B mice. Concerning the catecholamines, a previous study defined macrophages as an alternative source of catecholamine production in brown fat tissue [120], however contradictory findings were published in a subsequent report showing that macrophages do not synthesize catecholamines [133]. To asses if macrophages secrete catecholamines, I isolated BMDM cells from female ASV-B WT and Hif1a^{MC} mice followed by stimulation for classical and alternative activation of macrophages. Neither noradrenaline nor adrenaline were detected in the media supernatants of macrophages, supporting the finding that macrophages are not a likely source of catecholamines.

Finally, gene expression of hormone sensitive lipase (HSL) was performed via qPCR. HSL, which is one of the main responsible enzymes of lipolysis, is induced by hormone stimulation in adipose cells to catalyze triglyceride breakdown to fatty acids and glycerol [134]. Not surprisingly, expression of the HSL-encoding *Lipe* gene was significantly upregulated in the adipose tissue of ASV-B mice compared to healthy controls. However, between eWAT of ASV-B WT and Hif1a^{MC} mice, no difference was observed in the expression levels of the *Lipe* gene (Fig. 4.15C).

Taken together, these results support the notion of increased lipolytic activity in adipose tissue of ASV-B mice. Furthermore, enhanced glycerol release supports the observation of elevated lipolysis upon myeloid cell-specific *Hif1a* deletion.

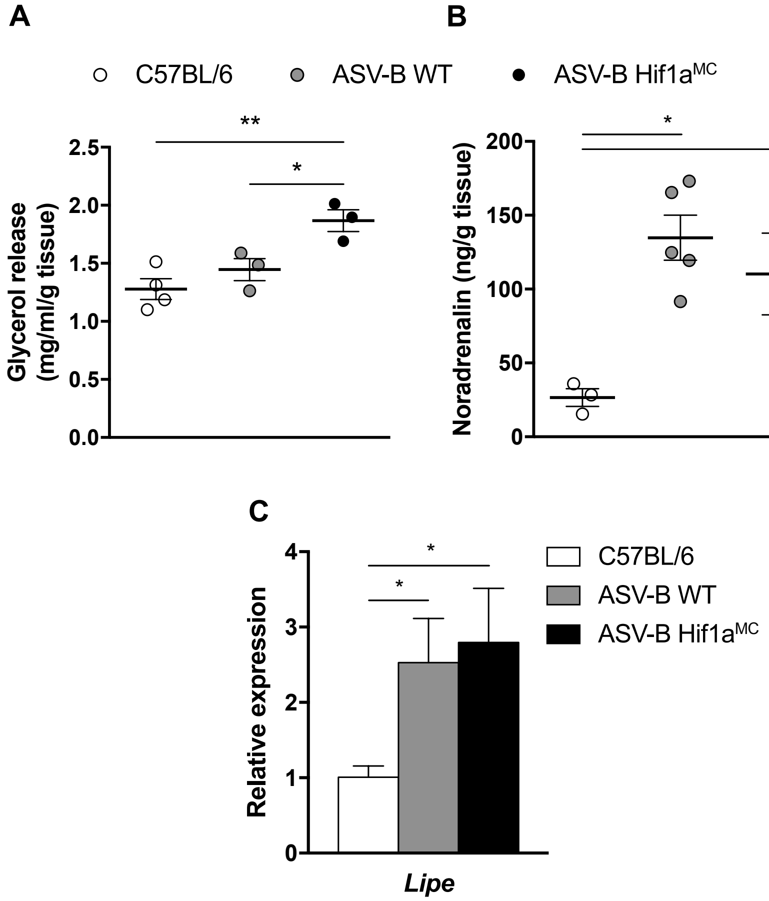

Figure 4.15: Lipolysis was increased in adipose tissue of ASV-B mice. A. Glycerol release from eWAT of 16 week old C57BL/6 (*n* = 4), ASV-B WT (*n* = 3) and Hif1a^{MC} (*n* = 3) mice. **B.** Noradrenaline levels detected via HPLC in eWAT of 16 week old C57BL/6 (*n* = 3), ASV-B WT (*n* = 5) and ASV-B Hif1a^{MC} (*n* = 4) mice. **C.** mRNA levels of *Lipe* gene (encoding for HSL) was measured by qPCR in eWAT of 16 week old C57BL/6 (*n* = 3), ASV-B WT (*n* = 3) and Hif1a^{MC} (*n* = 4) mice. Data represent means with S.E.M. and analyzed by one-way ANOVA followed by Tukey post hoc test, **P* < 0.05; ***P* < 0.01.

Browning is a mechanism that occurs in WAT to switch to a thermogenic fat ‘burning’ phenotype, resulting in increased energy expenditure. This mechanism was previously shown in mouse models of lung and pancreatic cancer cachexia [46, 80]. Fat tissue of ASV-B mice showed significantly elevated mRNA levels of browning marker genes including *Ucp1*, *Ppargc1a*, *Pparg*, *Prdm16* in comparison to C57BL/6 mice fat tissue. This result suggests that browning is one of the cachexia-related mechanisms triggered in WAT of ASV-B mice. The expression of these marker genes in WAT of ASV-B Hif1a^{MC} mice was comparable to WT mice (Fig. 4.16).

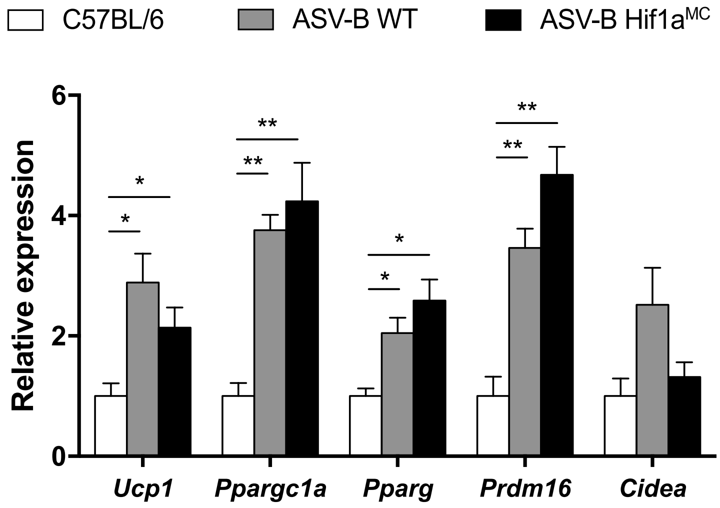

Figure 4.16: Browning occurs in adipose tissue of ASV-B mice. mRNA levels of browning marker genes (*Ucp1*, *Ppargc1a*, *Pparg*, *Prdm16, Cidea*) in eWAT of 16 week old C57BL/6 (*n* = 3), ASV-B WT (*n* = 3) and Hif1a^{MC} (*n* = 4) mice. Data represent means with S.E.M. and analyzed by one-way ANOVA followed by Tukey post hoc test, *$P < 0.05$; **$P < 0.01$.

4.5 Adipose tissue macrophages (ATMs) in ASV-B mice

4.5.1 Myeloid *Hif1a* loss decreases macrophage number in ASV-B mice eWAT

Macrophages have been studied in various aspects of adipose tissue biology, especially in obesity. They have been shown as crucial players in adipose tissue homeostasis via chronic inflammation of WAT and systemic insulin resistance [135]. In addition, macrophages are involved in local lipid regulation of adipose tissue where they are recruited to and accumulate after induction of lipolysis [107]. Based on this and on the observation of enhanced lipolysis in ASV-B mice, macrophages in adipose tissue were investigated as the next step of this thesis. Initially, eWAT samples were stained for the macrophage marker protein F4/80, and quantification of staining showed that ASV-B WT mice have increased number of adipose tissue macrophages (ATMs) compared to C57BL/6. Strikingly, this increase was completely lost in eWAT of ASV-B Hif1a^{MC} mice (Fig. 4.17). Next, the proliferation of macrophages was evaluated via the staining of the proliferation marker Ki67 (Fig. 4.18). In accordance with published findings showing that ATMs originate from bone marrow rather than proliferation of local cells [107, 136], it was not surprising that dividing macrophage ratios were quite low in adipose tissue. Indeed, there was no significant difference between C57BL/6 and ASV-B WT mice regarding the rate of mitotic macrophages. Despite the low ratio of cells, fewer proliferating macrophages were detected in ASV-B Hif1a^{MC} mice in comparison to healthy and ASV-B WT mice, suggesting a potential role of *Hif1a* in proliferation of ATMs.

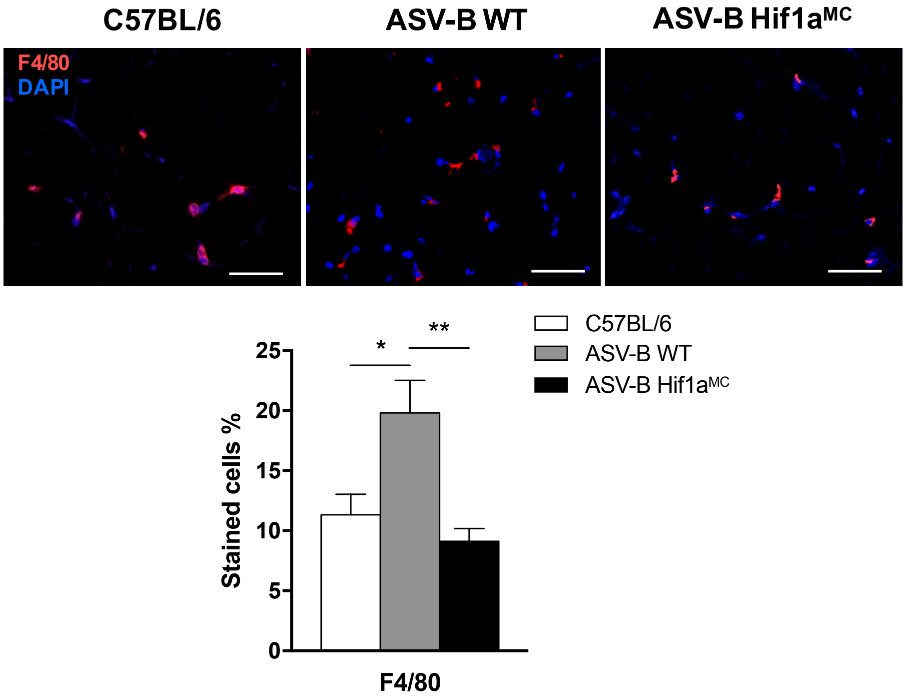

Figure 4.17: Elevated macrophage numbers in eWAT of ASV-B mice compared to healthy and ASV-B Hif1a^{MC} mice. Representative images of F4/80 immunofluorescence staining in eWAT from C57BL/6 (*n* = 5), ASV-B WT (*n* = 4) and Hif1a^{MC} (*n* = 5) mice, scale bars 50 µm, (upper panel) quantification of staining, F4/80-positive cells calculated as relative percentage of all counted cells (bottom panel). Data represent means with S.E.M. and analyzed by one-way ANOVA followed by Tukey post hoc test, *$P < 0.05$; **$P < 0.01$.

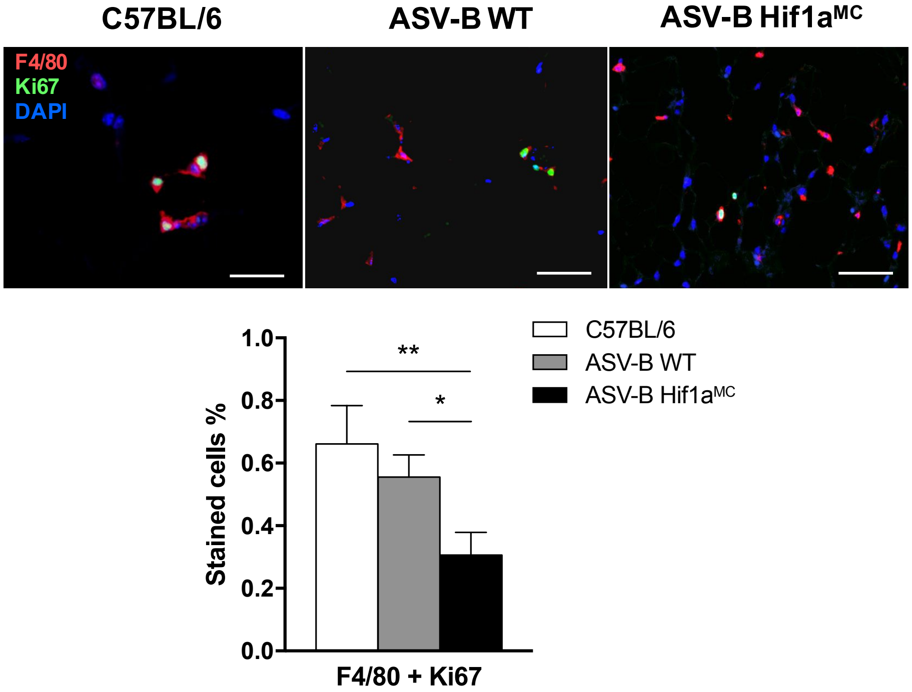

Figure 4.18: Macrophage proliferation in adipose tissue of ASV-B mice. (upper panel) Representative images of F4/80 and Ki67 immunofluorescence staining in eWAT tissue from C57BL/6 (n = 6), ASV-B WT (n = 4) and Hif1a^{MC} (n = 5) mice, scale bars 50 µm, (bottom panel) quantification of staining, F4/80 + Ki67 double-positive cells calculated as relative percentage of all counted cells. Data represent means with S.E.M. and analyzed by one-way ANOVA followed by Tukey post hoc test, $^{*}P < 0.05$; $^{**}P < 0.01$.

4.5.2 Macrophage phenotype in adipose tissue was not affected by *Hif1a*

ATMs were shown to play a crucial role in the regulation of tissue remodeling via different inflammatory features. Classically activated macrophages (CAMs) are abundant in inflamed adipose tissue in obesity, whereas alternatively activated macrophages (AAMs) are present in adipose tissue of lean or metabolically normal individuals [137]. Moreover, *Hif1a* deletion in macrophages led to decreased macrophage infiltration and reduced classically activated phenotype of macrophages in adipose tissue of high fat-fed mice [138]. Against this background, I investigated whether the myeloid cell-specific *Hif1a* deletion affected the macrophage phenotype in adipose tissue. Macrophage phenotypes in eWAT were first analyzed via gene expression levels of defined markers. The *Hif1a* knockout failed to impact on the ATM phenotype as established markers for classical (*Tnfa, Nos2, Cd274*) and alternative activation (*Arg1, Mrc1, Clec10a and Il-10*) were independent of the genotype (Fig. 4.19A). In addition, eWAT staining of an alternative activation marker Ym-1 for macrophages was not significantly different between ASV-B WT and Hif1a^{MC} mice (Fig. 4.19B).

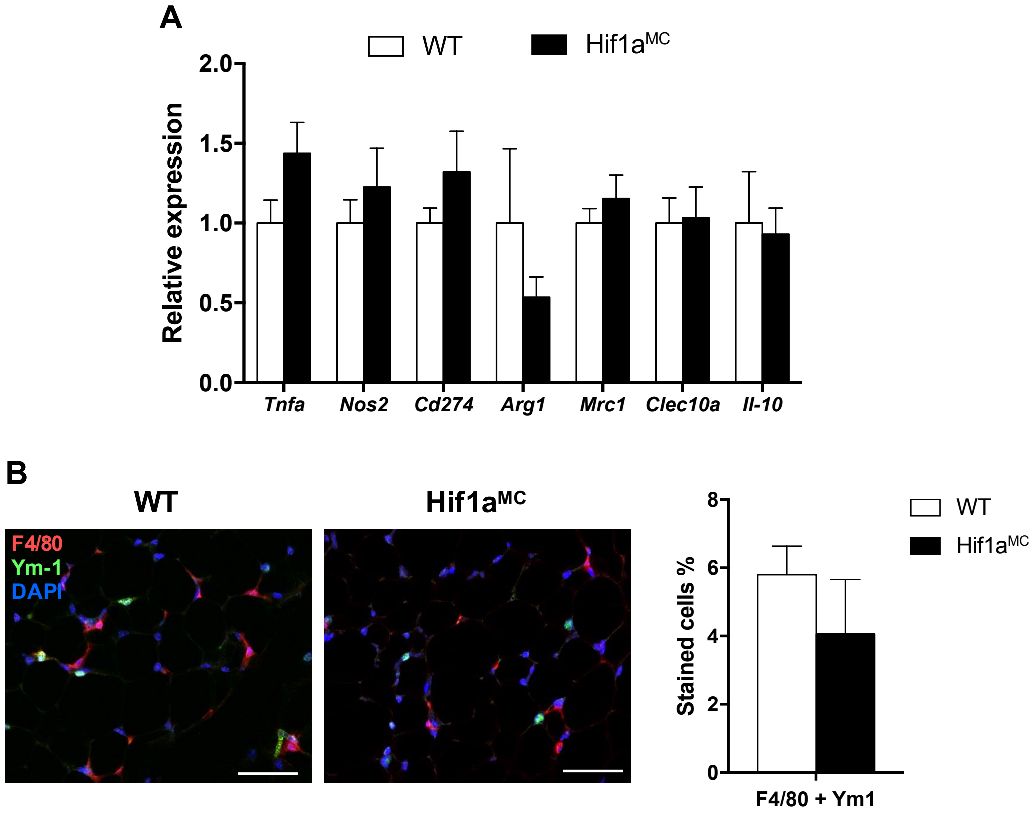

Figure 4.19: Macrophage polarization did not change between eWAT of ASV-B WT and ASV-B Hif1a^{MC} mice. A. mRNA expression analysis of markers for classically (*Tnfa*, *Nos2*, *Cd274*) and alternatively activated (*Arg1*, *Mrc1*, *Clec10a*, *Il-10*) macrophages in eWAT from ASV-B WT (*n* = 4) and Hif1a^{MC} (*n* = 5) mice. **B.** (left) Representative images of F4/80 and Ym-1 immunofluorescence in eWAT tissue from ASV-B WT (*n* = 4) and Hif1a^{MC} (*n* = 5) mice, scale bars 50 µm, (right) quantification of F4/80 + Ym-1 double staining, stained cells calculated as relative percentage of all counted cells. Data show means with S.E.M. and were analyzed by unpaired Student's *t*-test (**A**, **B**).

4.5.3 Innervation and macrophage-neuron proximity in eWAT

In the lipolysis part of the study, elevated levels of noradrenaline in ASV-B adipose tissue was noted. Following this observation, increased macrophage number was also revealed in adipose tissue of ASV-B mice. Recently, neuron-macrophage interaction in the regulation of lipolysis of adipose tissue has gained more attention. Published studies described the macrophage-associated destruction mechanisms of neuron-secreted catecholamine during aging and in obesity [139, 140]. Based on these data, I investigated whether innervation of neurons in WAT changes during cachexia in ASV-B mice. For that purpose, eWAT samples were stained for tyrosine hydroxylase (TH) protein, a well-established marker for sympathetic neurons. Even though quantification of the immunofluorescence staining revealed that ASV-B WT mice adipose tissue seems to have elevated TH, there was no statistically significant difference between the groups (Fig. 4.20A). Furthermore, total TH protein levels in eWAT of ASV-B WT and Hif1a^{MC} mice were comparable in western blot analyses (Fig. 4.20B). These results suggested that innervation of sympathetic neurons was not affected by increased lipolysis in ASV-B mice, or *vice versa*. Along with the innervation results, the elevated amount of noradrenaline in ASV-B mice adipose tissue points out that not the number but the function of neurons might increase during cachexia.

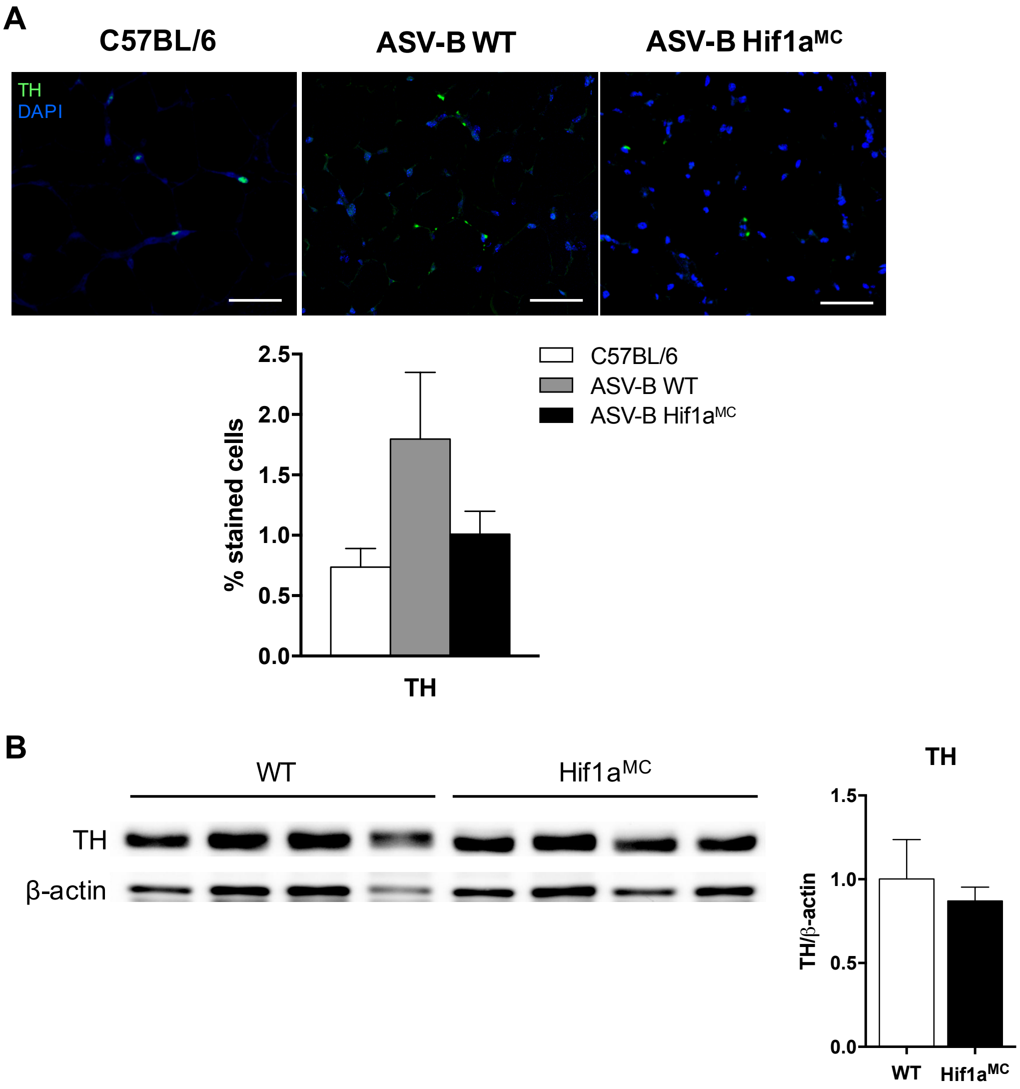

Figure 4.20: Innervation was not significantly different between C57BL/6 mice, ASV-B WT and ASV-B Hif1a^{MC} mice. A. (upper panel) Representative images of F4/80 and TH immunofluorescence in eWAT from C57BL/6 (*n* = 5), ASV-B WT (*n* = 4) and Hif1a^{MC} (*n* = 5) mice, scale bars 50 µm, (bottom panel) quantification of TH staining, stained cells calculated as relative percentage of all counted cells. **B.** (left) Western blot image of TH from 16-week-old ASV-B eWAT tissues and (right) quantification of western blot image. Data represent means with S.E.M. and analyzed by one-way ANOVA followed by Tukey post hoc test (**A**), unpaired Student's *t*-test (**B**), $^{*}P < 0.05$.

Since sympathetic neuron-associated macrophages have been described in adipose tissue and are associated with obesity via noradrenaline degradation [140], next, the number of macrophages present in the vicinity of neurons was calculated to address their potential interaction. Images of tissue samples stained for macrophages and sympathetic neurons were analyzed via automated counting by the group of Univ.-Prof. Dr. Dr. Twan Lammers (Institute for Experimental Molecular Imaging, University Hospital RWTH Aachen). ASV-B WT and Hif1a^{MC} mice had similar macrophage numbers around neurons whereas they showed less macrophages around neurons in eWAT compared to C57BL/6 mice. These results suggest that the interaction of macrophages with neurons is of lesser functional relevance in this setting. In light of the increased noradrenaline levels in adipose tissue during cachexia (Fig. 4.15B), this points towards a contrasting phenomenon compared to obesity, where noradrenaline availability is blocked by macrophages in a crosstalk with neurons resulting in reduced lipolysis and enhanced fat storage [140].

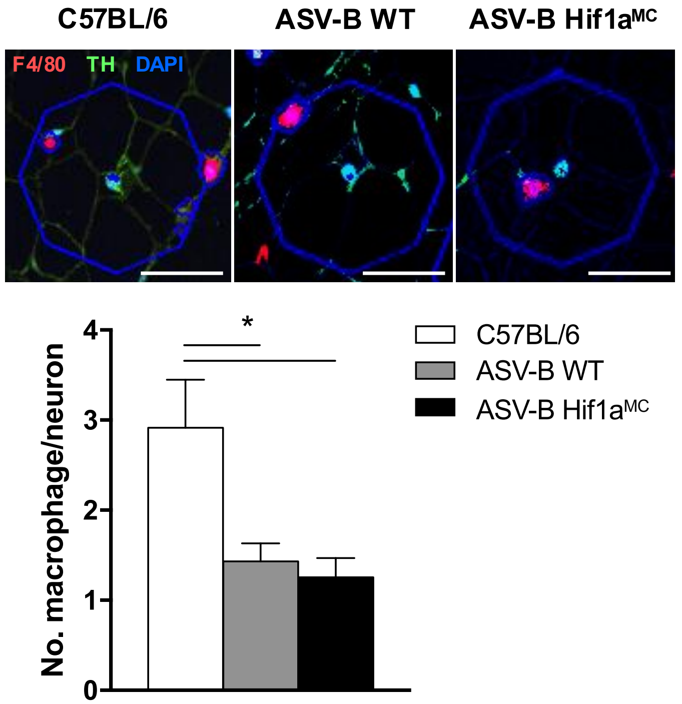

Figure 4.21: Macrophage-neuron proximity in adipose tissue of ASV-B WT and Hif1a^{MC} mice. (upper panel) Representative images with concentric rings of the automated quantification for macrophages in the vicinity of neurons, scale bars 100 µm, (lower panel) ratio of macrophages in the vicinity of neuron cells. Cells were counted from F4/80- and TH-stained immunofluorescence images in eWAT of C57BL/6 (n = 3), ASV-B WT (n = 3) and Hif1a^{MC} (n = 5) mice. Data represent means with S.E.M. and analyzed by one-way ANOVA followed by Tukey post hoc test, *$P < 0.05$.

4.5.4 Hypothalamic pro-opiomelanocortin (POMC) neuron activation in ASV-B mice

In addition to the regulation of lipid metabolism by peripheral sympathetic neurons, the central nervous system (CNS) has been shown to regulate lipid uptake or lipid mobilization of adipose tissue. The sympathetic nervous system connects WAT cells with homeostatic control areas in the CNS like the hypothalamus and other brain regions [141]. For this reason, with the help of our collaborator Dr. Marco Koch (Institute of Anatomy, University of Leipzig) the activation of pro-opiomelanocortin (POMC) neurons in the arcuate nucleus (ARC) of hypothalamus was analyzed. All mice showed a similar amount of POMC+ cells, demonstrating that the appropriate anatomical area was analyzed (Fig. 4.22A). The activation state of POMC+ neurons in the ARC was addressed by the staining against c-Fos, which is a marker of neuronal activation. ASV-B WT mice showed significantly increased number of c-Fos positive cells compared to healthy mice, indicating increased activation of POMC neurons. Myeloid cell-specific *Hif1a* knockout ASV-B mice showed a decreased amount of activated POMC+ cells compared to ASV-B WT mice, even though the difference was not significant (Fig. 4.22B).

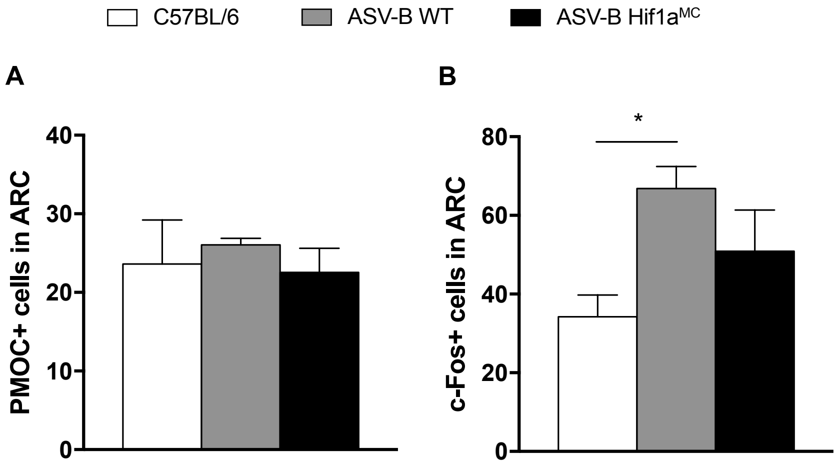

Figure 4.22: A. Hypothalamus staining for POMC+ neurons and **B.** c-Fos staining in the same area of the hypothalamus were performed. Perfused brain samples of C57BL/6 (*n* = 2), ASV-B WT (*n* = 5) and Hif1a^{MC} (*n* = 3) mice at 16 weeks of age were used. Data represent means with S.E.M. and analyzed by one-way ANOVA followed by Tukey post hoc test, *$P < 0.05$.

4.6 Quantification of body composition in human HCC patients

In this thesis so far, cancer cachexia and its potential mechanisms have been described in a mouse model of HCC. Animal models have been used in science to investigate mechanisms and test novel therapies before applying discoveries to humans. The physiological and anatomical similarities between humans and animals have made the use of these models suitable for research, although it is evident that the results of many animal experiments could not be confirmed in human studies [142]. Based on this, as the last step of the project, body composition of HCC patients was evaluated to check whether the cachexia phenotype occurs in this setting. Mourtzakis *et al.* reported an objective way of calculating body composition using CT images of the L3 region. They showed that the muscle and fat area from a single L3 image are strongly associated with whole body fat as well as muscle compartments in healthy cohorts and cancer patients. Using this approach, area of total muscle, VAT and SAT can be accurately calculated [128]. 47 HCC patients from the Department of General, Visceral, and Transplantation Surgery at the University Hospital RWTH Aachen were selected for L3 analysis. Only patients without underlying cirrhosis were analyzed as the ASV-B model does not show fibrotic changes in the liver. First, L3 images were selected from CT scans of all patients, and these images were analyzed with sliceOmatic software (version 5.0, TomoVision) for muscle and fat area detection. After the correction of calculated area values with the stature of the patients, the cohort was divided into tertiles for L3 index, and lowest tertiles were compared to middle and high tertiles. This patient cohort showed that 40% of the patients have a low muscle amount, 32% have a low visceral adipose tissue (VAT) amount, and 36% have low subcutaneous adipose tissue (SAT) amount. Weight- and height-based calculation was accounted for 38% of the patients with low body mass index (BMI) (Table 1). Representative images of L3 images can be observed in Figure 4.23A.

Table 1: Body composition and BMI results of 47 HCC patients. The patient group was divided into tertiles for each L3 index, and lowest tertiles were compared to medium/high tertiles and expressed as group percentages. VAT (visceral adipose tissue), SAT (subcutaneous adipose tissue) and BMI (body mass index).

***n*=47**	**L3-muscle index (cm^2/m^2)**	**L3-VAT index (cm^2/m^2)**	**L3-SAT index (cm^2/m^2)**	**BMI**
Low	40%	32%	36%	38%
Medium/high	60%	68%	64%	62%

L3-VAT index results were also shown as a distribution graph based on the cut-off value of 35. Figure 4.23B shows the low and medium/high groups for the visceral fat amount.

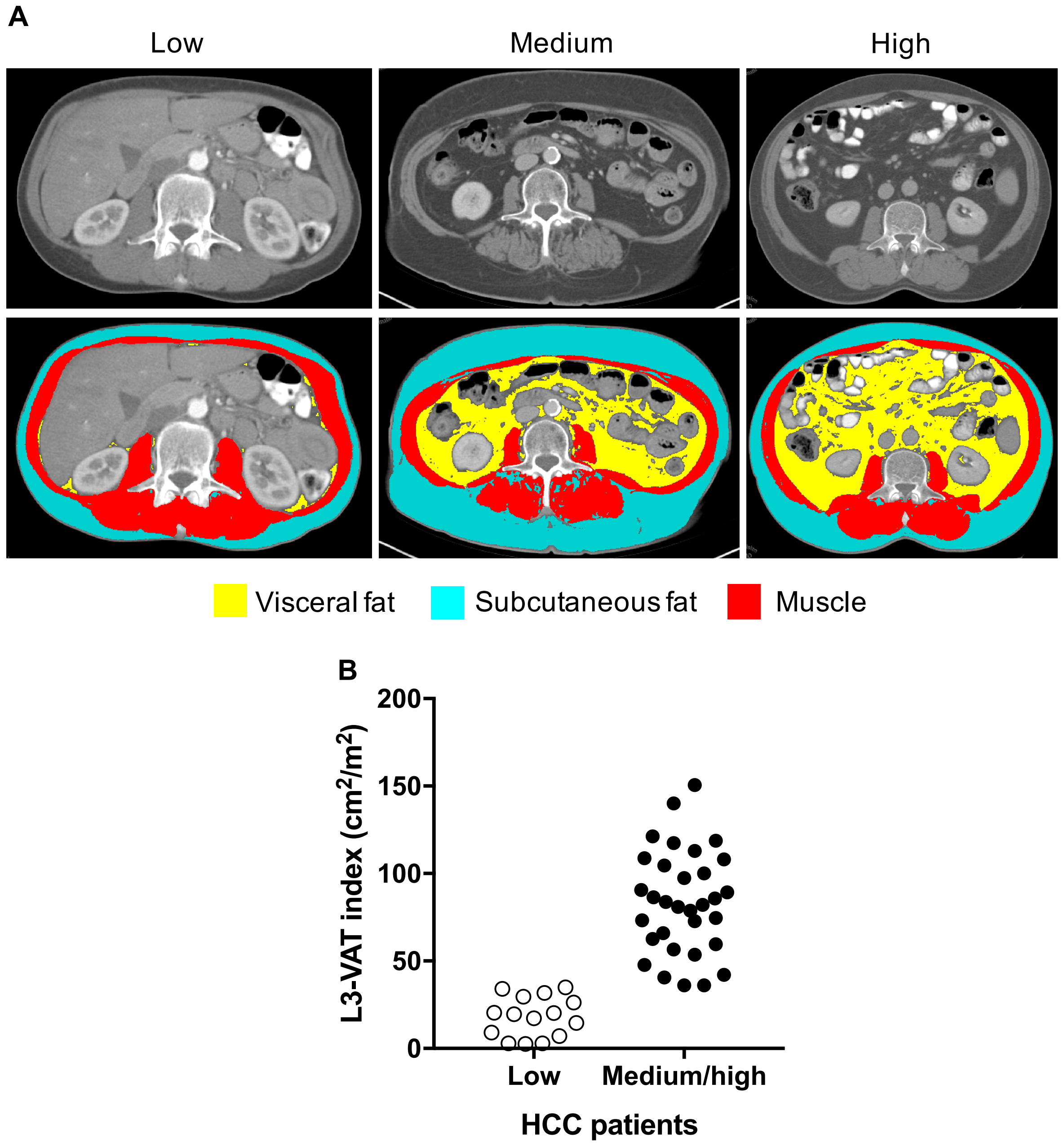

Figure 4.23: A. Representative L3 images of patients with low, medium and high L3-VAT index. Muscle and fat areas are labeled with specific colors for calculation by the software. **B.** Distribution of patients according to L3-VAT index. The group with low L3-VAT index was composed by a cut-off value of 35.

The results indicate that the observation of visceral adipose tissue loss in the ASV-B mouse model can be confirmed in a subgroup of HCC patients. This further demonstrates the potential applicability of the ASV-B model for translational studies addressing HCC-associated cachexia.

5. Discussion

5.1 ASV-B mice develop cachexia

The clinical management of HCC is challenging since the majority of the patients are diagnosed at late stages of the disease. The major problems include resistance towards chemo- and radiotherapy as well as limited resection options due to the size of tumor nodules and reduction of the functional liver reserve. While clinicians have been focusing on these obstacles for a long time, the important aspect of general body weakness and decreased in muscle mass strength (sarcopenia) experienced by HCC patients received a lot less attention. However, recent publications from different groups showed the importance of sarcopenia and cachexia for the clinical care of HCC patients [143], e.g. for predicting the prognosis [144, 145] and therapy response [146]. Not only for HCC, but also for many other types of cancer, cachexia is a clinically relevant problem affecting multiple organs. Cachexia is a complex disease and driven by a variable combination of different factors like food intake, hormones, cytokines, growth factors and inter-organ crosstalk [147]. It is therefore mandatory to use relevant preclinical models to better understand the pathogenesis of cachexia, and to be able to identify the underlying molecular and cell biological mechanisms on a whole organism level.

The available animal models for cachexia research are mainly rodent models. Mouse models of colon cancer such as the C26 carcinoma [148, 149] and APC^{min} intestinal adenoma [96] models have been identified for cachexia, as they develop muscle and fat loss. Moreover, mouse models of pancreatic cancer [80, 150], Lewis lung carcinoma [151], and melanoma (B16 model) [152] were also reported to be able to induce cachexia in mice. In this study, a robust cachexia phenotype is described for the first time in the well-established ASV-B mouse HCC model. Main characteristics of cachexia were noted in ASV-B mice, e.g. decreased skeletal muscle and heart mass compared to healthy controls. Furthermore, fat loss with phenotypical observation (Fig. 4.1 and 4.2) was present over time as well as increased inflammatory cytokines in serum (Fig 4.13) and anemia (Fig 4.3). In the literature, the only widely used model for HCC up to now is the Yoshida ascites hepatoma 130 model [153]. Indeed, this model is useful especially for testing the efficacy of novel treatment agents for cachexia [154, 155]. However, this model does not mimic the pathogenesis of HCC and reflect the liver microenvironment due to the establishment of the model via implantation of tumor cells to the peritoneal cavity. In addition to the Yoshida model, other ectopic models rely on established cancer cells, which do not necessarily mirror the original tumor very well [129]. For instance, the Yoshida 130 cell line has been established more than 60 years ago [156], and it is reasonable to conceive that the cells have acquired a lot of additional changes since then.

Another animal model of HCC-associated cachexia is the well-established chemical model based on di-ethyl-nitrosamine (DEN) injection. DEN-induced HCC mice developed cachexia with 50% penetrance at 16-18 months of age [80]. Although this provides another mouse model for HCC-induced cachexia, the long lifespan and cachexia development in only 50% of mice after such a long time period are surely disadvantages for this model in practice. On the other side, in ASV-B mice, cachexia could be detected already at 12 weeks of age in 100% of mice, which enhances the reproducibility of the experiments.

Overall, in the initial phase of this thesis, cachexia was identified in an established transgenic mouse model of HCC. As reliable and practical murine models for HCC-associated cachexia are lacking, the ASV-B model represents a valuable addition to the existing methodology.

5.2 Myeloid cell-specific *Hif1a* deficiency aggravates loss of adipose tissue in ASV-B mice

The HIF-1α transcription factor has been found to be overexpressed in a plethora of cancer types. HIF-1α target genes are involved in various critical steps of cancer biology, e.g. angiogenesis, glucose/energy metabolism, cell survival, and many others. Accumulating evidence from gain and loss of function studies confirmed that HIF-1α is involved in tumor growth, vascularization, and metastasis [113]. Taking this into account, the importance of *Hif1a* in hepatocytes for cachexia was investigated with the Cre-loxP system in ASV-B mice. *Hif1a* deficiency in hepatocytes did not influence the cachexia development in ASV-B mice (Fig. 4.4, 4.5), possibly as a result of similar tumor burden, which is an important determinant for cachexia severity [157]. Of note, a previous study also reported that HIF-1α did not change tumor growth in human HCC cell lines and animal models [158]. Since negative changes in body composition are well-defined signs of cachexia, NMR analyses were performed for quantification purposes (Fig. 4.5). Despite the muscle weight decrease in ASV-B mice, total body lean mass was found to be increased, which is an unusual finding in cachexia. However, this is due to the detection of internal organs and tumor tissue as lean mass in NMR measurement [150, 159], rendering total lean amount not an ideal reference value to evaluate cachexia in ASV-B mice.

As mentioned previously, HIF-1α is important in the inflammatory responses of myeloid cells [119], which are involved in cancer-associated inflammation [160]. In this regard, the importance of *Hif1a* in myeloid cells for the course of cachexia was also investigated in this thesis. It could be shown that cachexia-related measurements including body weight, tumor load and specific tumor area, muscle tissue weight and catabolic activity as well as fat tissue amount (BAT and eWAT), were not significantly altered, suggesting no significant effect of the myeloid cell-specific *Hif1a* knockout (Fig. 4.7, 4.9, and 4.11). Additionally, body composition values for lean and fat proportion were similar (Fig. 4.8). However, it was intriguing to note that myeloid cell-specific *Hif1a* knockout mice, which are known to harbor a defect in inflammation, showed reduced fat in all stages of HCC development in ASV-B mice. This is rather unexpected since one could assume that *Hif1a* deficiency in myeloid cells would translate into a protective effect against cachexia due to the impaired inflammatory response in these mice (Fig. 4.13) [115, 119]. This is an interesting finding questioning the general cachexia-supporting role of inflammation and pointing towards novel aspects of macrophages for fat metabolism in cachexia that have not been previously appreciated.

5.3 Lipolysis and browning of adipose tissue in HCC-induced cachexia

Loss of adipose tissue is a known phenomenon of cancer-associated cachexia that has been observed in patients as well as animal models [161]. In this regard, the fat loss observed in the ASV-B model is in line with other cancer cachexia animal models including Yoshida AH-130 rat model [161, 162]. In adipose tissue, fat content can be affected by several mechanisms: lipolysis (lipid breakdown), lipid storage, adipogenesis, and cell death [163]. Studies on cachexia and adipose tissue revealed that increased lipolysis is the key mechanism behind the fat loss in cancer cachexia [32]. This has been supported by high lipolysis rates in cancer cachexia patients (via measuring fasting plasma fatty acids or glycerol) [72] and morphological changes in adipose tissue including shrunken cells and increased interstitial space in mouse models [66]. Furthermore, HSL, a metabolic lipase and rate-limiting enzyme of the lipolytic pathway, was detected to be highly expressed in cancer patients with cachexia compared with those without [72, 164]. In line with these results, morphological changes in adipose tissue and extensive decrease in adipocyte cell size (Fig. 4.14) as well as increased HSL expression (Fig. 4.15) have all been observed in ASV-B mice, verifying the increased lipolysis. In the regulation of lipolysis, one of the major pathways is neuronal control, in which catecholamines released from sympathetic nerves bind β3-adrenoceptors to induce HSL and stimulate lipid breakdown [165]. This mechanism increased the lipolysis rate upon catecholamine stimulation in adipocytes, which were isolated from cachectic cancer patients [72]. Notably, ASV-B mice exhibited significantly higher levels of the catecholamine noradrenaline in adipose tissue indicating the potential involvement of neural activation/β-adrenergic stimulation for lipolysis in ASV-B cachexia. Altogether, these findings support the notion that cachexia-induced lipolysis pathways are activated in ASV-B mice.

As indicated previously, myeloid cell-specific *Hif1a* deficiency led to a decrease in total body fat of ASV-B mice. However, morphology and lipolysis analyses failed to identify the underlying mechanism(s) (Fig. 4.14, 4.15). The only difference was observed in *ex vivo* glycerol release of isolated fat pads, where increased values were detected in myeloid cell-specific *Hif1a* knockout mice, suggesting more efficient mobilization of fat. As an interesting point in this assay, glycerol release from ASV-B WT mice was not higher than that from tumor-free mice (Fig. 4.15). This might be a methodological disadvantage of the *ex vivo* lipolysis assay since the detected basal level of glycerol release in healthy C57BL/6 mice is already 2-fold higher than the reference values in the literature [166]. Another possibility could be that the levels of basal lipolysis are comparable between these mice at the investigated age. Since a lipolytic agent for stimulation of lipolysis were not used in this assay, only basal rates were identified [167]. It is conceivable to conclude that basal lipolysis rate does not change in tumor-bearing mice, however, stimulated lipolysis increases as high noradrenaline levels were detected. Further analyses may show the exact mechanism of lipolysis to elucidate the complete mechanism(s) of lipid breakdown in ASV-B mice.

Energy metabolism imbalance is considered to be a critical obstacle in cancer cachexia. In this context, reduced energy intake is often associated with anorexia and malnutrition, however, the wasting process of cachexia is an important cause of increased resting energy expenditure. Therefore, cancer cachexia patients suffer due to a negative energy balance even in case of sufficient nutrition intake [32]. In relation to energy status, recent studies using different mouse models of cancer cachexia (lung and pancreatic cancer) reported a switch from ATP generation to thermogenic activity in WAT [46, 80]. In this ‘browning’ process, adipocytes of WAT elevate the expression of thermogenesis genes such as in brown adipocytes, not only under cold exposure but also due to sympathetic stimulation. Data in this thesis about the ASV-B model suggest a browning phenotype via increased gene expression of thermogenic genes (Fig. 4.16) and also a shift in the energy balance towards increased expenditure, considering the fact that no reduced food intake was observed in ASV-B mice (Fig 4.1). At this point, future work to measure metabolic activity of these mice e.g. energy expenditure, respiratory exchange ratios, and spontaneous motility could provide further important information about the energy metabolism (possibly a hypermetabolic state) during cachexia in ASV-B mice.

5.4 Macrophage accumulation in adipose tissue is affected by *Hif1a*

Macrophages gained much attention after the initial description of their infiltration into WAT during obesity, which was reported in 2003 [104, 136]. Following studies confirmed the link between ATMs and inflammation and insulin resistance emphasizing them as important regulators in the fat metabolism. During obesity, significantly increasing number [136], inflammatory features [103], and different localization [168] of macrophages were reported. Although ATMs have been mostly associated with obesity, they are also known to be present in lean adipose tissue where they impact on adipose cells via various regulatory mechanisms. Kosteli *et al.* reported that lipolysis, induced by fasting or pharmacologic adrenergic activation in mice, results in macrophages influx into WAT. In this case, ATM adopt an anti-inflammatory phenotype and ultimately inhibit lipid release [107]. In line with this report, the increased lipolysis of ASV-B mice was paralleled by greater macrophage abundance in WAT (Fig. 4.17). However, this phenotype was inhibited upon *Hif1a* deletion in macrophages, suggesting that inhibition of ATM recruitment led to increased lipolysis and fat tissue loss in the conditional *Hif1a* knockout mice. This result possibly explains for less amount of fat in *Hif1a* knockout HCC mice via less macrophage abundance in adipose tissue, however, how macrophage abundance affects or regulates lipolysis is a question still open for investigation.

To the best of my knowledge, this is the first study showing a functional significance of macrophages in HCC-induced fat loss. In an earlier study by Bing *et al.*, a mouse model of colon CAC was analyzed for macrophages in WAT. In contrast to ASV-B mice, this model had no apparent WAT infiltration of macrophages [66]. This difference might be explained by the different cancer type, however, it should be taken into consideration that Bing *et al.* only showed H&E staining of tissue without a distinct identification of macrophages via specific immunostaining. In a patient study of different gastrointestinal cancer types, greater macrophage numbers in WAT were detected in cachectic patients compared to weight-stable patients [169], underscoring the need for further studies to address the significance of macrophages in cancer cachexia.

Reduced infiltration of macrophages into WAT in ASV-B Hif1a^{MC} mice during cachexia (Fig. 4.17) points towards impaired chemotaxis and migration of *Hif1a* deficient macrophages, in line with published literature using different pathological conditions [119, 170]. In this regard, the stimuli that attract macrophages to adipose tissue is also crucial. This topic has not been addressed in this thesis, however, earlier studies revealed adipocyte-secreted chemokines such as monocyte chemoattractant protein-1 (MCP-1/CCL2) as well as TNF-α, IL-6, and free fatty acids as potential candidates [107, 171]. Noteworthy, expression of the MCP-1 receptor CCR2 on monocytes [172] and toll-like receptor 4 (TLR4) signaling [173], which mediates the effect of free fatty acids [174], are strongly influenced by HIF-1α. This possibly accounts for the reduced macrophage abundance in adipose tissue upon *Hif1a* deletion. In addition to macrophage abundance, proliferation of ATMs was affected by the *Hif1a* knockout. While local proliferation of ATM has been shown in obesity before [175], in this thesis, local ATM proliferation in the setting of cancer cachexia associated fat loss is reported. A role of HIF-1α in macrophage proliferation was shown before for bovine macrophages after infection with the parasite *Theileria annulata* [176], but not for murine macrophages. Of note, the ratio of proliferating macrophages is rather small, therefore the importance of this result regarding the function of macrophages for cachexia remains to be addressed by future analyses.

To further describe the biological aspect of ATMs in HCC-induced cachexia, the macrophage phenotype was analyzed in adipose tissue of ASV-B mice. A functional significance of macrophage polarization for metabolic diseases could be assumed as pro-inflammatory macrophages with a classically activated phenotype dominate adipose tissue in obesity. The general view is that a high ratio of classically over alternatively activated macrophages predominates in obesity, while in the lean healthy adipose tissue, alternatively activated macrophages (AAMs) are the rule [177]. Indeed, AAMs are also present in WAT of ASV-B mice, whereas no effect of HIF-1α deletion on macrophage polarization of ATMs was detected (Fig. 4.19). To a certain extent this contrasts with an *in vitro* study by Takeda *et al.*, showing reduced ability of *Hif1a*-deficient macrophages to polarize into classically activated macrophages [178]. This discrepancy could be explained by the different experimental settings used and once again illustrates the importance of the tissue context and the microenvironment for the analysis of (inflammatory) cell biology.

5.5 Hypothalamic activation and WAT innervation does not underlie the enhanced fat loss in ASV-B Hif1a^{MC}

The hypothalamus is a part of the central nervous system that controls food intake and energy expenditure through the two specific types of neuronal populations in the arcuate nucleus (ARC): appetite promoting (orexigenic) agouti-related peptide (AgRP) neurons and satiety promoting (anorexigenic) POMC neurons. The coordinated regulation of hypothalamic circuits, termed the melanocortin system, is crucial for the maintenance of energy balance and feeding behavior, and any disruption in this regulation can result in metabolic diseases [179]. The hypothalamic involvement in cachexia has firstly been identified with the effect of systemic inflammation on neurons in the brain. PMOC neurons, for instance, can express IL-1β receptors that can initiate the activation of the central melanocortin system in the hypothalamus suggesting that cytokines may interfere with energy balance by influencing hypothalamic centers during cachexia [180]. In accordance with this phenomenon, ASV-B WT mice also exhibited increased number of activated POMC cells in the hypothalamus (Fig. 4.22), implying that the activation of the central melanocortin system is involved in cachexia development of this mouse model, especially regarding lipid mobilization [141]. *Hif1a* deletion in myeloid cells resulted in a tendency towards reduced activated POMC cells in ASV-B mice (Fig. 4.22). This could be explained by the functional relevance of inflammatory cytokines for hypothalamic activation, since as shown earlier in this thesis, *Hif1a* deficiency in myeloid cells reduced systemic IL-1β levels in tumor-bearing mice (Fig. 4.13). In the characterization part of ASV-B cachexia in this thesis, I observed that these mice do not show anorexia (Fig. 4.1). Despite no reduced food intake, increased activity of POMC neurons in ASV-B mice suggests a stimulation of the ARC through leptin. It has been shown in previous studies that excitation of POMC neurons by leptin rather than other stimulators resulted in normal food intake but increased energy expenditure [181, 182]. Therefore, a possible effect of leptin regarding HCC-induced cachexia should be evaluated in future analysis.

Given that the CNS exerts hypothalamic activation on WAT through the sympathetic nervous system [183, 184], and the detection of high levels of noradrenalin on WAT in ASV-B mice (Fig. 4.15), it is reasonable to assume that sympathetic innervation could be involved in the regulation of lipolysis. Of note, ASV-B mice showed no significantly increased number of sympathetic neurons (Fig. 4.20). This could imply that not only innervation of WAT, but also the activation of sympathetic neurons is important for catecholamine release and, ultimately, stimulation of lipolysis [185].

Collectively, these results suggest a functional interplay of pro-inflammatory cytokines and the hypothalamus-peripheral sympathetic nervous system axis in regulating tumor-associated lipolysis in ASV-B mice. Nevertheless, the effect of CNS activation on lipolysis of adipose tissue fails to explain increased adipose tissue loss with *Hif1a* deficiency in myeloid cell compared to ASV-B WT mice. Overall, this strongly argues for a role of local macrophages in the regulation of cancer cachexia-induced fat loss.

5.6 A subgroup of patients shows low muscle and/or fat amount in HCC cohort

In addition to the mouse data in this thesis, a human HCC cohort was analyzed for cachexia. In line with the mouse model data, a subgroup of HCC patients displayed a reduced amount of muscle and fat tissue (Table 1, Fig. 4.23). This result strongly suggests that loss of visceral fat happens in a subgroup of HCC patients. However, this body composition analysis includes only one-time point measurements, and to prove cachexia development convincingly, longitudinal patient studies, i.e. analyzing the same patient at different stages of disease progression should be performed. Thus far, fat tissue loss in HCC has only been reported by one Japanese group using a large patient cohort. In this study, the majority of the patients did not show visceral adiposity (exhibiting low level of adipose tissue), even though visceral adiposity predicted mortality in patients with HCC [186]. This study is the second study showing fat loss in a subgroup of HCC patients, referring to ASV-B model as well, although future studies should be performed with larger patient cohorts to address the functional importance of adipose tissue loss for the clinical course of HCC.

6. Conclusion

Collectively, the data presented in this thesis clearly demonstrate cachexia in the ASV-B model of HCC. This suggests the applicability of the ASV-B mouse model not only for investigating HCC, but also the pathogenesis of cancer-induced cachexia. In terms of cachexia, fat loss was remarkable in this model and was further investigated in this thesis. At the molecular level, increased lipolysis and browning of adipose tissue were shown as the main underlying mechanisms. Furthermore, *Hif1a* deficiency in myeloid cells caused reduced systemic inflammation but enhanced fat loss, arguing against a general role of inflammation as a driving force of cachexia. This unexpected result provided the basis to address another cachexia-inducing mechanism, hypothalamic activation. Indeed, increased hypothalamic activation was detected in tumor-bearing mice together with elevated systemic inflammation, pointing towards a functional relevance of the inflammation-brain-cachexia axis.

As a consequence of the myeloid cell-mediated inflammation defect, decreased macrophage accumulation in adipose tissue of ASV-B mice was detected, suggesting a role of *Hif1a* for migration and tissue infiltration of macrophages. Moreover, this result implies that local macrophages are protective against cancer cachexia-induced fat loss, providing another layer of complexity in the regulation of cachexia.

Overall, this thesis for the first time displays the macrophage-based regulation of adipose tissue loss in cancer cachexia. This phenomenon deserves to be analyzed further to better understand the pathogenesis of cachexia. Given that macrophage infiltration into adipose tissue is decreased upon *Hif1a* deletion, it would be interesting to assess the response of macrophages towards free fatty acids for migration and signaling pathways. Moreover, it would be of interest to investigate if myeloid cell-specific *Hif1a* deletion also affects adipose tissue macrophages in other animal models of cancer cachexia, to see whether this is a cancer type-specific observation. As adipose tissue is the largest energy reserve in the body, changes in adipose tissue mass and metabolism can have enormous impact on whole body energy balance. For this reason, the energy expenditure of ASV-B mice should be determined to better understand the metabolic changes in this model. Last but not least, a comprehensive patient study with a larger cohort of HCC patients addressing food intake, body composition change and general follow-up patients for energy balance would strengthen the suspected clinical relevance of HCC-induced cachexia.

7. References

[1] I.M. Arias, H.J. Alter, The liver : biology and pathobiology, 5th ed., John Wiley & Sons, Chichester, West Sussex, UK ; Hoboken, NJ, 2009.

[2] K. Si-Tayeb, F.P. Lemaigre, S.A. Duncan, Organogenesis and development of the liver, Dev Cell 18(2) (2010) 175-89.

[3] X. Mu, R. Espanol-Suner, I. Mederacke, S. Affo, R. Manco, C. Sempoux, F.P. Lemaigre, A. Adili, D. Yuan, A. Weber, K. Unger, M. Heikenwalder, I.A. Leclercq, R.F. Schwabe, Hepatocellular carcinoma originates from hepatocytes and not from the progenitor/biliary compartment, J Clin Invest 125(10) (2015) 3891-903.

[4] K.S. Tummala, M. Brandt, A. Teijeiro, O. Grana, R.F. Schwabe, C. Perna, N. Djouder, Hepatocellular Carcinomas Originate Predominantly from Hepatocytes and Benign Lesions from Hepatic Progenitor Cells, Cell Rep 19(3) (2017) 584-600.

[5] J. Ferlay, I. Soerjomataram, R. Dikshit, S. Eser, C. Mathers, M. Rebelo, D.M. Parkin, D. Forman, F. Bray, Cancer incidence and mortality worldwide: sources, methods and major patterns in GLOBOCAN 2012, Int J Cancer 136(5) (2015) E359-86.

[6] Y. Liu, F. Wu, Global burden of aflatoxin-induced hepatocellular carcinoma: a risk assessment, Environ Health Perspect 118(6) (2010) 818-24.

[7] H.B. El-Serag, Hepatocellular carcinoma, N Engl J Med 365(12) (2011) 1118-27.

[8] C. de Martel, D. Maucort-Boulch, M. Plummer, S. Franceschi, World-wide relative contribution of hepatitis B and C viruses in hepatocellular carcinoma, Hepatology 62(4) (2015) 1190-200.

[9] S. Mittal, Y.H. Sada, H.B. El-Serag, F. Kanwal, Z. Duan, S. Temple, S.B. May, J.R. Kramer, P.A. Richardson, J.A. Davila, Temporal trends of nonalcoholic fatty liver disease-related hepatocellular carcinoma in the veteran affairs population, Clin Gastroenterol Hepatol 13(3) (2015) 594-601 e1.

[10] T.M. Block, A.S. Mehta, C.J. Fimmel, R. Jordan, Molecular viral oncology of hepatocellular carcinoma, Oncogene 22(33) (2003) 5093-107.

[11] S. Badvie, Hepatocellular carcinoma, Postgrad Med J 76(891) (2000) 4-11.

[12] F. Trevisani, M. Frigerio, V. Santi, A. Grignaschi, M. Bernardi, Hepatocellular carcinoma in non-cirrhotic liver: a reappraisal, Dig Liver Dis 42(5) (2010) 341-7.

[13] P.A. Farazi, R.A. DePinho, Hepatocellular carcinoma pathogenesis: from genes to environment, Nat Rev Cancer 6(9) (2006) 674-87.

[14] A. Villanueva, P. Newell, D.Y. Chiang, S.L. Friedman, J.M. Llovet, Genomics and signaling pathways in hepatocellular carcinoma, Semin Liver Dis 27(1) (2007) 55-76.

[15] F. Sahin, R. Kannangai, O. Adegbola, J. Wang, G. Su, M. Torbenson, mTOR and P70 S6 kinase expression in primary liver neoplasms, Clin Cancer Res 10(24) (2004) 8421-5.

[16] P.A. Farazi, J. Glickman, J. Horner, R.A. Depinho, Cooperative interactions of p53 mutation, telomere dysfunction, and chronic liver damage in hepatocellular carcinoma progression, Cancer Res 66(9) (2006) 4766-73.

[17] J. Bruix, M. Sherman, D. American Association for the Study of Liver, Management of hepatocellular carcinoma: an update, Hepatology 53(3) (2011) 1020-2.

[18] L. European Association For The Study Of The, R. European Organisation For, C. Treatment Of, EASL-EORTC clinical practice guidelines: management of hepatocellular carcinoma, J Hepatol 56(4) (2012) 908-43.
[19] J.M. Llovet, J. Bruix, Systematic review of randomized trials for unresectable hepatocellular carcinoma: Chemoembolization improves survival, Hepatology 37(2) (2003) 429-42.
[20] A.L. Cheng, Y.K. Kang, Z. Chen, C.J. Tsao, S. Qin, J.S. Kim, R. Luo, J. Feng, S. Ye, T.S. Yang, J. Xu, Y. Sun, H. Liang, J. Liu, J. Wang, W.Y. Tak, H. Pan, K. Burock, J. Zou, D. Voliotis, Z. Guan, Efficacy and safety of sorafenib in patients in the Asia-Pacific region with advanced hepatocellular carcinoma: a phase III randomised, double-blind, placebo-controlled trial, Lancet Oncol 10(1) (2009) 25-34.
[21] J.M. Llovet, A.M. Di Bisceglie, J. Bruix, B.S. Kramer, R. Lencioni, A.X. Zhu, M. Sherman, M. Schwartz, M. Lotze, J. Talwalkar, G.J. Gores, H.C.C.D.C.T. Panel of Experts in, Design and endpoints of clinical trials in hepatocellular carcinoma, J Natl Cancer Inst 100(10) (2008) 698-711.
[22] J.M. Llovet, C. Bru, J. Bruix, Prognosis of hepatocellular carcinoma: the BCLC staging classification, Semin Liver Dis 19(3) (1999) 329-38.
[23] A. Forner, J.M. Llovet, J. Bruix, Hepatocellular carcinoma, Lancet 379(9822) (2012) 1245-55.
[24] M.J. Delano, L.L. Moldawer, The origins of cachexia in acute and chronic inflammatory diseases, Nutr Clin Pract 21(1) (2006) 68-81.
[25] A.M. Katz, P.B. Katz, Diseases of the heart in the works of Hippocrates, Br Heart J 24 (1962) 257-64.
[26] K. Fearon, F. Strasser, S.D. Anker, I. Bosaeus, E. Bruera, R.L. Fainsinger, A. Jatoi, C. Loprinzi, N. MacDonald, G. Mantovani, M. Davis, M. Muscaritoli, F. Ottery, L. Radbruch, P. Ravasco, D. Walsh, A. Wilcock, S. Kaasa, V.E. Baracos, Definition and classification of cancer cachexia: an international consensus, Lancet Oncol 12(5) (2011) 489-95.
[27] T. Yoshida, P. Delafontaine, Mechanisms of Cachexia in Chronic Disease States, Am J Med Sci 350(4) (2015) 250-6.
[28] S. Dodson, V.E. Baracos, A. Jatoi, W.J. Evans, D. Cella, J.T. Dalton, M.S. Steiner, Muscle wasting in cancer cachexia: clinical implications, diagnosis, and emerging treatment strategies, Annu Rev Med 62 (2011) 265-79.
[29] S.C. Teunissen, W. Wesker, C. Kruitwagen, H.C. de Haes, E.E. Voest, A. de Graeff, Symptom prevalence in patients with incurable cancer: a systematic review, J Pain Symptom Manage 34(1) (2007) 94-104.
[30] W.D. Dewys, C. Begg, P.T. Lavin, P.R. Band, J.M. Bennett, J.R. Bertino, M.H. Cohen, H.O. Douglass, Jr., P.F. Engstrom, E.Z. Ezdinli, J. Horton, G.J. Johnson, C.G. Moertel, M.M. Oken, C. Perlia, C. Rosenbaum, M.N. Silverstein, R.T. Skeel, R.W. Sponzo, D.C. Tormey, Prognostic effect of weight loss prior to chemotherapy in cancer patients. Eastern Cooperative Oncology Group, Am J Med 69(4) (1980) 491-7.
[31] M. Tsoli, G. Robertson, Cancer cachexia: malignant inflammation, tumorkines, and metabolic mayhem, Trends Endocrinol Metab 24(4) (2013) 174-83.
[32] J.M. Argiles, S. Busquets, B. Stemmler, F.J. Lopez-Soriano, Cancer cachexia: understanding the molecular basis, Nat Rev Cancer 14(11) (2014) 754-62.

[33] W.J. Evans, J.E. Morley, J. Argiles, C. Bales, V. Baracos, D. Guttridge, A. Jatoi, K. Kalantar-Zadeh, H. Lochs, G. Mantovani, D. Marks, W.E. Mitch, M. Muscaritoli, A. Najand, P. Ponikowski, F. Rossi Fanelli, M. Schambelan, A. Schols, M. Schuster, D. Thomas, R. Wolfe, S.D. Anker, Cachexia: a new definition, Clin Nutr 27(6) (2008) 793-9.

[34] J. Khal, A.V. Hine, K.C. Fearon, C.H. Dejong, M.J. Tisdale, Increased expression of proteasome subunits in skeletal muscle of cancer patients with weight loss, Int J Biochem Cell Biol 37(10) (2005) 2196-206.

[35] A. Bosutti, G. Toigo, B. Ciocchi, R. Situlin, G. Guarnieri, G. Biolo, Regulation of muscle cathepsin B proteolytic activity in protein-depleted patients with chronic diseases, Clin Nutr 21(5) (2002) 373-8.

[36] S. Busquets, C. Garcia-Martinez, B. Alvarez, N. Carbo, F.J. Lopez-Soriano, J.M. Argiles, Calpain-3 gene expression is decreased during experimental cancer cachexia, Biochim Biophys Acta 1475(1) (2000) 5-9.

[37] C. Bing, P. Trayhurn, Regulation of adipose tissue metabolism in cancer cachexia, Curr Opin Clin Nutr Metab Care 11(3) (2008) 201-7.

[38] S.T. Russell, M.J. Tisdale, Effect of a tumour-derived lipid-mobilising factor on glucose and lipid metabolism in vivo, Br J Cancer 87(5) (2002) 580-4.

[39] A. Hyltander, C. Drott, U. Korner, R. Sandstrom, K. Lundholm, Elevated energy expenditure in cancer patients with solid tumours, Eur J Cancer 27(1) (1991) 9-15.

[40] A. Hyltander, U. Korner, K.G. Lundholm, Evaluation of mechanisms behind elevated energy expenditure in cancer patients with solid tumours, Eur J Clin Invest 23(1) (1993) 46-52.

[41] D.D. Taylor, C. Gercel-Taylor, L.G. Jenis, D.F. Devereux, Identification of a human tumor-derived lipolysis-promoting factor, Cancer Res 52(4) (1992) 829-34.

[42] P.T. Todorov, W.N. Field, M.J. Tisdale, Role of a proteolysis-inducing factor (PIF) in cachexia induced by a human melanoma (G361), Br J Cancer 80(11) (1999) 1734-7.

[43] S.T. Russell, K. Hirai, M.J. Tisdale, Role of beta3-adrenergic receptors in the action of a tumour lipid mobilizing factor, Br J Cancer 86(3) (2002) 424-8.

[44] C.L. Monitto, S.M. Dong, J. Jen, D. Sidransky, Characterization of a human homologue of proteolysis-inducing factor and its role in cancer cachexia, Clin Cancer Res 10(17) (2004) 5862-9.

[45] C. Deans, S. Wigmore, S. Paterson-Brown, J. Black, J. Ross, K.C. Fearon, Serum parathyroid hormone-related peptide is associated with systemic inflammation and adverse prognosis in gastroesophageal carcinoma, Cancer 103(9) (2005) 1810-8.

[46] S. Kir, J.P. White, S. Kleiner, L. Kazak, P. Cohen, V.E. Baracos, B.M. Spiegelman, Tumour-derived PTH-related protein triggers adipose tissue browning and cancer cachexia, Nature 513(7516) (2014) 100-4.

[47] K.C. Fearon, D.J. Glass, D.C. Guttridge, Cancer cachexia: mediators, signaling, and metabolic pathways, Cell Metab 16(2) (2012) 153-66.

[48] C. Deans, S.J. Wigmore, Systemic inflammation, cachexia and prognosis in patients with cancer, Curr Opin Clin Nutr Metab Care 8(3) (2005) 265-9.

[49] J. Gelin, L.L. Moldawer, C. Lonnroth, B. Sherry, R. Chizzonite, K. Lundholm, Role of endogenous tumor necrosis factor alpha and interleukin 1 for experimental tumor growth and the development of cancer cachexia, Cancer Res 51(1) (1991) 415-21.

[50] G. Strassmann, M. Fong, J.S. Kenney, C.O. Jacob, Evidence for the involvement of interleukin 6 in experimental cancer cachexia, J Clin Invest 89(5) (1992) 1681-4.

[51] P. Matthys, H. Heremans, G. Opdenakker, A. Billiau, Anti-interferon-gamma antibody treatment, growth of Lewis lung tumours in mice and tumour-associated cachexia, Eur J Cancer 27(2) (1991) 182-7.

[52] L.L. Moldawer, M.A. Rogy, S.F. Lowry, The role of cytokines in cancer cachexia, JPEN J Parenter Enteral Nutr 16(6 Suppl) (1992) 43S-49S.

[53] P. Matthys, A. Billiau, Cytokines and cachexia, Nutrition 13(9) (1997) 763-70.

[54] H. Suzuki, A. Asakawa, H. Amitani, N. Nakamura, A. Inui, Cancer cachexia--pathophysiology and management, J Gastroenterol 48(5) (2013) 574-94.

[55] M.G. O'Riordain, J.S. Falconer, J. Maingay, K.C. Fearon, J.A. Ross, Peripheral blood cells from weight-losing cancer patients control the hepatic acute phase response by a primarily interleukin-6 dependent mechanism, Int J Oncol 15(4) (1999) 823-7.

[56] D.A. Deans, S.J. Wigmore, H. Gilmour, S. Paterson-Brown, J.A. Ross, K.C. Fearon, Elevated tumour interleukin-1beta is associated with systemic inflammation: A marker of reduced survival in gastro-oesophageal cancer, Br J Cancer 95(11) (2006) 1568-75.

[57] M.D. Barber, K.C. Fearon, J.A. Ross, Relationship of serum levels of interleukin-6, soluble interleukin-6 receptor and tumour necrosis factor receptors to the acute-phase protein response in advanced pancreatic cancer, Clin Sci (Lond) 96(1) (1999) 83-7.

[58] V.E. Baracos, Management of muscle wasting in cancer-associated cachexia: understanding gained from experimental studies, Cancer 92(6 Suppl) (2001) 1669-77.

[59] M.J. Tisdale, Mechanisms of cancer cachexia, Physiol Rev 89(2) (2009) 381-410.

[60] A. Bonetto, T. Aydogdu, X. Jin, Z. Zhang, R. Zhan, L. Puzis, L.G. Koniaris, T.A. Zimmers, JAK/STAT3 pathway inhibition blocks skeletal muscle wasting downstream of IL-6 and in experimental cancer cachexia, Am J Physiol Endocrinol Metab 303(3) (2012) E410-21.

[61] J.M. Argiles, M. Orpi, S. Busquets, F.J. Lopez-Soriano, Myostatin: more than just a regulator of muscle mass, Drug Discov Today 17(13-14) (2012) 702-9.

[62] C. Rommel, S.C. Bodine, B.A. Clarke, R. Rossman, L. Nunez, T.N. Stitt, G.D. Yancopoulos, D.J. Glass, Mediation of IGF-1-induced skeletal myotube hypertrophy by PI(3)K/Akt/mTOR and PI(3)K/Akt/GSK3 pathways, Nat Cell Biol 3(11) (2001) 1009-13.

[63] H. Ogiwara, S. Takahashi, Y. Kato, I. Uyama, T. Takahara, K. Kikuchi, S. Iida, Diminished visceral adipose tissue in cancer cachexia, J Surg Oncol 57(2) (1994) 129-33.

[64] K.C. Fearon, T. Preston, Body composition in cancer cachexia, Infusionstherapie 17 Suppl 3 (1990) 63-6.

[65] R.A. Murphy, M.S. Wilke, M. Perrine, M. Pawlowicz, M. Mourtzakis, J.R. Lieffers, M. Maneshgar, E. Bruera, M.T. Clandinin, V.E. Baracos, V.C. Mazurak, Loss of adipose tissue and plasma phospholipids: relationship to survival in advanced cancer patients, Clin Nutr 29(4) (2010) 482-7.

[66] C. Bing, S. Russell, E. Becket, M. Pope, M.J. Tisdale, P. Trayhurn, J.R. Jenkins, Adipose atrophy in cancer cachexia: morphologic and molecular analysis of adipose tissue in tumour-bearing mice, Br J Cancer 95(8) (2006) 1028-37.
[67] T. Mracek, N.A. Stephens, D. Gao, Y. Bao, J.A. Ross, M. Ryden, P. Arner, P. Trayhurn, K.C. Fearon, C. Bing, Enhanced ZAG production by subcutaneous adipose tissue is linked to weight loss in gastrointestinal cancer patients, Br J Cancer 104(3) (2011) 441-7.
[68] I. Dahlman, N. Mejhert, K. Linder, T. Agustsson, D.M. Mutch, A. Kulyte, B. Isaksson, J. Permert, N. Petrovic, J. Nedergaard, E. Sjolin, D. Brodin, K. Clement, K. Dahlman-Wright, M. Ryden, P. Arner, Adipose tissue pathways involved in weight loss of cancer cachexia, Br J Cancer 102(10) (2010) 1541-8.
[69] S.D. Zuijdgeest-van Leeuwen, J.W. van den Berg, J.L. Wattimena, A. van der Gaast, G.R. Swart, J.H. Wilson, P.C. Dagnelie, Lipolysis and lipid oxidation in weight-losing cancer patients and healthy subjects, Metabolism 49(7) (2000) 931-6.
[70] M. Ryden, T. Agustsson, J. Laurencikiene, T. Britton, E. Sjolin, B. Isaksson, J. Permert, P. Arner, Lipolysis--not inflammation, cell death, or lipogenesis--is involved in adipose tissue loss in cancer cachexia, Cancer 113(7) (2008) 1695-704.
[71] M. Ebadi, V.C. Mazurak, Evidence and mechanisms of fat depletion in cancer, Nutrients 6(11) (2014) 5280-97.
[72] T. Agustsson, M. Ryden, J. Hoffstedt, V. van Harmelen, A. Dicker, J. Laurencikiene, B. Isaksson, J. Permert, P. Arner, Mechanism of increased lipolysis in cancer cachexia, Cancer Res 67(11) (2007) 5531-7.
[73] D.X. Cao, G.H. Wu, Z.A. Yang, B. Zhang, Y. Jiang, Y.S. Han, G.D. He, Q.L. Zhuang, Y.F. Wang, Z.L. Huang, Q.L. Xi, Role of beta1-adrenoceptor in increased lipolysis in cancer cachexia, Cancer Sci 101(7) (2010) 1639-45.
[74] S.K. Das, S. Eder, S. Schauer, C. Diwoky, H. Temmel, B. Guertl, G. Gorkiewicz, K.P. Tamilarasan, P. Kumari, M. Trauner, R. Zimmermann, P. Vesely, G. Haemmerle, R. Zechner, G. Hoefler, Adipose triglyceride lipase contributes to cancer-associated cachexia, Science 333(6039) (2011) 233-8.
[75] R.E. Duncan, M. Ahmadian, K. Jaworski, E. Sarkadi-Nagy, H.S. Sul, Regulation of lipolysis in adipocytes, Annu Rev Nutr 27 (2007) 79-101.
[76] M. Ryden, P. Arner, Fat loss in cachexia--is there a role for adipocyte lipolysis?, Clin Nutr 26(1) (2007) 1-6.
[77] R.W. Grant, J.M. Stephens, Fat in flames: influence of cytokines and pattern recognition receptors on adipocyte lipolysis, Am J Physiol Endocrinol Metab 309(3) (2015) E205-13.
[78] K.R. Feingold, W. Doerrler, C.A. Dinarello, W. Fiers, C. Grunfeld, Stimulation of lipolysis in cultured fat cells by tumor necrosis factor, interleukin-1, and the interferons is blocked by inhibition of prostaglandin synthesis, Endocrinology 130(1) (1992) 10-6.
[79] J.N. Gordon, S.R. Green, P.M. Goggin, Cancer cachexia, QJM 98(11) (2005) 779-88.
[80] M. Petruzzelli, M. Schweiger, R. Schreiber, R. Campos-Olivas, M. Tsoli, J. Allen, M. Swarbrick, S. Rose-John, M. Rincon, G. Robertson, R. Zechner, E.F. Wagner, A switch from white to brown fat increases energy expenditure in cancer-associated cachexia, Cell Metab 20(3) (2014) 433-47.

[81] T. Yoshikawa, Y. Noguchi, C. Doi, T. Makino, T. Okamoto, A. Matsumoto, Insulin resistance was connected with the alterations of substrate utilization in patients with cancer, Cancer Lett 141(1-2) (1999) 93-8.
[82] M.R. Teli, O.F. James, A.D. Burt, M.K. Bennett, C.P. Day, The natural history of nonalcoholic fatty liver: a follow-up study, Hepatology 22(6) (1995) 1714-9.
[83] M. Berriel Diaz, A. Krones-Herzig, D. Metzger, A. Ziegler, A. Vegiopoulos, M. Klingenspor, K. Muller-Decker, S. Herzig, Nuclear receptor cofactor receptor interacting protein 140 controls hepatic triglyceride metabolism during wasting in mice, Hepatology 48(3) (2008) 782-91.
[84] M. Olivan, J. Springer, S. Busquets, A. Tschirner, M. Figueras, M. Toledo, C. Fontes-Oliveira, M.I. Genovese, P. Ventura da Silva, A. Sette, F.J. Lopez-Soriano, S. Anker, J.M. Argiles, Theophylline is able to partially revert cachexia in tumour-bearing rats, Nutr Metab (Lond) 9(1) (2012) 76.
[85] X. Zhou, J.L. Wang, J. Lu, Y. Song, K.S. Kwak, Q. Jiao, R. Rosenfeld, Q. Chen, T. Boone, W.S. Simonet, D.L. Lacey, A.L. Goldberg, H.Q. Han, Reversal of cancer cachexia and muscle wasting by ActRIIB antagonism leads to prolonged survival, Cell 142(4) (2010) 531-43.
[86] M. Tian, Y. Nishijima, M.L. Asp, M.B. Stout, P.J. Reiser, M.A. Belury, Cardiac alterations in cancer-induced cachexia in mice, Int J Oncol 37(2) (2010) 347-53.
[87] K.C. Fearon, Cancer cachexia: developing multimodal therapy for a multidimensional problem, Eur J Cancer 44(8) (2008) 1124-32.
[88] C. Pietra, Y. Takeda, N. Tazawa-Ogata, M. Minami, X. Yuanfeng, E.M. Duus, R. Northrup, Anamorelin HCl (ONO-7643), a novel ghrelin receptor agonist, for the treatment of cancer anorexia-cachexia syndrome: preclinical profile, J Cachexia Sarcopenia Muscle 5(4) (2014) 329-37.
[89] M.D. DeBoer, X.X. Zhu, P. Levasseur, M.M. Meguid, S. Suzuki, A. Inui, J.E. Taylor, H.A. Halem, J.Z. Dong, R. Datta, M.D. Culler, D.L. Marks, Ghrelin treatment causes increased food intake and retention of lean body mass in a rat model of cancer cachexia, Endocrinology 148(6) (2007) 3004-12.
[90] B.E. Wisse, R.S. Frayo, M.W. Schwartz, D.E. Cummings, Reversal of cancer anorexia by blockade of central melanocortin receptors in rats, Endocrinology 142(8) (2001) 3292-301.
[91] S.J. Wigmore, M.D. Barber, J.A. Ross, M.J. Tisdale, K.C. Fearon, Effect of oral eicosapentaenoic acid on weight loss in patients with pancreatic cancer, Nutr Cancer 36(2) (2000) 177-84.
[92] S.J. Wigmore, K.C. Fearon, J.P. Maingay, J.A. Ross, Down-regulation of the acute-phase response in patients with pancreatic cancer cachexia receiving oral eicosapentaenoic acid is mediated via suppression of interleukin-6, Clin Sci (Lond) 92(2) (1997) 215-21.
[93] B. Wiedenmann, P. Malfertheiner, H. Friess, P. Ritch, J. Arseneau, G. Mantovani, F. Caprioni, E. Van Cutsem, D. Richel, M. DeWitte, M. Qi, D. Robinson, Jr., B. Zhong, C. De Boer, J.D. Lu, U. Prabhakar, R. Corringham, D. Von Hoff, A multicenter, phase II study of infliximab plus gemcitabine in pancreatic cancer cachexia, J Support Oncol 6(1) (2008) 18-25.
[94] A. Jatoi, H.L. Ritter, A. Dueck, P.L. Nguyen, D.A. Nikcevich, R.F. Luyun, B.I. Mattar, C.L. Loprinzi, A placebo-controlled, double-blind trial of infliximab for cancer-

associated weight loss in elderly and/or poor performance non-small cell lung cancer patients (N01C9), Lung Cancer 68(2) (2010) 234-9.

[95] Z.H. Khan, E.J. Simpson, A.T. Cole, M. Holt, I. MacDonald, D. Pye, A. Austin, J.G. Freeman, Oesophageal cancer and cachexia: the effect of short-term treatment with thalidomide on weight loss and lean body mass, Aliment Pharmacol Ther 17(5) (2003) 677-82.

[96] J.P. White, J.W. Baynes, S.L. Welle, M.C. Kostek, L.E. Matesic, S. Sato, J.A. Carson, The regulation of skeletal muscle protein turnover during the progression of cancer cachexia in the Apc(Min/+) mouse, PLoS One 6(9) (2011) e24650.

[97] K. Ando, F. Takahashi, M. Kato, N. Kaneko, T. Doi, Y. Ohe, F. Koizumi, K. Nishio, K. Takahashi, Tocilizumab, a proposed therapy for the cachexia of Interleukin6-expressing lung cancer, PLoS One 9(7) (2014) e102436.

[98] A.T. Ali, W.E. Hochfeld, R. Myburgh, M.S. Pepper, Adipocyte and adipogenesis, Eur J Cell Biol 92(6-7) (2013) 229-36.

[99] J.-P. Bastard, B. F©·ve, Physiology and physiopathology of adipose tissue, Springer,, Paris ; New York, 2013, p. 1 online resource.

[100] J. Aron-Wisnewsky, J. Tordjman, C. Poitou, F. Darakhshan, D. Hugol, A. Basdevant, A. Aissat, M. Guerre-Millo, K. Clement, Human adipose tissue macrophages: m1 and m2 cell surface markers in subcutaneous and omental depots and after weight loss, J Clin Endocrinol Metab 94(11) (2009) 4619-23.

[101] Y. Okamoto, H. Higashiyama, J.X. Rong, M.J. McVey, M. Kinoshita, S. Asano, M.K. Hansen, Comparison of mitochondrial and macrophage content between subcutaneous and visceral fat in db/db mice, Exp Mol Pathol 83(1) (2007) 73-83.

[102] I. Murano, G. Barbatelli, V. Parisani, C. Latini, G. Muzzonigro, M. Castellucci, S. Cinti, Dead adipocytes, detected as crown-like structures, are prevalent in visceral fat depots of genetically obese mice, J Lipid Res 49(7) (2008) 1562-8.

[103] C.N. Lumeng, S.M. Deyoung, J.L. Bodzin, A.R. Saltiel, Increased inflammatory properties of adipose tissue macrophages recruited during diet-induced obesity, Diabetes 56(1) (2007) 16-23.

[104] H. Xu, G.T. Barnes, Q. Yang, G. Tan, D. Yang, C.J. Chou, J. Sole, A. Nichols, J.S. Ross, L.A. Tartaglia, H. Chen, Chronic inflammation in fat plays a crucial role in the development of obesity-related insulin resistance, J Clin Invest 112(12) (2003) 1821-30.

[105] C.N. Lumeng, J.L. Bodzin, A.R. Saltiel, Obesity induces a phenotypic switch in adipose tissue macrophage polarization, J Clin Invest 117(1) (2007) 175-84.

[106] R. Cancello, C. Henegar, N. Viguerie, S. Taleb, C. Poitou, C. Rouault, M. Coupaye, V. Pelloux, D. Hugol, J.L. Bouillot, A. Bouloumie, G. Barbatelli, S. Cinti, P.A. Svensson, G.S. Barsh, J.D. Zucker, A. Basdevant, D. Langin, K. Clement, Reduction of macrophage infiltration and chemoattractant gene expression changes in white adipose tissue of morbidly obese subjects after surgery-induced weight loss, Diabetes 54(8) (2005) 2277-86.

[107] A. Kosteli, E. Sugaru, G. Haemmerle, J.F. Martin, J. Lei, R. Zechner, A.W. Ferrante, Jr., Weight loss and lipolysis promote a dynamic immune response in murine adipose tissue, J Clin Invest 120(10) (2010) 3466-79.

[108] V. Kumar, D.I. Gabrilovich, Hypoxia-inducible factors in regulation of immune responses in tumour microenvironment, Immunology 143(4) (2014) 512-9.

[109] G.L. Semenza, Hypoxia-inducible factors in physiology and medicine, Cell 148(3) (2012) 399-408.

[110] S.C. Lin, W.L. Liao, J.C. Lee, S.J. Tsai, Hypoxia-regulated gene network in drug resistance and cancer progression, Exp Biol Med (Maywood) 239(7) (2014) 779-792.

[111] G.L. Semenza, Targeting HIF-1 for cancer therapy, Nat Rev Cancer 3(10) (2003) 721-32.

[112] R. Tal, The role of hypoxia and hypoxia-inducible factor-1alpha in preeclampsia pathogenesis, Biol Reprod 87(6) (2012) 134.

[113] G.L. Semenza, Defining the role of hypoxia-inducible factor 1 in cancer biology and therapeutics, Oncogene 29(5) (2010) 625-34.

[114] C. Chen, T. Lou, Hypoxia inducible factors in hepatocellular carcinoma, Oncotarget 8(28) (2017) 46691-46703.

[115] C. Peyssonnaux, V. Datta, T. Cramer, A. Doedens, E.A. Theodorakis, R.L. Gallo, N. Hurtado-Ziola, V. Nizet, R.S. Johnson, HIF-1alpha expression regulates the bactericidal capacity of phagocytes, J Clin Invest 115(7) (2005) 1806-15.

[116] C.C. Blouin, E.L. Page, G.M. Soucy, D.E. Richard, Hypoxic gene activation by lipopolysaccharide in macrophages: implication of hypoxia-inducible factor 1alpha, Blood 103(3) (2004) 1124-30.

[117] J. Rius, M. Guma, C. Schachtrup, K. Akassoglou, A.S. Zinkernagel, V. Nizet, R.S. Johnson, G.G. Haddad, M. Karin, NF-kappaB links innate immunity to the hypoxic response through transcriptional regulation of HIF-1alpha, Nature 453(7196) (2008) 807-11.

[118] J.E. Albina, B. Mastrofrancesco, J.A. Vessella, C.A. Louis, W.L. Henry, Jr., J.S. Reichner, HIF-1 expression in healing wounds: HIF-1alpha induction in primary inflammatory cells by TNF-alpha, Am J Physiol Cell Physiol 281(6) (2001) C1971-7.

[119] T. Cramer, Y. Yamanishi, B.E. Clausen, I. Forster, R. Pawlinski, N. Mackman, V.H. Haase, R. Jaenisch, M. Corr, V. Nizet, G.S. Firestein, H.P. Gerber, N. Ferrara, R.S. Johnson, HIF-1alpha is essential for myeloid cell-mediated inflammation, Cell 112(5) (2003) 645-57.

[120] K.D. Nguyen, Y. Qiu, X. Cui, Y.P. Goh, J. Mwangi, T. David, L. Mukundan, F. Brombacher, R.M. Locksley, A. Chawla, Alternatively activated macrophages produce catecholamines to sustain adaptive thermogenesis, Nature 480(7375) (2011) 104-8.

[121] N. Dubois, M. Bennoun, I. Allemand, T. Molina, G. Grimber, M. Daudet-Monsac, R. Abelanet, P. Briand, Time-course development of differentiated hepatocarcinoma and lung metastasis in transgenic mice, J Hepatol 13(2) (1991) 227-39.

[122] M. Berge, P. Bonnin, E. Sulpice, J. Vilar, D. Allanic, J.S. Silvestre, B.I. Levy, G.C. Tucker, G. Tobelem, T. Merkulova-Rainon, Small interfering RNAs induce target-independent inhibition of tumor growth and vasculature remodeling in a mouse model of hepatocellular carcinoma, Am J Pathol 177(6) (2010) 3192-201.

[123] H.E. Ryan, M. Poloni, W. McNulty, D. Elson, M. Gassmann, J.M. Arbeit, R.S. Johnson, Hypoxia-inducible factor-1alpha is a positive factor in solid tumor growth, Cancer Res 60(15) (2000) 4010-5.

[124] P.C. Orban, D. Chui, J.D. Marth, Tissue- and site-specific DNA recombination in transgenic mice, Proc Natl Acad Sci U S A 89(15) (1992) 6861-5.

[125] C. Postic, M. Shiota, K.D. Niswender, T.L. Jetton, Y. Chen, J.M. Moates, K.D. Shelton, J. Lindner, A.D. Cherrington, M.A. Magnuson, Dual roles for glucokinase in

glucose homeostasis as determined by liver and pancreatic beta cell-specific gene knock-outs using Cre recombinase, J Biol Chem 274(1) (1999) 305-15.

[126] B.E. Clausen, C. Burkhardt, W. Reith, R. Renkawitz, I. Forster, Conditional gene targeting in macrophages and granulocytes using LysMcre mice, Transgenic Res 8(4) (1999) 265-77.

[127] F. Gremse, M. Stark, J. Ehling, J.R. Menzel, T. Lammers, F. Kiessling, Imalytics Preclinical: Interactive Analysis of Biomedical Volume Data, Theranostics 6(3) (2016) 328-41.

[128] M. Mourtzakis, C.M. Prado, J.R. Lieffers, T. Reiman, L.J. McCargar, V.E. Baracos, A practical and precise approach to quantification of body composition in cancer patients using computed tomography images acquired during routine care, Appl Physiol Nutr Metab 33(5) (2008) 997-1006.

[129] R. Ballaro, P. Costelli, F. Penna, Animal models for cancer cachexia, Curr Opin Support Palliat Care 10(4) (2016) 281-287.

[130] S.J. Hwang, J.C. Luo, C.P. Li, C.W. Chu, J.C. Wu, C.R. Lai, J.H. Chiang, G.Y. Chau, W.Y. Lui, C.C. Lee, F.Y. Chang, S.D. Lee, Thrombocytosis: a paraneoplastic syndrome in patients with hepatocellular carcinoma, World J Gastroenterol 10(17) (2004) 2472-7.

[131] J. Faber, P. Vos, D. Kegler, K. van Norren, J.M. Argiles, A. Laviano, J. Garssen, A. van Helvoort, Beneficial immune modulatory effects of a specific nutritional combination in a murine model for cancer cachexia, Br J Cancer 99(12) (2008) 2029-36.

[132] M. Lafontan, D. Langin, Lipolysis and lipid mobilization in human adipose tissue, Prog Lipid Res 48(5) (2009) 275-97.

[133] K. Fischer, H.H. Ruiz, K. Jhun, B. Finan, D.J. Oberlin, V. van der Heide, A.V. Kalinovich, N. Petrovic, Y. Wolf, C. Clemmensen, A.C. Shin, S. Divanovic, F. Brombacher, E. Glasmacher, S. Keipert, M. Jastroch, J. Nagler, K.W. Schramm, D. Medrikova, G. Collden, S.C. Woods, S. Herzig, D. Homann, S. Jung, J. Nedergaard, B. Cannon, M.H. Tschop, T.D. Muller, C. Buettner, Alternatively activated macrophages do not synthesize catecholamines or contribute to adipose tissue adaptive thermogenesis, Nat Med 23(5) (2017) 623-630.

[134] F.B. Kraemer, W.J. Shen, Hormone-sensitive lipase: control of intracellular tri-(di-)acylglycerol and cholesteryl ester hydrolysis, J Lipid Res 43(10) (2002) 1585-94.

[135] L.K. Heilbronn, L.V. Campbell, Adipose tissue macrophages, low grade inflammation and insulin resistance in human obesity, Curr Pharm Des 14(12) (2008) 1225-30.

[136] S.P. Weisberg, D. McCann, M. Desai, M. Rosenbaum, R.L. Leibel, A.W. Ferrante, Jr., Obesity is associated with macrophage accumulation in adipose tissue, J Clin Invest 112(12) (2003) 1796-808.

[137] J.M. Olefsky, C.K. Glass, Macrophages, inflammation, and insulin resistance, Annu Rev Physiol 72 (2010) 219-46.

[138] A. Takikawa, A. Mahmood, A. Nawaz, T. Kado, K. Okabe, S. Yamamoto, A. Aminuddin, S. Senda, K. Tsuneyama, M. Ikutani, Y. Watanabe, Y. Igarashi, Y. Nagai, K. Takatsu, K. Koizumi, J. Imura, N. Goda, M. Sasahara, M. Matsumoto, K. Saeki, T. Nakagawa, S. Fujisaka, I. Usui, K. Tobe, HIF-1alpha in Myeloid Cells Promotes

Adipose Tissue Remodeling Toward Insulin Resistance, Diabetes 65(12) (2016) 3649-3659.

[139] C.D. Camell, J. Sander, O. Spadaro, A. Lee, K.Y. Nguyen, A. Wing, E.L. Goldberg, Y.H. Youm, C.W. Brown, J. Elsworth, M.S. Rodeheffer, J.L. Schultze, V.D. Dixit, Inflammasome-driven catecholamine catabolism in macrophages blunts lipolysis during ageing, Nature 550(7674) (2017) 119-123.

[140] R.M. Pirzgalska, E. Seixas, J.S. Seidman, V.M. Link, N.M. Sanchez, I. Mahu, R. Mendes, V. Gres, N. Kubasova, I. Morris, B.A. Arus, C.M. Larabee, M. Vasques, F. Tortosa, A.L. Sousa, S. Anandan, E. Tranfield, M.K. Hahn, M. Iannacone, N.J. Spann, C.K. Glass, A.I. Domingos, Sympathetic neuron-associated macrophages contribute to obesity by importing and metabolizing norepinephrine, Nat Med 23(11) (2017) 1309-1318.

[141] R. Nogueiras, P. Wiedmer, D. Perez-Tilve, C. Veyrat-Durebex, J.M. Keogh, G.M. Sutton, P.T. Pfluger, T.R. Castaneda, S. Neschen, S.M. Hofmann, P.N. Howles, D.A. Morgan, S.C. Benoit, I. Szanto, B. Schrott, A. Schurmann, H.G. Joost, C. Hammond, D.Y. Hui, S.C. Woods, K. Rahmouni, A.A. Butler, I.S. Farooqi, S. O'Rahilly, F. Rohner-Jeanrenaud, M.H. Tschop, The central melanocortin system directly controls peripheral lipid metabolism, J Clin Invest 117(11) (2007) 3475-88.

[142] F. Barre-Sinoussi, X. Montagutelli, Animal models are essential to biological research: issues and perspectives, Future Sci OA 1(4) (2015) FSO63.

[143] K.V. Chang, J.D. Chen, W.T. Wu, K.C. Huang, C.T. Hsu, D.S. Han, Association between Loss of Skeletal Muscle Mass and Mortality and Tumor Recurrence in Hepatocellular Carcinoma: A Systematic Review and Meta-Analysis, Liver Cancer 7(1) (2018) 90-103.

[144] S. Levolger, M.G. van Vledder, R. Muslem, M. Koek, W.J. Niessen, R.A. de Man, R.W. de Bruin, J.N. Ijzermans, Sarcopenia impairs survival in patients with potentially curable hepatocellular carcinoma, J Surg Oncol 112(2) (2015) 208-13.

[145] S. Iritani, K. Imai, K. Takai, T. Hanai, T. Ideta, T. Miyazaki, A. Suetsugu, M. Shiraki, M. Shimizu, H. Moriwaki, Skeletal muscle depletion is an independent prognostic factor for hepatocellular carcinoma, J Gastroenterol 50(3) (2015) 323-32.

[146] O. Mir, R. Coriat, B. Blanchet, J.P. Durand, P. Boudou-Rouquette, J. Michels, S. Ropert, M. Vidal, S. Pol, S. Chaussade, F. Goldwasser, Sarcopenia predicts early dose-limiting toxicities and pharmacokinetics of sorafenib in patients with hepatocellular carcinoma, PLoS One 7(5) (2012) e37563.

[147] K. Fearon, J. Arends, V. Baracos, Understanding the mechanisms and treatment options in cancer cachexia, Nat Rev Clin Oncol 10(2) (2013) 90-9.

[148] E.E. Talbert, G.A. Metzger, W.A. He, D.C. Guttridge, Modeling human cancer cachexia in colon 26 tumor-bearing adult mice, J Cachexia Sarcopenia Muscle 5(4) (2014) 321-8.

[149] P. Aulino, E. Berardi, V.M. Cardillo, E. Rizzuto, B. Perniconi, C. Ramina, F. Padula, E.P. Spugnini, A. Baldi, F. Faiola, S. Adamo, D. Coletti, Molecular, cellular and physiological characterization of the cancer cachexia-inducing C26 colon carcinoma in mouse, BMC Cancer 10 (2010) 363.

[150] K.A. Michaelis, X. Zhu, K.G. Burfeind, S.M. Krasnow, P.R. Levasseur, T.K. Morgan, D.L. Marks, Establishment and characterization of a novel murine model of pancreatic cancer cachexia, J Cachexia Sarcopenia Muscle 8(5) (2017) 824-838.

[151] J.A. Chen, A. Splenser, B. Guillory, J. Luo, M. Mendiratta, B. Belinova, T. Halder, G. Zhang, Y.P. Li, J.M. Garcia, Ghrelin prevents tumour- and cisplatin-induced muscle wasting: characterization of multiple mechanisms involved, J Cachexia Sarcopenia Muscle 6(2) (2015) 132-43.
[152] M. Toledo, F. Penna, S. Busquets, F.J. Lopez-Soriano, J.M. Argiles, Distinct behaviour of sorafenib in experimental cachexia-inducing tumours: the role of STAT3, PLoS One 9(12) (2014) e113931.
[153] M.A. Honors, K.P. Kinzig, Characterization of the Yoshida sarcoma: a model of cancer cachexia, Support Care Cancer 21(10) (2013) 2687-94.
[154] A. Tschirner, S. von Haehling, S. Palus, W. Doehner, S.D. Anker, J. Springer, Ursodeoxycholic acid treatment in a rat model of cancer cachexia, J Cachexia Sarcopenia Muscle 3(1) (2012) 31-6.
[155] M. Toledo, F. Penna, F. Oliva, M. Luque, A. Betancourt, E. Marmonti, F.J. Lopez-Soriano, J.M. Argiles, S. Busquets, A multifactorial anti-cachectic approach for cancer cachexia in a rat model undergoing chemotherapy, J Cachexia Sarcopenia Muscle 7(1) (2016) 48-59.
[156] T. Yoshida, Contributions of the ascites hepatoma to the concept of malignancy of cancer, Ann N Y Acad Sci 63(5) (1956) 852-81.
[157] A. De Lerma Barbaro, The complex liaison between cachexia and tumor burden (Review), Oncol Rep 34(4) (2015) 1635-49.
[158] K. Daskalow, N. Rohwer, E. Raskopf, E. Dupuy, A. Kuhl, C. Loddenkemper, B. Wiedenmann, V. Schmitz, T. Cramer, Role of hypoxia-inducible transcription factor 1alpha for progression and chemosensitivity of murine hepatocellular carcinoma, J Mol Med (Berl) 88(8) (2010) 817-27.
[159] M.N. Metzinger, B. Miramontes, P. Zhou, Y. Liu, S. Chapman, L. Sun, T.A. Sasser, G.E. Duffield, M.S. Stack, W.M. Leevy, Correlation of X-ray computed tomography with quantitative nuclear magnetic resonance methods for pre-clinical measurement of adipose and lean tissues in living mice, Sensors (Basel) 14(10) (2014) 18526-42.
[160] N. Caronni, B. Savino, R. Bonecchi, Myeloid cells in cancer-related inflammation, Immunobiology 220(2) (2015) 249-53.
[161] C. Bing, P. Trayhurn, New insights into adipose tissue atrophy in cancer cachexia, Proc Nutr Soc 68(4) (2009) 385-92.
[162] N. Carbo, P. Costelli, L. Tessitore, G.J. Bagby, F.J. Lopez-Soriano, F.M. Baccino, J.M. Argiles, Anti-tumour necrosis factor-alpha treatment interferes with changes in lipid metabolism in a tumour cachexia model, Clin Sci (Lond) 87(3) (1994) 349-55.
[163] A. Vegiopoulos, M. Rohm, S. Herzig, Adipose tissue: between the extremes, EMBO J 36(14) (2017) 1999-2017.
[164] M.P. Thompson, S.T. Cooper, B.R. Parry, J.A. Tuckey, Increased expression of the mRNA for hormone-sensitive lipase in adipose tissue of cancer patients, Biochim Biophys Acta 1180(3) (1993) 236-42.
[165] P. Arner, D. Langin, Lipolysis in lipid turnover, cancer cachexia, and obesity-induced insulin resistance, Trends Endocrinol Metab 25(5) (2014) 255-62.
[166] J.H. Shin, S.H. Lee, Y.N. Kim, I.Y. Kim, Y.J. Kim, D.S. Kyeong, H.J. Lim, S.Y. Cho, J. Choi, Y.J. Wi, J.H. Choi, Y.S. Yoon, Y.S. Bae, J.K. Seong, AHNAK deficiency

promotes browning and lipolysis in mice via increased responsiveness to beta-adrenergic signalling, Sci Rep 6 (2016) 23426.

[167] C.A. Guo, S. Kogan, S.U. Amano, M. Wang, S. Dagdeviren, R.H. Friedline, M. Aouadi, J.K. Kim, M.P. Czech, CD40 deficiency in mice exacerbates obesity-induced adipose tissue inflammation, hepatic steatosis, and insulin resistance, Am J Physiol Endocrinol Metab 304(9) (2013) E951-63.

[168] C.N. Lumeng, J.B. DelProposto, D.J. Westcott, A.R. Saltiel, Phenotypic switching of adipose tissue macrophages with obesity is generated by spatiotemporal differences in macrophage subtypes, Diabetes 57(12) (2008) 3239-46.

[169] M.L. Batista, Jr., F.S. Henriques, R.X. Neves, M.R. Olivan, E.M. Matos-Neto, P.S. Alcantara, L.F. Maximiano, J.P. Otoch, M.J. Alves, M. Seelaender, Cachexia-associated adipose tissue morphological rearrangement in gastrointestinal cancer patients, J Cachexia Sarcopenia Muscle 7(1) (2016) 37-47.

[170] L.E. Crotty Alexander, K. Akong-Moore, S. Feldstein, P. Johansson, A. Nguyen, E.K. McEachern, S. Nicatia, A.S. Cowburn, J. Olson, J.Y. Cho, H. Isaacs, Jr., R.S. Johnson, D.H. Broide, V. Nizet, Myeloid cell HIF-1alpha regulates asthma airway resistance and eosinophil function, J Mol Med (Berl) 91(5) (2013) 637-44.

[171] H. Ohira, Y. Fujioka, C. Katagiri, R. Mamoto, M. Aoyama-Ishikawa, K. Amako, Y. Izumi, S. Nishiumi, M. Yoshida, M. Usami, M. Ikeda, Butyrate attenuates inflammation and lipolysis generated by the interaction of adipocytes and macrophages, J Atheroscler Thromb 20(5) (2013) 425-42.

[172] F. Dong, M. Khalil, M. Kiedrowski, C. O'Connor, E. Petrovic, X. Zhou, M.S. Penn, Critical role for leukocyte hypoxia inducible factor-1alpha expression in post-myocardial infarction left ventricular remodeling, Circ Res 106(3) (2010) 601-10.

[173] S. Frede, C. Stockmann, P. Freitag, J. Fandrey, Bacterial lipopolysaccharide induces HIF-1 activation in human monocytes via p44/42 MAPK and NF-kappaB, Biochem J 396(3) (2006) 517-27.

[174] H. Shi, M.V. Kokoeva, K. Inouye, I. Tzameli, H. Yin, J.S. Flier, TLR4 links innate immunity and fatty acid-induced insulin resistance, J Clin Invest 116(11) (2006) 3015-25.

[175] S.U. Amano, J.L. Cohen, P. Vangala, M. Tencerova, S.M. Nicoloro, J.C. Yawe, Y. Shen, M.P. Czech, M. Aouadi, Local proliferation of macrophages contributes to obesity-associated adipose tissue inflammation, Cell Metab 19(1) (2014) 162-171.

[176] M. Metheni, A. Lombes, F. Bouillaud, F. Batteux, G. Langsley, HIF-1alpha induction, proliferation and glycolysis of Theileria-infected leukocytes, Cell Microbiol 17(4) (2015) 467-72.

[177] M.J. Kraakman, A.J. Murphy, K. Jandeleit-Dahm, H.L. Kammoun, Macrophage polarization in obesity and type 2 diabetes: weighing down our understanding of macrophage function?, Front Immunol 5 (2014) 470.

[178] N. Takeda, E.L. O'Dea, A. Doedens, J.W. Kim, A. Weidemann, C. Stockmann, M. Asagiri, M.C. Simon, A. Hoffmann, R.S. Johnson, Differential activation and antagonistic function of HIF-{alpha} isoforms in macrophages are essential for NO homeostasis, Genes Dev 24(5) (2010) 491-501.

[179] J.W. Sohn, Network of hypothalamic neurons that control appetite, BMB Rep 48(4) (2015) 229-33.

[180] A.J. Grossberg, J.M. Scarlett, D.L. Marks, Hypothalamic mechanisms in cachexia, Physiol Behav 100(5) (2010) 478-89.

[181] N. Balthasar, R. Coppari, J. McMinn, S.M. Liu, C.E. Lee, V. Tang, C.D. Kenny, R.A. McGovern, S.C. Chua, Jr., J.K. Elmquist, B.B. Lowell, Leptin receptor signaling in POMC neurons is required for normal body weight homeostasis, Neuron 42(6) (2004) 983-91.

[182] E.D. Berglund, C.R. Vianna, J. Donato, Jr., M.H. Kim, J.C. Chuang, C.E. Lee, D.A. Lauzon, P. Lin, L.J. Brule, M.M. Scott, R. Coppari, J.K. Elmquist, Direct leptin action on POMC neurons regulates glucose homeostasis and hepatic insulin sensitivity in mice, J Clin Invest 122(3) (2012) 1000-9.

[183] J.J. Geerling, M.R. Boon, S. Kooijman, E.T. Parlevliet, L.M. Havekes, J.A. Romijn, I.M. Meurs, P.C. Rensen, Sympathetic nervous system control of triglyceride metabolism: novel concepts derived from recent studies, J Lipid Res 55(2) (2014) 180-9.

[184] M. Bamshad, V.T. Aoki, M.G. Adkison, W.S. Warren, T.J. Bartness, Central nervous system origins of the sympathetic nervous system outflow to white adipose tissue, Am J Physiol 275(1 Pt 2) (1998) R291-9.

[185] C. Dodt, P. Lonnroth, J.P. Wellhoner, H.L. Fehm, M. Elam, Sympathetic control of white adipose tissue in lean and obese humans, Acta Physiol Scand 177(3) (2003) 351-7.

[186] N. Fujiwara, H. Nakagawa, Y. Kudo, R. Tateishi, M. Taguri, T. Watadani, R. Nakagomi, M. Kondo, T. Nakatsuka, T. Minami, M. Sato, K. Uchino, K. Enooku, Y. Kondo, Y. Asaoka, Y. Tanaka, K. Ohtomo, S. Shiina, K. Koike, Sarcopenia, intramuscular fat deposition, and visceral adiposity independently predict the outcomes of hepatocellular carcinoma, J Hepatol 63(1) (2015) 131-40.

Declaration

I hereby declare that I wrote this thesis myself and used only the sources that have been specified. All the work reported was performed by myself except contributions to the research made by the others which is explicitly acknowledged in the thesis. Parts of this work were published before in:

Erdem M, Möckel D, Jumpertz S, John C, Fragoulis A, Rudolph I, Wulfmeier J, Springer J, Horn H, Koch M, Lurje G, Lammers T, van der Kroft G, Gremse G, Cramer T. Macrophages protect against loss of adipose tissue during cancer cachexia (J Cachexia Sarcopenia Muscle 2019 Jul 18. doi: 10.1002/jcsm.12450).

Some figures and text can be identical in this thesis and published article.

Erklärung

Ich erkläre eidesstattlich, dass ich die vorliegende Dissertation selbstständig verfasst und nur die angegebenen Quellen und Hilfsmittel verwendet habe. Alle Arbeiten, über die berichtet wurde, wurden von mir selbst ausgeführt, mit Ausnahme der Beiträge der anderen, die in der Dissertation ausdrücklich erwähnt werden. Teile dieser Arbeit wurden bereits veröffentlicht in:

Erdem M, Möckel D, Jumpertz S, John C, Fragoulis A, Rudolph I, Wulfmeier J, Springer J, Horn H, Koch M, Lurje G, Lammers T, van der Kroft G, Gremse G, Cramer T. Macrophages protect against loss of adipose tissue during cancer cachexia (J Cachexia Sarcopenia Muscle 2019 Jul 18. doi: 10.1002/jcsm.12450).

Einige Abbildungen und Texte können in dieser Dissertation und dem publizierten Artikel identisch sein.

Aachen, den 31.07.2019

Merve Erdem, M. Sc.

Publications

Published articles

Erdem M, Möckel D, Jumpertz S, John C, Fragoulis A, Rudolph I, Wulfmeier J, Springer J, Horn H, Koch M, Lurje G, Lammers T, van der Kroft G, Gremse G, Cramer T. Macrophages protect against loss of adipose tissue during cancer cachexia (J Cachexia Sarcopenia Muscle 2019 Jul 18. doi: 10.1002/jcsm.12450)

Rohwer N, Jumpertz S, **Erdem M**, Egners A, Warzecha KT, Fragoulis A, Kühl AA, Kramann R, Neuss S, Rudolph I, Endermann T, Zasada C, Apostolova I, Gerling M, Kempa S, Hughes, Lewis CE, Brenner W, Malinowski MB, Stockmann M, Schomburg L, Faller W, Sansom O, Tacke F, Morkel M, Cramer T. Non-canonical HIF-1 stabilization contributes to intestinal tumorigenesis (Oncogene 2019 Jul;38(28):5670-5685)

Bagatur Y, Ilter Akulke AZ, Bihorac A**, Erdem M**, Telci D. Tissue transglutaminase expression is necessary for adhesion, metastatic potential and cancer stemness of renal cell carcinoma (Cell Adh Migr. 2018 Mar 4;12(2):138-151)

Egners A, **Erdem M**, Cramer T. The Response of Macrophages and Neutrophils to Hypoxia in the Context of Cancer and Other Inflammatory Diseases (Mediators Inflamm. 2016;2016:2053646)

Erdem M, Erdem S, Sanli O, Sak H, Kilicaslan I, Sahin F, Telci D. Upregulation of TGM2 with ITGB1 and SDC4 is important in the development and metastasis of renal cell carcinoma (UrolOncol. 2014 Jan;32(1):25.e13-20)

Aysan E, Sahin F, Telci D, **Erdem M**, Muslumanoglu M, Yardimci E, Bektasoglu H. Mechanism of body weight reducing effect of oral boric acid intake (Int J Endocrinol.2013;2013:914651)

Erdem M, Tekiner TA, Fejzullahu A, Akan G, Saribeyoglu ET, Anak S, Ozbek, Atalar F. *herg1b* expression as a potential specific marker in pediatric acute myeloid leukemia patients with HERG 897K/K genotype (Pediatr Hematol Oncol. 2015 Apr;32(3):182-92)

Article under review

Berndt N, Egners A, Mastrobuoni G, Vvedenskaya O, Fragoulis A, Dugourd A, Bulik S, Pietzke M, Bielow C, van Gassel R, Olde Damink SW, **Erdem M**, Saez-Rodriguez J, Holzhütter HG, Kempa S, Cramer T. Kinetic modeling of quantitative proteome data predicts metabolic reprogramming of liver cancer (Under review, Cancer Research and available on bioRxiv, Cold Spring Harbor Laboratory, The Preprint Server for Biology, https://www.biorxiv.org/content/early/2018/03/05/275040)

Book Chapter

Telci D, Ilter AZ, **Erdem M**. (2013). Stem Cells in Wound Healing. In K. Turksen (ed.), *Stem Cells: Current Challenges and New Directions*(pp.175-197). New York, NY: Springer

Oral presentation

Erdem M, Drescher C, von Haehling S, Anker S, Springer J, Cramer T, HIF-1α in myeloid cells affects peripheral lipid metabolism in cancer cachexia, short talk at Keystone Symposia: Tumor metabolism: Mechanisms and Targets / Adaptations to Hypoxia in Physiology and Disease, 2017, March 2017, Vancouver, Canada

Poster presentations

Erdem M, Drescher C, von Haehling S, Anker S, Springer J, Cramer T, HIF-1α in myeloid cells affects peripheral lipid metabolism in cancer cachexia, poster presentation at Keystone Symposia: Tumor metabolism: Mechanisms and Targets / Adaptations to Hypoxia in Physiology and Disease, 2017, March 2017, Vancouver, Canada

Erdem M, Fragoulis A, Palus A, von Haehling S, Anker A, Springer J, Cramer T, Introduction of a Mouse Model for Hepatocellular Carcinoma-Associated Cachexia poster presentation at 20th Surgical Research Days: Section of Surgical Research of the German Society of Surgery, Sep 2016, Magdeburg, Germany.

Erdem M, Egners A, Berndt N, Mastrobuoni G, Vvedenskaya O, Bielow G, Kempa S, Holzhütter H, Cramer T, Combination of mass spectrometry-based proteomics and mathematical modelling predicts therapy targets of liver cancer, poster presentation at 6th Conference on Systems Biology of Mammalian Cells, 2016, May 2016, Munich, Germany.

Erdem M, Drescher C, von Haehling S, Anker S, Springer J, Cramer T, Conditional HIF1A gene targeting reveals an unexpected protective role of myeloid cells in cancer cachexia, poster presentation at Changing Views in Cancer, MKFZ Conference 2016, June 2016, Berlin, Germany.

Erdem M, Drescher C, von Haehling S, Anker S, Springer J, Cramer T, Conditional gene targeting reveals an unexpected protective role of myeloid cells in cancer cachexia, poster presentation at 8th International Conference on Cachexia, Sarcopenia and Muscle Wasting, 2015, Dec 2015, Paris, France.

Erdem M, Springer J, von Haehling S, Anker S, Palus S, Cramer T, Cell type-specific role of HIF1α in cancer cachexia in a newly described mouse model of liver cancer, poster presentation at Tumor Microenvironment, Metabolism and Metastasis, DKFZ-ZMBH Alliance Forum 2015, Sep 2015, Heidelberg, Germany.

Erdem M, Springer J, von Haehling S, Anker S, Palus S, Cramer T Cell type-specific role of HIF1A in a newly established mouse model of liver cancer, poster presentation at Keystone Meeting Hypoxia: From Basic Mechanisms to Therapeutics, May 2015, Dublin, Ireland.

Erdem M, Cramer T, Growth promoting effects of insulin on colorectal cancer cells, poster presentation at 1st SignGene Winter School Biology of Differentiation & Cancer, Jan 2014, Haifa, Israel.

Telci D, Aysan E, **Erdem M**, Yalvac E, Muslumanoglu M, Yardimci E, Bektasoglu H, Sahin F, Molecular mechanism of body weight reducing effect for oral boric acid intake, poster presentation at 38th FEBS Congress, July 2013, St. Petersburg, Russia.

Bagatur Y, **Erdem M**, Telci D, Role for tissue transglutaminase (TG2) in renal carcinoma cell adhesion and migration, poster presentation at 37th FEBS Congress, Sep 2012, Sevilla, Spain.

Erdem M, Erdem S, Sanli O, Sahin F, Kilicaslan I, Telci D, Loss of transglutaminase 2 (TG2) activity promotes renal cell carcinoma (RCC), poster presentation at American Urological Association-Annual Meeting 2011, May 2011, Washington, USA.

Erdem M, Erdem S, Sanli O, Sahin F, Kilicaslan I, Telci D, Tissue transglutaminase 2 may be a novel molecular marker in renal clear cell carcinoma, poster presentation at 6th South Eastern European Meeting 2010, Oct 2010, Istanbul, Turkey and abstract in European Urology Supplements, Volume 9, Issue 6, September 2010.

Erdem S, **Erdem M**, Telci D, Sanli O, Kilicaslan I, Esen T, Sahin F, Is there any role of tissue transglutaminase in the pathology of renal cell carcinoma?-The preliminary results of a prospective study, poster presentation at 9. National Congress of Uro-oncology, Nov 2009, Ankara, Turkey.

Erdem M, Tekiner TA, Fejzullahu A, Anak S, Ozbek U, Atalar F, Alterations of *herg1* isoform expressions in pediatric acute myeloid leukemia and solid tumors, poster presentation at European Human Genetics Conference 2009, Vienna, Austria May 2009 and abstract in European Journal of Human Genetics, Volume 17, Supplement 2, May 2009.

Fejzullahu A, Tekiner TA, **Erdem M**, Anak S, Ozbek U, Atalar F, Crosstalk between T-cadherin and Wnt/β-catenin pathways in cancer, poster presentation at European Human Genetics Conference 2009, Vienna, Austria May 2009 and abstract in European Journal of Human Genetics, Volume 17, Supplement 2, May 2009.

Erdem M, Tekiner TA, Fejzullahu A, Anak S, Ozbek U, Atalar F, Upregulation of *herg1b* gene and presence of the functional HERG variant K897T in pediatric acute myeliod leukemia, poster presentation at Second International Congress on Leukemia – Lymphoma – Myeloma, May 2009, Istanbul, Turkey.

Fejzullahu A, Tekiner TA, **Erdem M**, Anak S, Ozbek U, Atalar F, Expression of adiponectin and its receptors in pediatric acute myeloid leukemia: High levels of T-cadherin and loss of adiponectin, poster presentation at Second International Congress on Leukemia – Lymphoma – Myeloma, May 2009, Istanbul, Turkey.